Growth of semiconductor nanostructures by MBE for the study of electron and nuclear spin enhancement and other physical phenomena

By

Qiang Zhang

A dissertation submitted to the Graduate Faculty in Physics in partial fulfillment of the requirements for the degree of Doctor of Philosophy, The City University of New York

2010

This manuscript has been read and accepted for the Graduate Faculty in Physics in satisfaction of the dissertation requirement for the degree of Doctor of Philosophy.

Date	Dr. Maria C. Tamargo Chair of Examining Committee
Date	Dr. Steven Greenbaum Executive Officer

Dr. Aidong Shen

Dr. Carlos A. Meriles

Dr. Igor L. Kuskovsky

Dr. Maria C. Tamargo

Dr. Shiping Guo

Supervision Committee

THE CITY UNIVERSITY OF NEW YORK

Abstract

Growth of semiconductor nanostructures by MBE for the study of electron and nuclear spin enhancement and other physical phenomena

by Qiang Zhang

Adviser: Professor Maria C. Tamargo

Molecular beam epitaxy (MBE) is an extremely versatile thin film technique, which can produce single-crystal layers with atomic dimensional controls and thus permit the preparation of novel structures and devices tailored to meet specific needs. Spin relaxation time τ_s is one of the key features in spin-related phenomena and thus of great importance for spintronics. In this work, we prepare high quality samples, mainly of CdTe epilayers, by MBE, characterize their spin relaxation dynamics, and discuss the results theoretically.

First, with the goal of understanding the mechanisms of electron relaxation dynamics and nuclear spin enhancement, we focus on the growth and characterization of CdTe epilayers. By changing the shutter sequences and inserting ZnSe buffer layer, we have reproducibly grown (111) and (100) CdTe epilayers of high crystalline qualities by MBE, despite the large lattice mismatch between CdTe and GaAs substrate. Then we investigate τ_s for the (111) and (100) CdTe epilayers. It is found that for the (111) CdTe, spin relaxation rate τ_s^{-1} is significantly enhanced and shows no temperature dependence through 130K to 300K, while τ_s^{-1} for the (100) CdTe is strongly affected by the temperature. It is also found that τ_s^{-1} is dependent on material quality for both (111) and

(100) CdTe. We theoretically discuss the effect of strain and defect on spin relaxation time of CdTe. It is the first experimental observation of the effect of strain on τ_s^{-1} in a II-VI semiconductor material.

Second, the growth and characterization of ZnTe/ZnSe related type II quantum structures, or quantum dots (QDs), are also presented in this work. The PL of Zn-Se-Te related type II quantum structures show blue shifts with higher intensities of exciting laser, an indication of type II QDs. Besides being an attractive method to p-type dope wide bandgap materials, the resulting material may be a promising structure for spin enhancement properties.

Third, we present the study of the enhancement of nuclear spin polarization through pumping laser. We find strong enhancement both in bulk CdTe as well as in CdTe epilayers, independent of the helicity of the laser, which is on the contrary to the prior reports by others. Compared with GaAs crystal, we ascribe this independence to the surface spin-dependent recombination. GaAs/AlAs and GaAs/GaAlAs multiple coupled double quantum wells (QWs), and CdTe/CdMgTe QW have also been grown and explored. The measurements show good quality of the material and are consistent with the designed structures.

Last, we summary the work and propose the future directions.

Samples are in-situ monitored by reflection high energy electron diffraction (RHEED). Post growth characterization techniques, such as time resolved Kerr rotation (TRKR), X-ray diffraction (XRD), photoluminescence (PL), and optical pumping nuclear magnetic resonance (OPNMR), are introduced and applied to the samples.

Acknowledgements

When I started my Ph. D. research, I felt I'd known a lot about the "Philosophy", while nothing could really be handled. After five and a half years of practical laboratory life, I feel I am just a snotty-nosed kid in the field of physics, while I am able to make something real under control, as growing thin films by MBE, one of thousands of branches of the "Philosophy". There are many generous helps on my route of evolution, and here I'd like to express my sincere gratitude and appreciation.

First of all, I would like thank my mentor Prof. Maria C. Tamargo. There is no way to express the luck of being advised by you, not only in research itself, but also in the attitude of doing research. Thank you for providing me with high level lab facilities and the freedom to explore new topics. Thank you for giving me the freedom to fail as well as to succeed. Probably I've learned much more from what didn't work than what did. Your encouragement, inspiration and optimism will benefit me the whole life.

Many thanks to my co-mentor Prof. Carlos. A. Meriles. It is you who lead me to the fascinating "spin" world. Thank you for the illuminating scientific discussions guiding me in the ambiguous "spin" fog. The research could not be done without your generous help and I wish I could work with you in the future.

Many thanks to Prof. Aidong Shen. To me, you are more like a respectable knowledgeable brother than a teacher. Thank you for your selfless help and it is really a good feeling to talk with you, of science and life.

William, I owe you a debt of gratitude for your generous help. Thank you for your help at the beginning when "I felt I'd known a lot about the 'Philosophy', while I could handle few of the experimental”. It is a good experience to work with you in the last three years. Best wishes to your coming PH. D. defense and your family.

I’d like to thank Prof. Igor L. Kuskovsky for the PL measurements and theoretical discussions at Queens College, as well as the free lunch and ride to subway station. I also thank Prof. Ying-chih Chen and Prof. Yuhang Ren for the help at Hunter College, and Prof. Francisco Fernandez for the ECV training and Dr. Shiping Guo for kindly driving a long way to City College to serve in the committees of my 2nd exam and defense. I also want to say “thank you” to my old friend Mr. Binlin Wu for the help all times and “Good luck to your research.”

I am indebted to Ms. Chenghui Liu, Dr. Hong Lu, Dr. Bingsheng Li, Dr. Bo Li, Dr. Wei Dong, Dr. Xuejun Liu, Mr. Yu Zhao, Ms. Li Zhang, Mr. Chun-Min Feng, and other group members: Yunpu Li, Daniela Pagliero, Kuaile Zhao, Le Peng, Vasilios Deligiannakis, Humara Sultana, Adrian Dario Alfaro-Martinez, Allen, Jorge, etc.

Finally I’d like to thank my parents. Your endless love is the origin of all my life, and your honesty and diligence is the biggest treasure you give me. I also want to thank my two sisters and their families for their support all times.

Table of Contents

List of figures and tables

Chapter 1

Introduction

1.1 Molecular Beam Epitaxy (MBE)

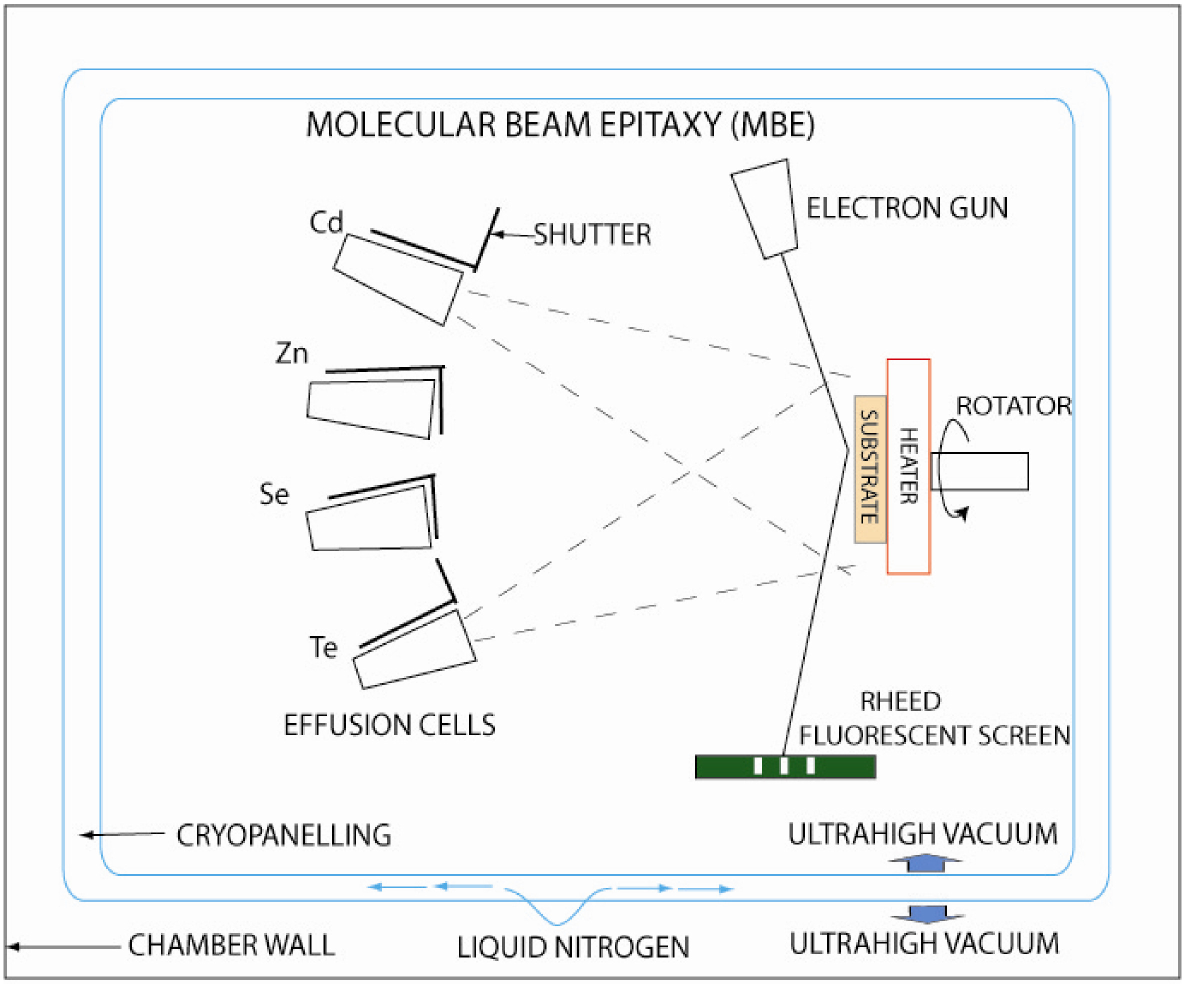

Fig. 1.1 Schematic diagram of MBE process for the growth of CdTe.

The MBE process achieves epitaxial growth in an ultra-high vacuum (UHV) environment through the chemical reaction of one or more thermal molecular beams with a crystalline surface of the substrate [1-3]. The schematic diagram of the MBE process is shown in Fig. 1.1, illustrating the growth of CdTe epilayers. The UHV environment, provided by the liquid-nitrogen-cooled cryopanels, is essential to minimize unintentional impurity incorporation in the deposited layers from the residual background. Molecular beams generated by thermal Knudsen effusion cells interact on a heated crystalline substrate to produce a single crystal layer. Each cell contains one of the constituent elements or compounds required in the epitaxial growth. The temperature of each cell is chosen to evaporate the desired molecular beam flux so that the vapor pressures of the materials are sufficiently high for generation of thermal energy molecular beams by free evaporation and films of the desired composition may be obtained. The growth temperature of the substrate, provided by the heater, is also adjusted properly to perform the necessary processes, such as deoxidation, growth and annealing. Our III-VI chamber includes cells of Ga, In, As, Al, Si and Be, and II-VI includes cells of Zn1, Mg, Zn2, Cd, N, ZnCl2, Se and Te. The cells are arranged so that the central portion of the beam flux distribution from each cell intersects the substrate, ensuring optimum film uniformity both of composition and thickness. Rotation of the substrate, provided by the rotator, is also important to facilitate this criterion. Reflection high energy electron diffraction (RHEED) equipment is usually mounted with the geometry depicted in Fig. 1.1, monitoring the growth in real time, and thus, of great importance.

By inserting mechanical stops or shutters between each cell and the substrate, the growth process is of high controllability. As the name molecular beam implies, the beam flux of each source can be consider unidirectional with negligible interaction within the evaporating species. By operating the shutters between each cell and the substrate and choosing appropriate substrate temperature, epitaxial films of the desired chemical components, and crystal orientation, can be obtained. The extremely high precision in beam flux control allows the growth of very thin layers, even monolayers (ML) thick.

1.2 Introduction of spintronics

Spin, akin to electric charge and rest mass, is a fundamental characteristic property of elementary particles, such as electrons and nuclei. Spin electronics, or spintronics [4], aims to employ this spin degree of freedom to extend the realm of semiconductor electronics. The information could be stored or transferred through the spins of charge carriers, rather than the absence or presence of these particles. Spintronics, the systematic control of electron angular momentum, is emerging as an attractive opportunity for the development of novel computational and information-storage devices, and is providing new discoveries for fundamental science and phenomenology. It may not be a big imagination of far future. Actually, in 1990, Datta and Das introduced a device concept, called spin transistor, that could possibly completely revolutionize semiconductor electronics [5].

Of principal interest in this emerging field is the control and manipulation of electron spin angular momentum. Spin relaxation and spin dephasing, the essential part of spin relaxation dynamics, are processes that lead to spin equilibration and are thus of great importance for spintronics.

Until recently, extensive investigations have been carried out in III-V semiconductors, especially GaAs-based structures, while far less in II-VI semiconductors [6]. CdTe is a potential material for spintronics because it has the same crystal structure and different material parameters (e.g., lattice constant, effective masses, spin-orbit coupling) than III-V semiconductors. There are some reports of the spin dynamics by Time resolved Kerr rotation (TRKR) measurements at room temperature (RT) on bulk CdTe [6, 7] and CdTe-related low-dimensional structures [8, 9]. But there are still some conflicting reports. For example, the relaxation time (2.5ps) reported in Ref. [7] is more than 20 times less than that (52ps) in Ref. [6], which claims that the difference probably originated from the excitation intensity and/or the CdTe samples, as well as the incorrect Kerr rotation dynamics measured in Ref. [7], that is, different relaxation times they measured [10].

Control of nuclear spin angular momentum is also emerging, though more recently, owing to the promise of sensitivity-enhanced nuclear magnetic, as it has been known for decades that optical fields could affect nuclear spin momentum indirectly through electrons. Indeed, the general scheme of “optically pumped nuclear magnetic resonance (OPNMR)” is the generation of a non-equilibrium reservoir of excited electron spins, which subsequently cross-relax with nuclei [11]. The mechanism by which the nuclear polarization changes, is not yet fully understood. As a result, the study of interaction between electrons and nuclei becomes relatively important. Particularly intriguing is the II-VI group because several of these semiconductors have proven amenable to optical pumping in bulk, although no OPNMR studies in nanostructures with these compositions have been reported to date.

1.3 The scope of this dissertation

To get a better understanding of the spin relaxation dynamics, we focus on a II-VI material: CdTe. First, we develop an orientation-controllable technique to grow CdTe epilayers of high material quality by MBE. Second, we perform TRKR measurements on these CdTe samples and discuss the dependence of spin relaxation times on temperature and material qualities, based on a theoretical model involving the effect of strain on spin relaxation time of CdTe. Third, we perform OPNMR measurements on the CdTe semiconductors and find strong enhancement both in bulk material and films, and present possible explanations [12]. Last but not least other nanostructures, such as type II structure, are explored and characterized.

The outline of this work is the following:

In chapter 2 we introduce the general growth procedure of MBE and experimental techniques to monitor the growth and characterize the samples.

In chapter 3 we focus on the growth and characterization of (100) and (111) CdTe epilayers and CdTe/CdMgTe quantum wells (QWs). Possible explanations of the orientation-controllable growth are presented.

In chapter 4 we observe the dependence of electron spin relaxation times on temperature and material quality. Theoretically we discuss the dependence, based on the interlayer model.

In chapter 5 we present the growth and characterization of ZnTe/ZnSe type-II QDs, which show potential application in both electronic device fabrication and study of longer electron spin relaxation times.

In chapter 6 we investigate the nuclear spin relaxation dynamics of CdTe by OPNMR and find strong enhancement both in bulk CdTe as well as in the MBE grown CdTe epilayers, independent of the pumping laser helicity. We also explore some other III-V nanostructures, such as GaAs/AlAs and GaAs/GaAlAs QWS.

In chapter 7 we summarize the work and propose future directions.

Chapter 2

Experimental techniques

In this Chapter, we first give a brief description of the MBE system in our laboratory, which is the foundation of this entire work. Then we present the general growth procedure, and discuss the optimum growth conditions for hetero-epitaxial nanostructures. In situ and ex situ characterization techniques used in the work are introduced, including: Reflection high energy electron diffraction (RHEED), X-ray diffraction (XRD), Photoluminescence (PL), Scanning electron microscope (SEM), Hall effect measurement, Reflection spectroscopy, Time resolved Kerr rotation (TRKR) and Optically pumped nuclear magnetic resonance (OPNMR). Some other less frequently used techniques, such as Residual gas analyzer (RGA), Electrochemical capacitance voltage (ECV), Atomic force microscopy (AFM), Profilometer, etc., are introduced upon the specific measurements.

2.1 General growth procedure of MBE

The MBE system that we employ is a Riber 2300P shown in Fig. 2.1, which contains six chambers: loading chamber, transfer channel, substrate treatment chamber, metallization chamber, and two growth chambers. Fig. 2.2 shows schematic of the top-view of the system. There are several gate valves to separate all the chambers to insure that unintentional cross contamination between them does not occur. In order to avoid contamination and achieve ultra-high vacuum, all the chambers are pumped by an ion-pump and a Ti sublimation pump except the loading chamber, which is pumped by a turbo molecular pump backed by a mechanical pump. The II-VI chamber is pumped by an additional cryo-pump, which is especially effective when the nitrogen plasma source is being employed. The substrates or samples can be transferred within the system through the transfer channel and handled by transfer rods.

Fig. 2.1 The photo of Riber 2300P dual chamber MBE system.

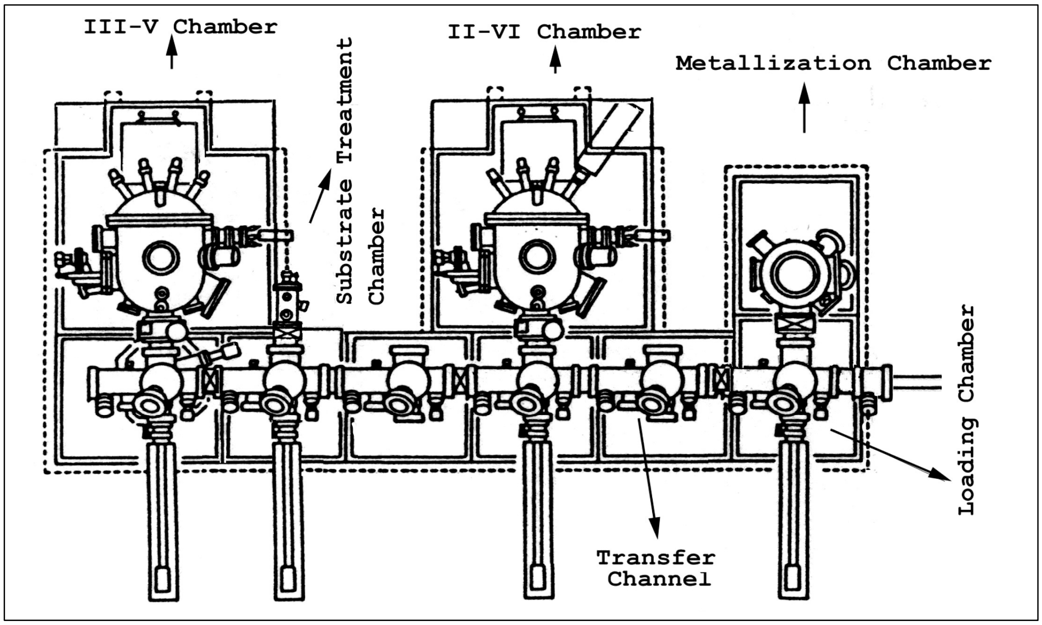

Fig. 2.2 Schematic top-view of the MBE system (after Ref. [1]).

As illustrated in Fig. 2.3, generally we grow samples by the following steps: (1) substrate preparation, (2) III-V semiconductor growth, (3) II-VI nanostructures growth if needed.

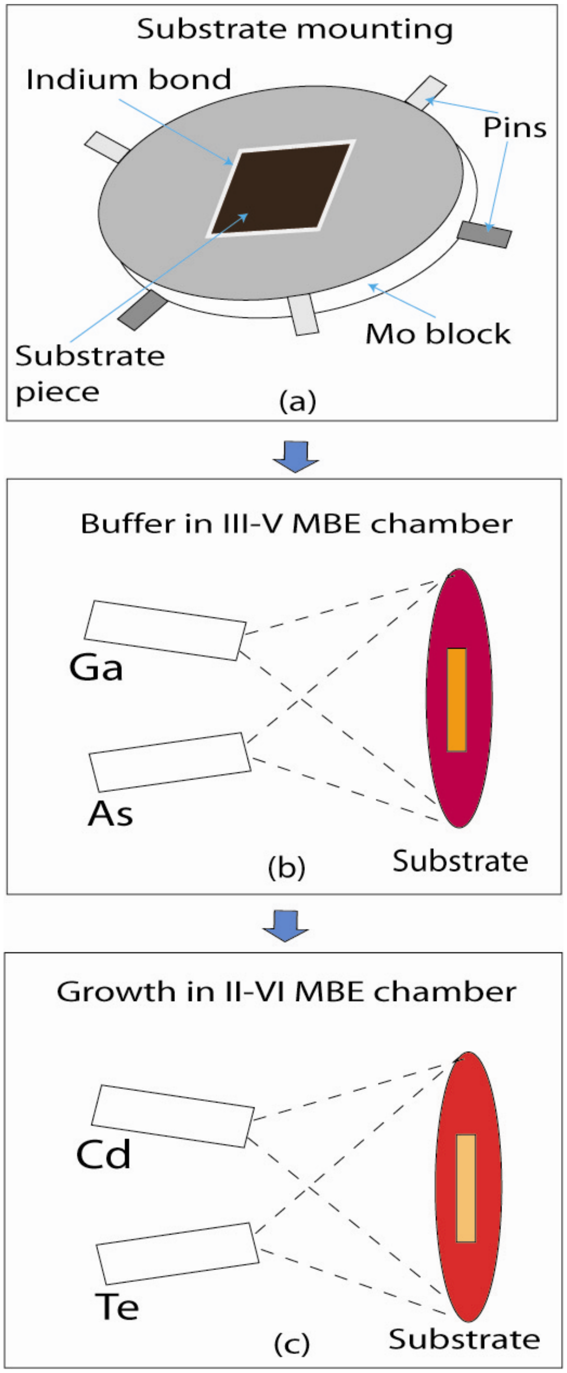

Fig. 2.3 Illustration of the growth procedure, subsequently from (a) to (c).

2.1.1 Substrate preparation

In our laboratory, epi-ready GaAs and InP substrates are most often used, which do not need to be chemically cleaned. Usually, the epi-ready GaAs or InP substrates are cleaved to smaller pieces of proper dimension as shown by the dark brown square in Fig. 2.3(a), and then each of the pieces is indium-bonded onto the center of a molybdenum (Mo) block, which acts as the substrate holder. Before mounted, the Mo block is cleaned by a chemical etching procedure, including an ultrasonic cleaner and chemicals, such as HCl, Br_2:Methanol, DI water, Aqua Regia ($HCl:HNO_3$) and Methanol.

All the operations are carried out in an air-flow class-100 clean hood located in our clean room. Once the substrates are prepared, they are placed in glass petri dishes and transferred to the loading chamber in the clean room. After the substrates are transferred into the loading chamber, which is vented by ultra pure nitrogen gas, the chamber is at atmospheric pressure. It is necessary to pump it down ($\sim 10^{-8}$ torr), which is carried out, subsequently, by a mechanical pump ($\sim 10^{-1}$ torr), liquid-nitrogen cooled sorption pumps ($\sim 10^{-3}$ torr) and a turbomolecular pump ($< 10^{-8}$ torr). Then the substrates are transferred to the UHV III-V chamber via the transfer channel.

2.1.2 Growth in the III-V chamber

Prior to growth, the source cell temperatures in the III-V chamber have been increased and stabilized so that they provide desired fluxes, which are monitored by a flux gauge placed in the substrate position. The oxide desorption of the substrate is performed in by heating the substrate with an As flux impinging on the substrate surface. Once the oxide is removed, evident by the streaky RHEED patterns (detailed in the following section Chapter 2.2), a desired epitaxial layer may be deposited on the substrate in the III-V chamber, as shown in Fig. 2.3(b). Often the purpose of the III-V layer is to smooth the surface of the substrate, and to facilitate high quality II-VI growth, so that the epitaxial layers grown act as buffer layers, typically a GaAs layer for a GaAs substrate, or a lattice-matched InGaAs layer for InP substrates. It is critical to adjust the temperatures of the substrate and sources to control the growth rate of ~1 μm/hour.

2.1.3 Growth of II-VI nanostructures

Once the buffer layer has been deposited on the substrates, the substrates are transferred quickly via the UHV transfer channel to the II-VI chamber to perform the growth of the desired II-VI materials, as shown in Fig. 2.3(c). It is essential to grow a high quality III-V/II-VI buffer to reduce the defect density and increase the lifetime of devices based on II-VI semiconductors [13]. In the case of ZnSe buffering on GaAs epi-layer, it is demonstrated that it is important to avoid the initial interaction between Se and the III-V material [14]. It is reported the precise control of the III-V surface stoichiometry is important to reduce this interaction [15]. In order to reduce the defect density, some techniques are usually employed, such as an As-terminated III-V buffer surface, a "Zn irradiation" before the II-VI buffer growth and an initial buffer grown at relatively low temperature, all of which favor initial two-dimensional growth. In the case of an InP substrate, a ZnCdSe buffer is usually employed to improve the III-V/II-VI interface quality [16].

Once the proper buffer is deposited, the designed the II-VI nanostructure can be grown by operating the shutters, manually or programmed by the computer. A thin cap layer may be applied at the end to avoid surface oxidation for some compounds containing Mg. Some II-VI materials of interest in our lab are ZnSe, CdSe, ZnCdSe, ZnCdMgSe, CdTe, CdMgTe, and their p-type or n-type doped semiconductors. Once the growth is done, the samples are transferred back to the loading chamber and taken out for post-growth characterization.

Following the growth procedure, CdTe and other samples are prepared by this Riber 2300P MBE system. In the case of CdTe epilayers grown on (100) GaAs substrates, the high quality ZnSe (100) epitaxy on GaAs provides an essential function allowing us to control the II-VI/III-V interface prior to the CdTe deposition. Subsequently by adjusting the interface between ZnSe and CdTe, it is possible to selectively obtain the growth of either (100) or (111) CdTe epitaxial layers on the (100) ZnSe/GaAs substrate. The controllable high quality films hereby provide a stage to access material inherent properties, such as spin relaxation dynamics. Specific sample growth procedures will be detailed in Chapter 3 and 5.

2.2 In situ probe: Reflection high energy electron diffraction (RHEED)

The UHV condition in the MBE system allows some techniques to be performed in situ to obtain information about the growth, such as the growth background, growth mode, surface chemical composition and topography and the energy levels of the epilayer. Besides Reflection high energy electron diffraction (RHEED), a key technique to assist real-time control of the growth, there are other important techniques that can be applied in the MBE system, such as Auger electron spectroscopy (AES) for the determination of surface chemical composition, X-ray photoelectron spectroscopy (XPS) and Ultraviolet photoelectron spectroscopy (UPS) for the study of the electronic structure and energy levels of the epilayer, Secondary ion mass spectroscopy (SIMS) for the determination of the chemical composition of the outermost epilayers, and residual gas analyzer (RGA) for the determination of the growth background. In our laboratory, the RGA is mounted in the transfer channel to do the background inspection and works efficiently as a leak check for both chambers, due to the high sensitivity of helium. Only RHEED is employed in this work to characterize in situ the growth of the epilayers.

It is important to monitor the sample surface during the growth. A. Y. Cho was the first to use MBE to prepare GaAs surfaces under well-defined conditions and used RHEED to investigate reconstructions occurring on surfaces and how they related to growth conditions and subsequent processing [17]. RHEED is a highly suitable technique to carry out such studies during the substrate deoxidation and epilayer growth. The glancing angle geometry of RHEED, as shown in the Fig. 2.4(a), is the most appropriate configuration for MBE, since the electron beam can be placed at glancing incidence, whereas the molecular beams impinge almost normally on the substrate. The wavelength of the electrons is similar to the lattice constant of the material, resulting in a diffraction pattern that can be viewed on phosphor screen due to the fluorescence caused by the electrons. For example, electrons with energies 10-100 keV, generated by an electron gun, reach the sample surface with a very small (glancing) angle of 1-2° to the crystal surface. Calculating the de Broglie wavelength of the electrons using a mathematical approximation for these conditions, a range of 0.12-0.037 Å is obtained, which insures that the penetration of the beam into the surface is low and restricted to the outermost few atomic layers. In our laboratory, the electrons have energy ~10 keV, and the penetration depth is very small, ~0.12 Å, because the only important component that influences the penetration is the normal component to the surface.

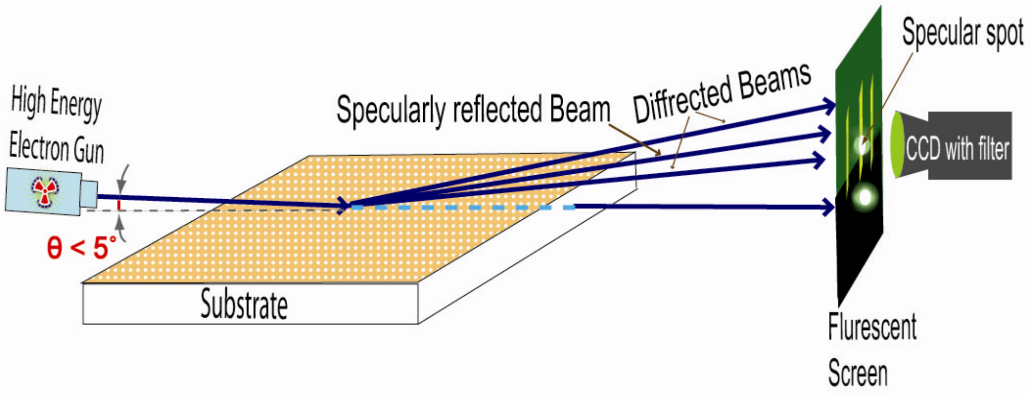

(a) Schematic of RHEED with CCD camera

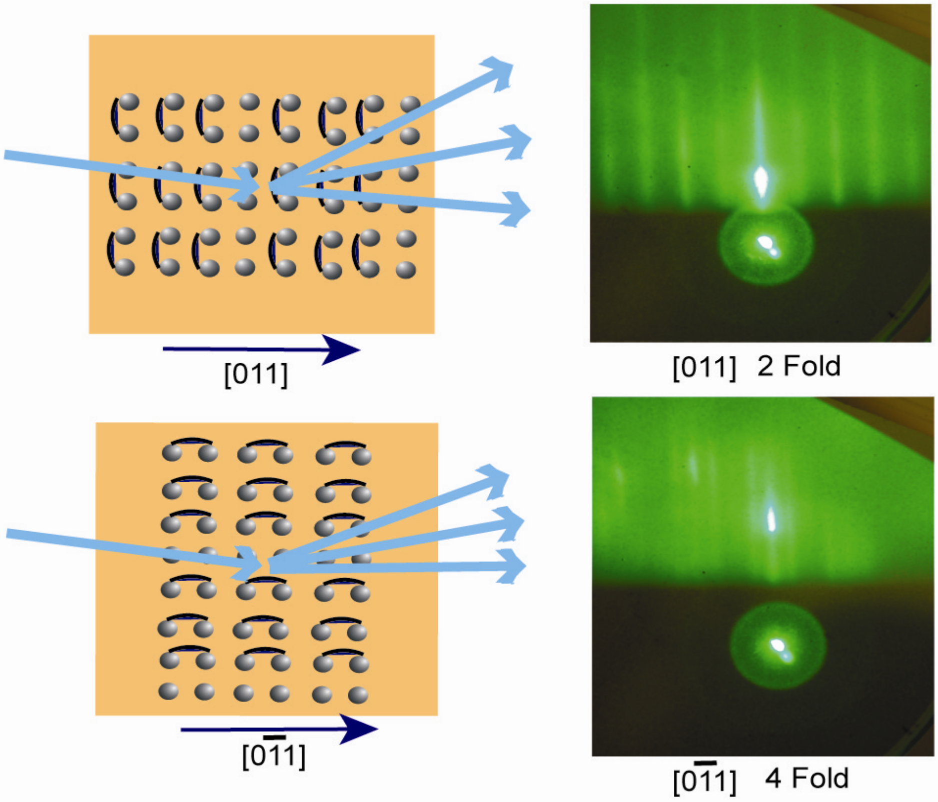

(b) A surface reconstruction (2X4)-β and its RHEED patterns

Fig 2.4 (a) Schematic representation of RHEED with a CCD camera for oscillation measurements. (b) A surface reconstruction (2×4)-β (missing row model) in real space and corresponding patterns: 2 fold in the [011] azimuth and 4 fold in the [0$\bar{1}$1] azimuth.

The RHEED pattern depends on the atomic arrangement, flatness of the surface and the crystalline orientation of the growth surface. The typical RHEED pattern for a disordered (amorphous) surface (for example before the deoxidization) is a diffuse pattern or rings due to the thin amorphous oxide layer on the surface, and for a clean surface after deoxidization it is streaky lines or ordered spots. RHEED is also sensitive to the mode of growth that is occurring on the substrate (three dimensional or two dimensional) and to some extent, on the chemical nature of the surface. In the case of three dimensional ("rough") growth, due to in the growth a strained thick layer or the growth of three-dimensional quantum dots (QDs), ordered spots are expected as the RHEED pattern, while for two dimensional growth (layer-by-layer growth), it is "rods" or "streaks". The diffraction pattern is unique for a given azimuthal orientation of substrate and provides, in addition to surface quality and growth mode, information about the surface reconstruction.

Much interest has been shown in the (100) can (111) surfaces of compounds grown by MBE. These polar surfaces may have an excess of one or more atoms depending on growth conditions or post growth treatment. They have associated with a large number of reconstructions in which the surface atoms reorder themselves to produce a periodicity different from that of the underlying crystal. Such reconstructions are usually denoted by a convention described by Wood, and we follow this convention in this work [18]. A surface structure denoted by (100)-(m X n) means that a crystal is orientated with the [100] direction normal to the surface and has a surface structure, due to reconstruction, whose unit mesh is m X n times larger than the bulk structure. Such surface meshes may be centered, in which case there is a mesh site at the center of the (m X n) mesh and the notation would be (100)-c(m X n). If the mesh is rotated so that its principal axes are not aligned with those of the underlying bulk then the rotation angle is also included, e.g., GaAs (111)-$\sqrt{19} \times \sqrt{19} R23.4^o$ [17].

The surface reconstructions for As-rich (100) GaAs surfaces are dependent on how much excess of As is on the surface. As shown in Fig. 2.4(b) they are typically (2 X 4), or c(2 X 8) or c(4 X 4). In contrast, for a Ga-rich (100) GaAs, the surface reconstructions are (4 X 2) or c(8 X 2). In the case of InGaAs on (100) InP substrate, surfaces reconstructions are also, respectively, (2 X 4) or (4 X 2) in As-rich or Ga-rich surfaces [3]. For a Se-rich (100) ZnSe the typical pattern is (2 X 1) and for Zn-rich (100) ZnSe the pattern is c(2 X 2) [15]. -For a Te-rich (100) CdTe, the typical pattern is (2 X 1), same to the Se-rich (100) ZnSe, but the separation between the rods reduce visually during the transition from ZnSe to CdTe when we grow a CdTe/ZnSe heterostructure. While for a Te-rich (111) CdTe, the typical pattern is $2\sqrt{3} \times 2\sqrt{3} R30^o$, showing a 3-fold symmetry typical of the (111) surface [19].

It is possible to explore the growth dynamics of MBE by monitoring temporal variations in the intensity of various features in the RHEED pattern. Since the beginning of 1980’s it has become apparent that when MBE growth is initiated, the intensity of the various features shows an oscillatory behavior which is directly related to the growth rate. It is found that the oscillation is most pronounced in the specularly reflected beam (or specular spot). The oscillations in the intensity of RHEED patterns are considered to be related to the changes in surface roughness during growth, and the proposed model for monolayer growth is shown in Fig. 2.5. From the top to the bottom in this schematic, the intensity of the specular spot oscillates with the fractional surface coverage and is hereby monitored by a CCD camera.

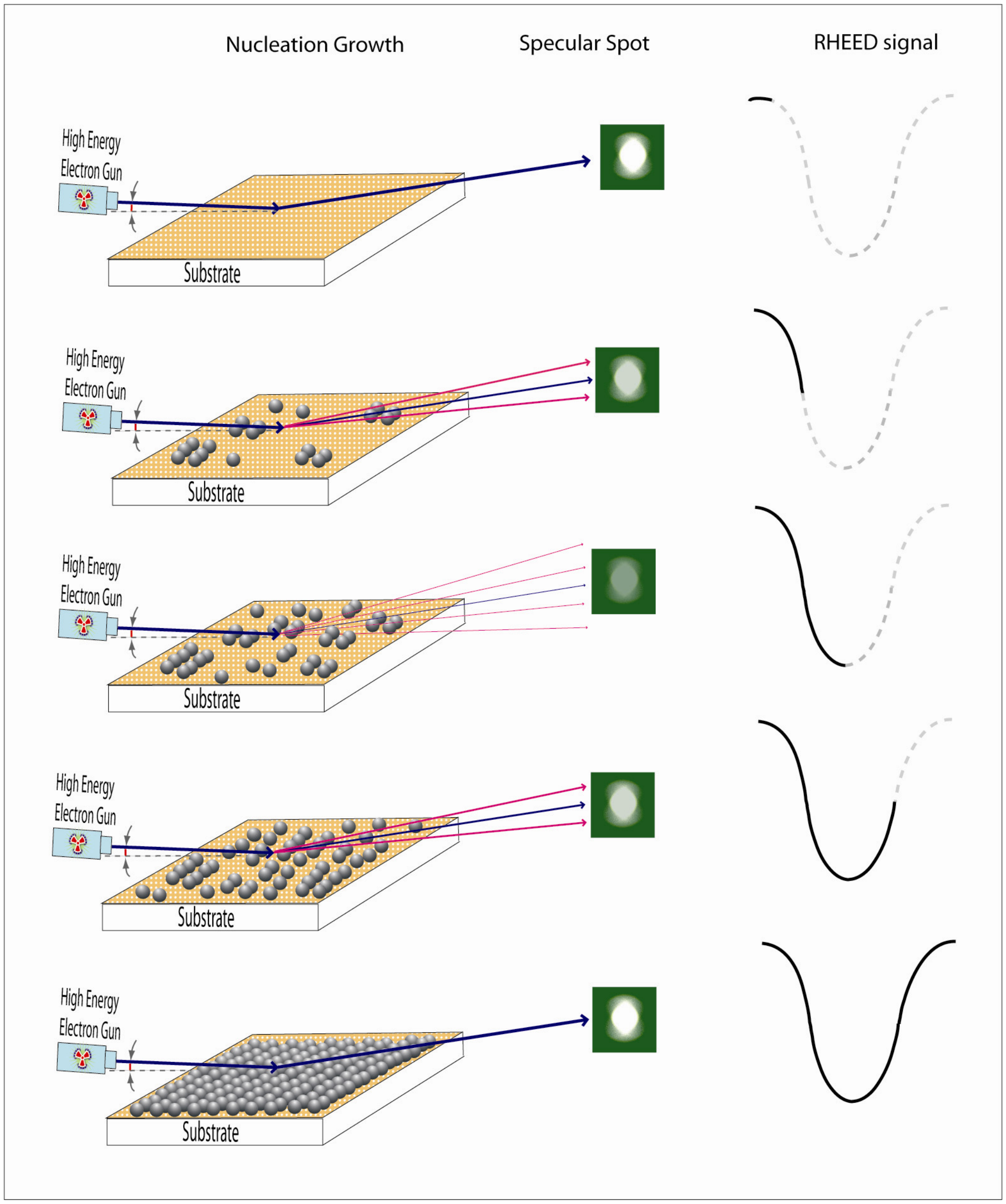

Fig. 2.5 Schematic of nucleation growth and completion of a ML. The intensity of the specular spot oscillates with the fractional surface coverage and is hereby monitored by a CCD camera. Note that nucleation of a second layer is possible before the completion of the first.

The equilibrium surface existing before growth is smooth, corresponding to high reflectivity of the specular (zeroth-order) beam. On commencement of growth, nucleation islands will form at random positions of the surface, leading to a decrease in reflectivity. These islands will grow and ultimately produce another smooth surface, and it would be expected that the minimum in reflectivity would correspond to 50% coverage by the growing layer. The observed damping in the reflectivity oscillations will occur if nucleation takes place on a growing layer before it is complete and the oscillations will cease as the growth centers become distributed over several incomplete atomic layers. Note that nucleation of a second layer is possible before the completion of the first.

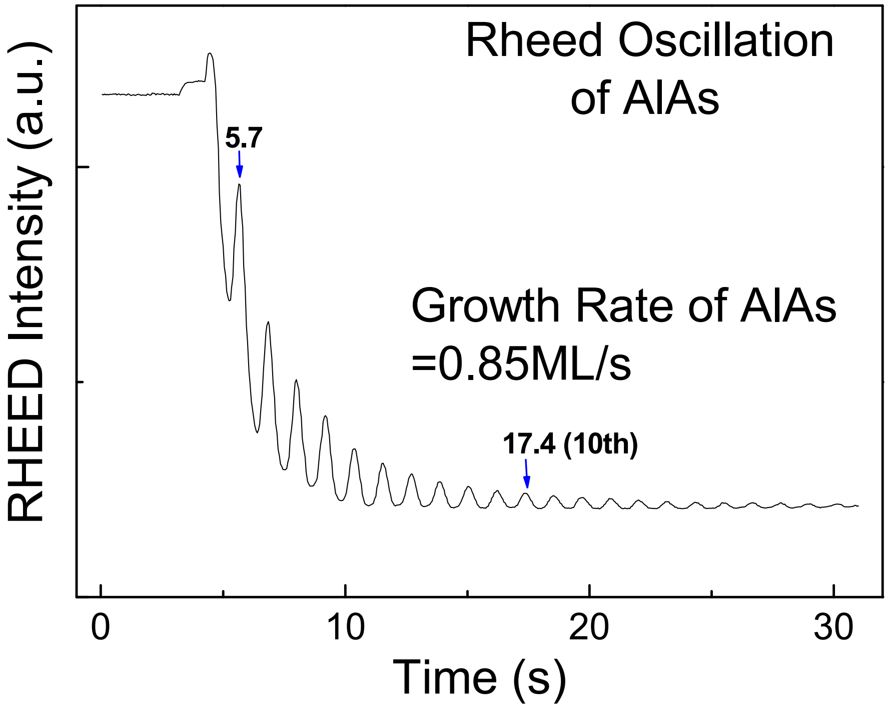

Fig. 2.6 The RHEED intensity oscillations of the specular spot of AlAs epilayer.

RHEED oscillation measurement has now become routine to calibrate beam fluxes and control alloy composition and thickness of nanostructure epilayers. Data relating to surface diffusion, crystal growth mechanisms, and dopant incorporation have also been obtained from studies of RHEED intensity oscillations. The RHEED intensity oscillation at specular spot of AlAs is shown in Fig. 2.6, corresponding to a calculated growth rate 0.85 ML/s (0.86μm/h).

2.3 Post-growth characterization techniques

It is necessary to characterize the samples after the growth, so that we could obtain a wide range of information of crystal structure, surface topography, chemical composition, carrier concentration and epilayer quality and furthermore, adjust the growth conditions and evaluate our progress.

Once the sample has been taken out of the MBE system, proper ex situ characterization should be performed as soon as possible. The surface of the epilayer could be first characterized by an optical microscope and then by surface profilometer and AFM, if needed. The thickness of the epilayer could be determined by SEM and Reflection spectroscopy, compared with the calculated one based on the RHEED oscillation. The electronic structure could be determined by PL and Reflection spectroscopy. Current-Voltage (I-V) measurement is used to characterize the electrical properties. Doping level and hall mobility of the doped layers could be determined by Hall effect measurement and ECV. The crystalline quality and lattice-mismatch were measured by single crystal and double crystal XRD. Electron spin relaxation time is determined by TRKR, and OPNMR is employed to detect the enhanced NMR signal. All these characterization tools are employed in our laboratory and some of them will be detailed in the following subsections. [1-3, 20-27].

2.3.1 X-ray diffraction (XRD)

X-ray diffraction is an important technique used to characterize semiconductor materials. It can give information about the lattice constant, the crystal structure and orientation, the crystalline quality and strain in the layer.

The principle of the XRD is the Bragg's law, based on the condition for the constructive interference:

$$n\lambda = 2d\sin\theta$$

where d is the spacing of lattice planes and θ is the corresponding Bragg angle denoting the angle between the lattice planes. The scattering geometry of X-ray diffraction is shown in Fig. 2.7.

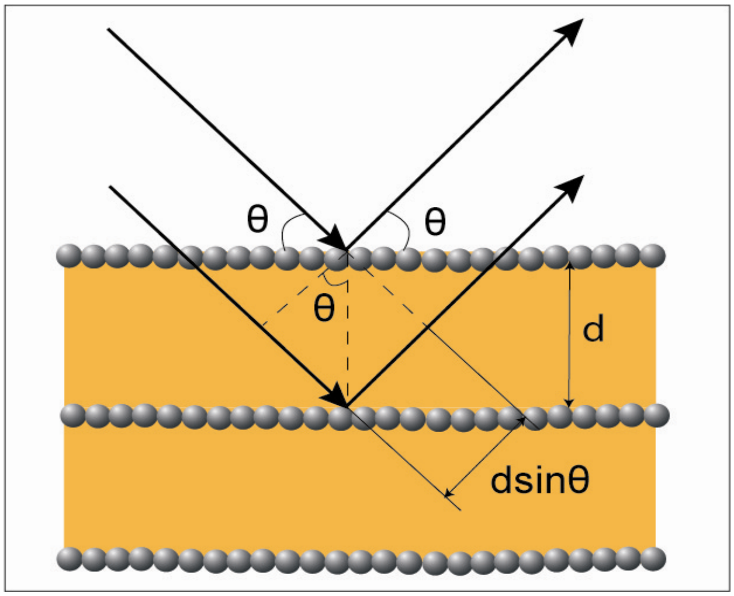

Fig. 2.7 The scattering geometry of X-ray diffraction.

The schematic diagram of our X-ray diffraction system is shown in Fig. 2.8. It consists of an X-ray source, a single crystal X-ray diffraction system (SCXRD), and a double crystal X-ray diffraction system (DCXRD). The X-ray is generated by a Cu X-ray source producing two lines, $K_{\alpha1}$ and $K_{\alpha2}$. In SCXRD, only one crystal (the sample) is used, so the incident X-ray is not monochromatic. Therefore, in the diffraction, each layer has two peaks corresponding to Cu $K_{\alpha1}$ and Cu $K_{\alpha2}$. Usually the intensity of the Cu $K_{\alpha1}$ peak is double that of the Cu $K_{\alpha2}$ peak. The SCXRD is good to measure large lattice-mismatch and to find the structure of the materials.

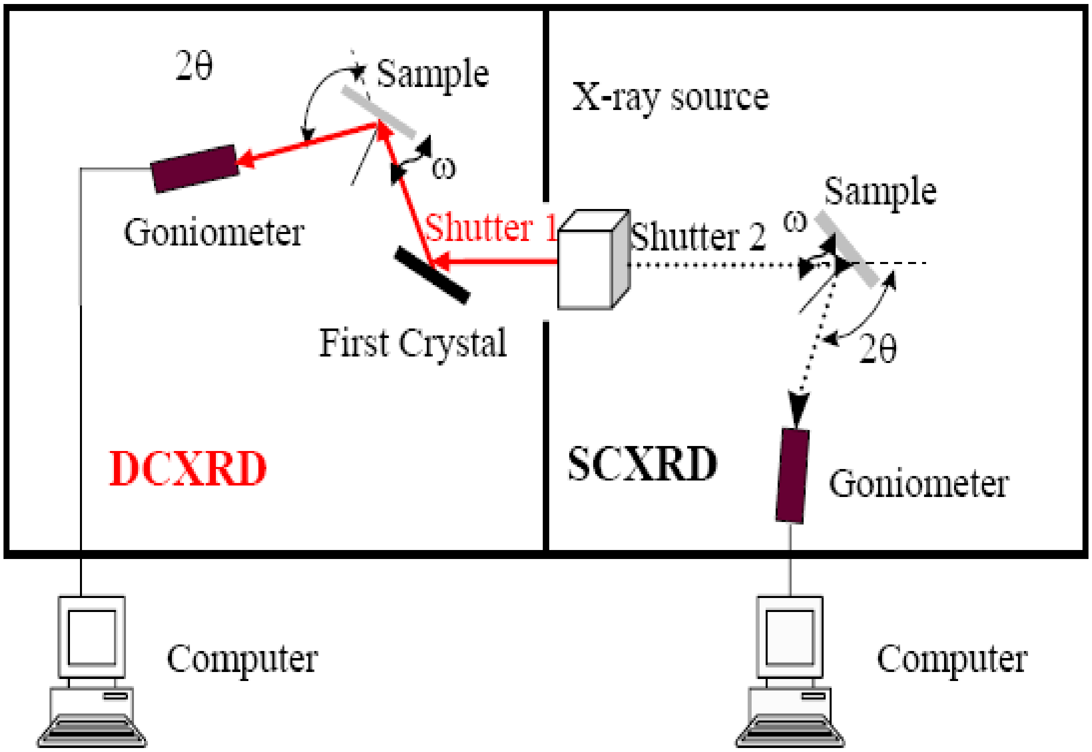

Fig. 2.8 Schematic of X-ray diffraction system (after Ref. [1]).

In DCXRD, a first crystal ((100) Ge) is used to filter out the Cu $K_{\alpha2}$ line and narrow the X-ray band of wavelengths before the X-ray beam reaches the sample (the second crystal). Because of its increased resolution, DCXRD is good to measure small lattice-mismatch and accurately determine lattice constant and material composition of the sample. The full width at half maximum (FWHM) of the diffraction peaks gives us information about the material quality. The lattice-mismatch can be evaluated by

$$\Delta a / a_S = (\frac{a_E - a_S}{a_S}) \times 100\%,$$

where a_S and a_E are the lattice constants of substrate and epilayer, respectively, which we can obtain by measuring the Bragg angles.

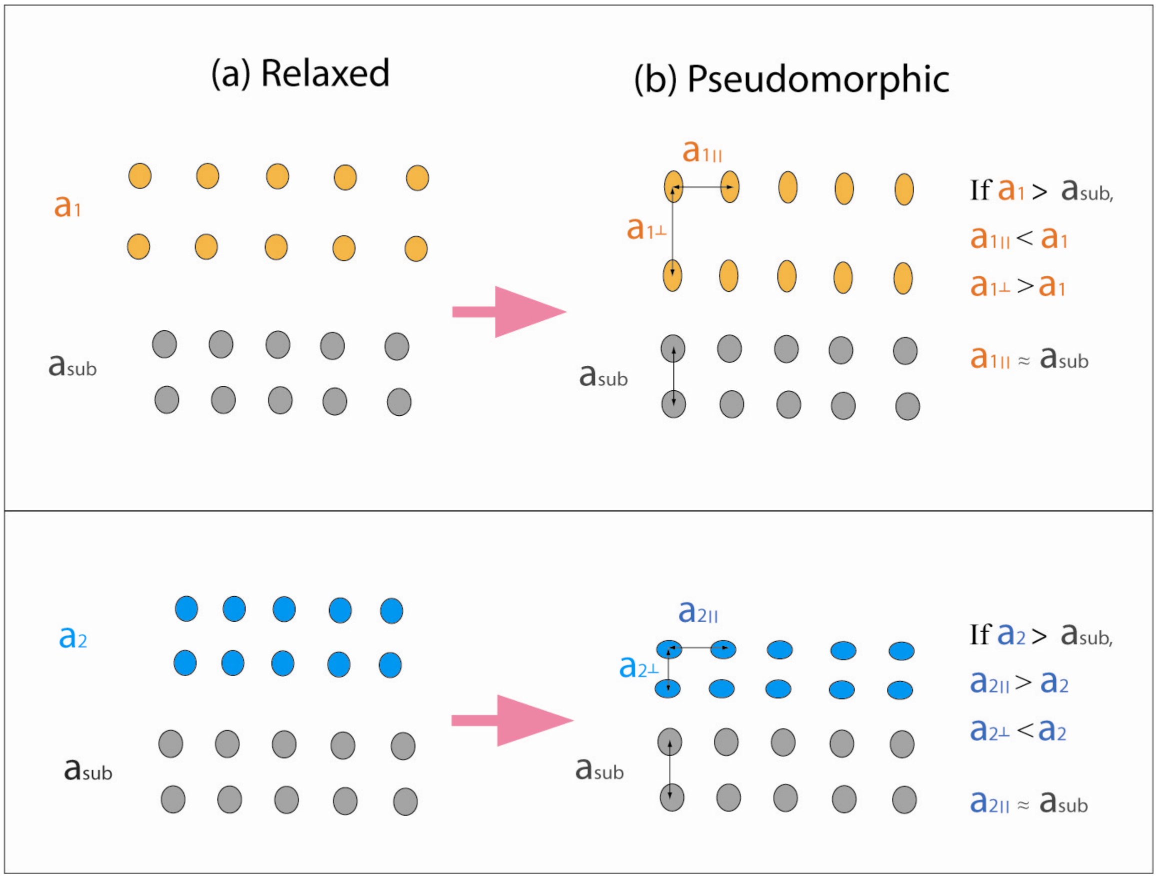

Fig. 2.9 Schematic of the (a) relaxed and (b) pseudomorphic interfaces

XRD is also a powerful tool to inspect the strain in the epilayer, usually due to the lattice mismatch and different thermal expansion. For an epilayer grown on a substrate with a different lattice constant, the epilayer could be strained. When the thickness of the epilayer is less than a certain value (critical thickness), the epilaer will be pseudomorphic (strained) and the crystal structure could be distorted, as shown in Fig. 2.9. In the case that the epilayer lattice constant $a_1 > a_{sub}$, the epilayer lattice could be compressed in the interface plane and expanded in the growth direction (tetragonal distortion) , leading to the in-plane lattice constant $a_{1||} < a_1$ and the normal lattice constant $a_{1\perp} > a_1$. On the other hand, if the epilayer lattice constant $a_2 < a_{sub}$, the epilayer structure could be expended in the interface plane and compressed in the growth direction, leading to the in-plane lattice constant $a_{2||} > a_2$ and the normal lattice constant $a_{2\perp} > a_2$. In both cases, the in-plane lattice constant of the epilayer is assumed to be the same to the substrate lattice constant within the critical thickness, i.e., $a_{||} = a_{sub}$.

If the epilayers are pseudomorphic (not relaxed), the strain-free lattice constant cannot be obtained from only the (400) X-ray rocking curves. And the epilayer is deformed from cubic to tetragonal. So the composition of the epilayers cannot be calculated for the (400) X-ray rocking curves. To obtain the strain-free lattice constant, we could use the X-ray results from other reflections, such as, (511) reflections and the elastic theory. According to the solution of Hooke's law with biaxial stresses, the perpendicular and parallel strains in the epilayer are related by the Poisson effect so that

$$a_f = {(1-\nu)a_\perp}\big/{1-\nu} + {2\nu a_{||}}\big/{1+\nu}$$

where ν is the Poisson ratio of the film (ν~0.33 for GaInAs and ~0.41 for CdTe) and a_f is the free standing lattice constant of the epilayer, Both $a_\perp$ and $a_{||}$ could be measured by calculating the difference in Bragg angles between (511)a and (511)b.

X-ray rocking curves in directions other than the above ones are also popular, such as (200), which is more effective on determination of longer special periodicity by so-called satellite peaks. The periodicity could be deduced and simplified as:

$$p = \frac{\lambda}{\cos\theta \bullet \Delta\theta}$$

where λ is the X-ray wavelength (Cu $K_{\alpha1}$=1.54056 Å). This will be applied on GaAs/AlAs QW in Chapter 6.2. The satellite peaks from the periodicity of the QWs could be clearly seen in DCXRD of the 200 direction other than that in 400 direction shown in Fig 6.6.

2.3.2 Photoluminescence (PL)

Photoluminescence (PL) is a very powerful, nondestructive technique employed to investigate the electronic structure around and below the energy gap of semiconductor materials.

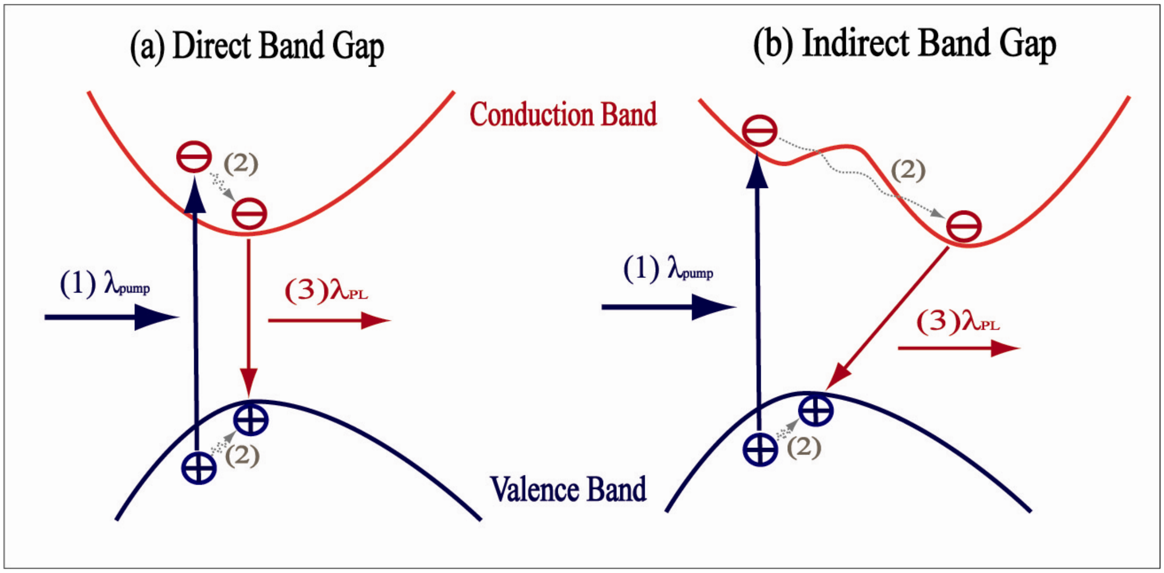

Fig. 2.10 General steps involved in a PL experiment.

PL can be defined as an optical excitation-emission process, in which photons of $hv_0 > E_g$ are absorbed by the semiconductor, creating electron-hole (e-h) pairs that subsequently will recombine emitting photons. The steps involved in the general PL process are schematically represented in Fig. 2.10. (1) The e-h pair excitation: Initially, the e-h pairs are photoexcited to a non-equilibrium state by absorption of light (generally, generated by a laser). (2) The e-h pair thermalization and diffusion: The e-h pairs diffuse and relax into a quasiequilibrium distribution to the lowest energy state (non-radiative process). (3) The e-h recombination: The e-h pairs recombine, emitting photons, or by other non-radiative processes. Different from the direct band structure, the indirect band structure occurs when the minimum of the conduction band does not coincide in momentum space with the maximum of the valence band. A similar situation, called "spatially indirect bandgap" structure, arises when the electrons are confined in one material and the holes are confined in a different material. This gives rise to a difference between the absorption energy and the emission energy, as well as a longer time to diffuse and relax, hereby leading a less probability of the last step (3) than the direction transition. This "indirect" alignment could be a potential advantageous structure in the study of spin relaxation time, which will be introduced in details in Chapter 5.

The PL technique is commonly used in a MBE lab, not only for the possibility to characterize the most fundamental optical properties of the grown materials, such as band gap, donor and/or acceptor states, deep defect levels, the quality and the band structure of epilayers, but also for the flexibility of its setup geometry. In addition, for the PL excitation it is not necessary to fabricate a contact or a junction (as electroluminescence), making PL an interesting method to characterize materials and devices in early stages of development and growth.

Besides these advantages, other advantages that made this technique a useful tool in a semiconductor lab are: (i) It is a non-destructive technique where only small quantities of material are needed. (ii) It provides information mainly on minority carrier properties and, thus, it is complementary to electrical characterization techniques. The lifetime, the diffusion length, the quantum efficiency could be inferred through the study of the recombination paths. When the photo-generated e-h pair density is larger than the free carrier concentration (high excitation conditions), majority carrier properties are also accessible. (iii) It is an easy technique because it does not require particular sample handling and preparation. The experimental set-up complexity is proportional to the needs: for fast characterization a very simple and inexpensive apparatus is adequate. (iv) It is sensitive to the chemical species of impurities, which can be detected even at very low densities. (v) It is an optical spectroscopic technique, i.e., it gives energetically resolved information.

2.3.3 Scanning electron microscope (SEM)

The thickness measurements provide information about the growth rates and conditions of the thin layer film. We perform the thickness measurement through the images of Scanning electron microscope (SEM), a type of electron microscope that images the sample surface by scanning it with a high-energy beam of electrons in a raster scan pattern. Higher resolution could be achieved because SEM uses high-energy electrons (shorter wavelength) instead of light to form an image.

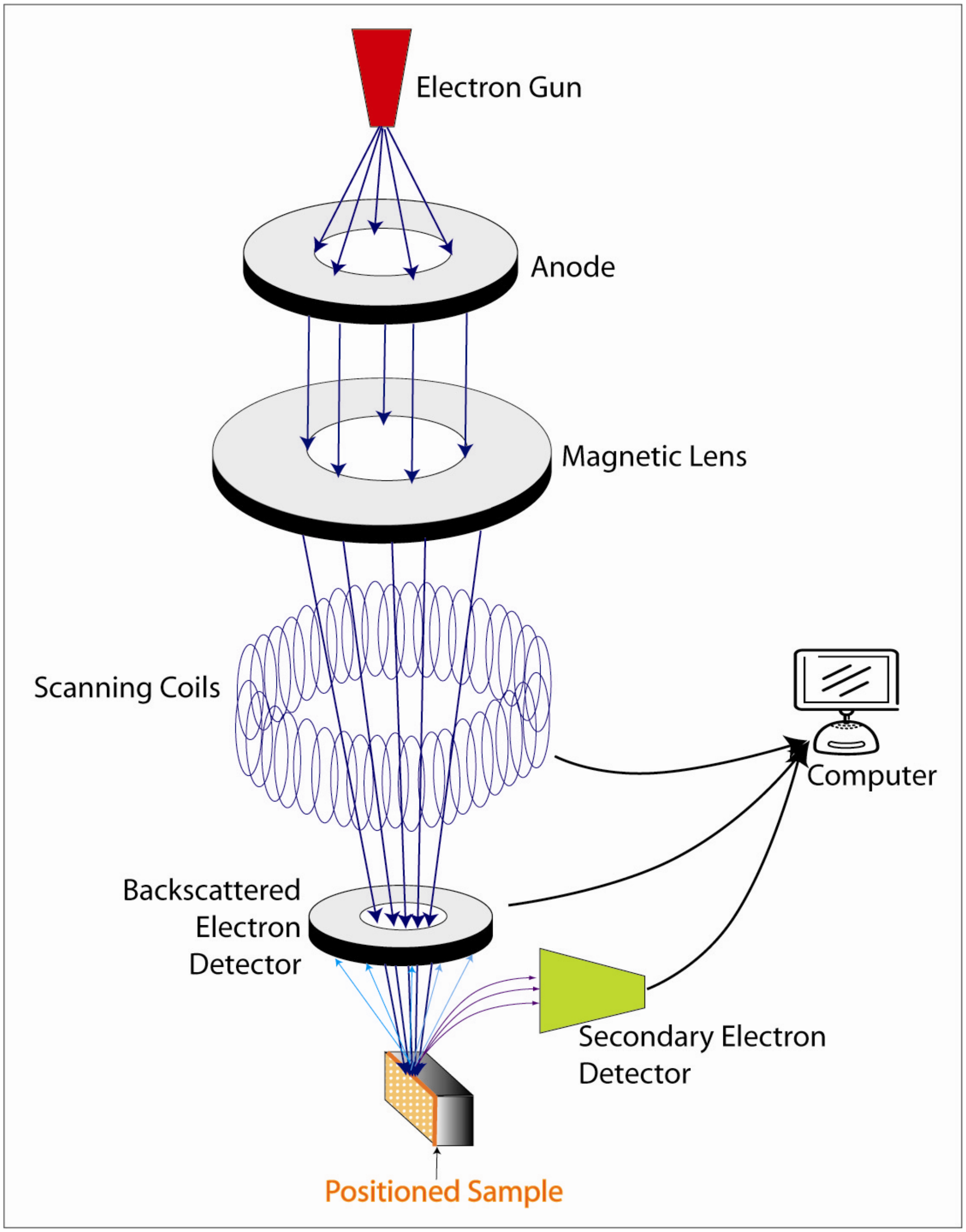

Fig. 2.11 The illustration of SEM.

The illustration of the SEM is shown in Fig. 2.11. A beam of electrons is produced by an electron gun at the top of the microscope by heating of a metallic filament. The electron beam follows a vertical path through the column of the microscope. It makes its way through electromagnetic lenses which focus and direct the beam down towards the sample. Once it hits the sample, other electrons (backscattered or secondary) are ejected from the sample. Detectors collect the secondary or backscattered electrons, and convert them to a signal that is sent to a viewing screen similar to the one in an ordinary television, producing an image. Different layers can be distinguished by different lightness due to different reflection index. So that we can read out the thickness of the layer, therefore we can obtain the growth rate of that layer by dividing the growth time.

SEM imaging is the most direct way to measure the film thickness. We can recall that it could also be measured *in situ* by RHEED at high growth temperature, as introduced in Chapter 2.2, by simply calculating the product of growth time and the growth rate. Reflection spectroscopy provides yet another easier way to measure thin film post growth at room temperature (RT), once the function of refractive index is available. This characterization technique will be detailed in Chapter 2.3.5.

2.3.4 Current-voltage (I-V) and Hall effect measurement

Hall effect measurement are employed mainly to measure the carrier type, density, and mobility. The contacts for the Hall effect measurement must be tested before the measurement to determine their Current-voltage (I-V) characteristics.

I-V measurement is fundamentally applied in our laboratory to characterize the behavior of contacts (ohmic: either ideal non rectifying barrier contact or tunneling barrier contact, diode contact and others). An ohmic contact is a low-resistance junction providing conduction in both directions between the metal and the semiconductor. To test the I-V characteristics of the contacts, indium is annealed on the semiconductor surface. Sometime a gold deposition is applied, by evaporating on the clean surface of the sample with the vapor deposition machine. After the evaporation, a small drop of indium served to solder the gold wire to the surface.

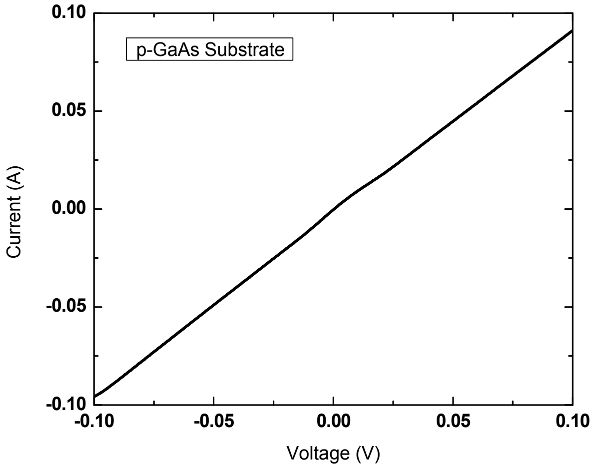

Fig. 2.12 The I-V curve of a p-type GaAs substrate.

A Keithley source unit model 236 for the I-V measurements is employed to determine the I-V characteristics of the samples. Ideally, the current through the ohmic contacts is a linear function of the applied voltage (following the Ohm's law) and the applied voltage should be very small. Fig. 2.12 shows the measured I-V curve of a p-type GaAs substrate.

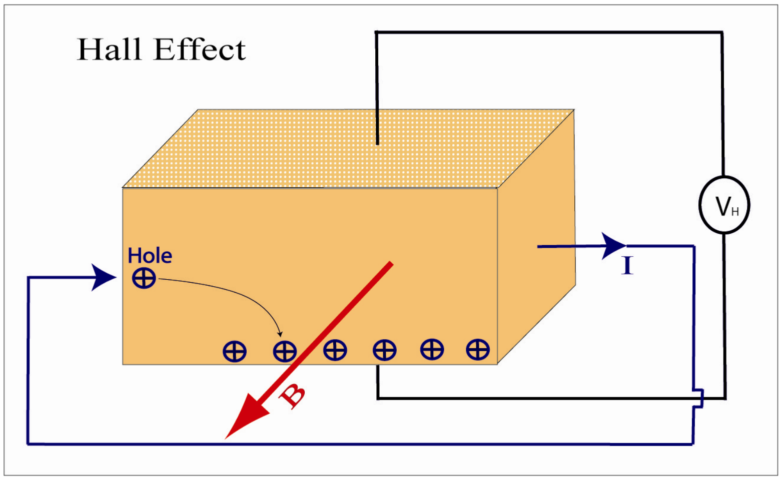

Fig. 2.13 Schematic of Hall effect for a p-type semiconductor sample.

Fig. 2.13 shows a schematic diagram of the Hall effect principle for a p-type semiconductor sample (the n-type case is analogous). As is illustrated in the figure, an electric field is applied along the x-axis while a magnetic field is applied along the z-axis. The electric field is defined the electric force per unit charge: $\vec{E} = \vec{F}/q$, Where $\vec{E}$ is the electric field, $\vec{F}$ is the force and q is the charge. For a p-type sample, the Lorentz force, produced by the magnetic field is represented by:

$$\vec{F} = q\vec{V} \times \vec{B}$$

where $\vec{B}$ is the magnetic field, $\vec{V}$ is the velocity and q is the charge. This Lorentz force causes an average downward force on the holes, and downward directed current causes a piling up of the holes at the bottom side of the sample, which in turn give rise to another upward electric field. Since there is no net current along the y direction in the steady state, the electric field along the y axis (Hall field) exactly balances the Lorentz force. Once the steady state is ready, several important parameters, such as the Hall coefficient, carriers' type, concentration, mobility, etc., can be obtained by calculation.

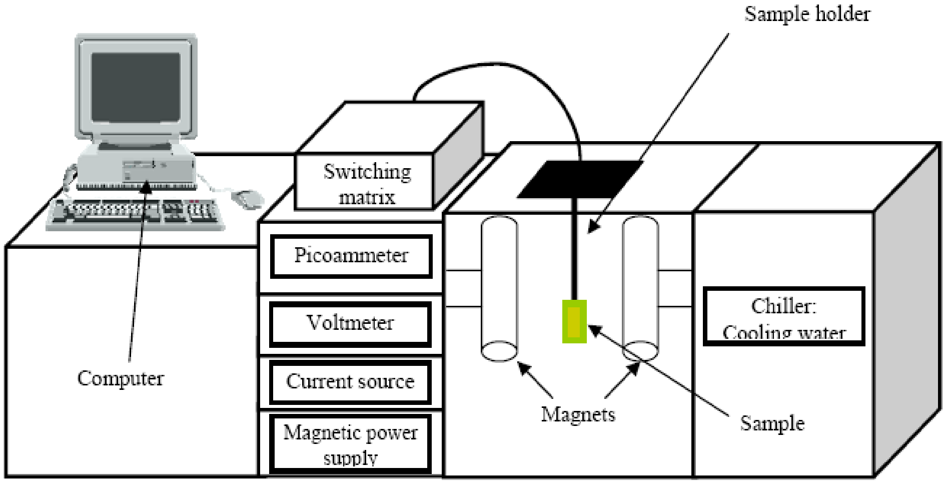

Fig. 2.14 The Hall effect measurement apparatus (after Ref. [1]).

Fig. 2.14 shows our Hall effect measurement apparatus. The magnetic field $\vec{B}$ used for Hall effect measurements in our laboratory is fixed at 2.5 kG (0.25T). Hall effect measurements are used to measure the doping level in Chapter 5. To measure the doping level within a complex structure, eletrochemical capacitance-voltage (ECV) measurement, which gives the net carrier concentration of different layers and is introduced in the following section, could be performed, as in Chapter 6.2. This technique is especially useful when the epilayer is grown on a conducting substrate, which makes it impossible to perform the Hall effect measurement.

2.3.5 Reflection spectroscopy

The reflectance spectrum of a sample could provide some information of epilayer, such as absorption and thickness. The surface and interface condition, band gaps of substrate and epilayer will affect the signal strength, as well as the size of the sample. For a refractive index known epilayer, the thickness measurement is preferred by reflectance measurement due to its easy procedure and nondestructive feature.

The conditions of applicability of the method can be summarized as follows: (1) The film and substrate are optically isotropic and homogeneous. (2) There is a difference between the refractive index of the film and that of the substrate. (3) The film boundaries are flat and smooth. (4) The film has low or medium absorption so that the interference fringes are visible. (5) The optical thickness of the film is high enough to yield enough number of interference extremes.

To deduce the refractive index of a thin film is a key issue of the reflection spectroscopy, even for some commercial thin-film-measurement equipment, for example, Thin-Film-Measurement Spectroscopic Reflectometer Nanocalc-2000-UV/VIS/NIR, available in our group. Different approaches have been used for deducing the optical parameters of a thin absorbing film on a transparent substrate or on an absorbing one and from reflectance measurements. The most common approach consists of fitting the theoretical reflectance spectra to the experimental ones. In this proposal, the reflection spectrum of an absorbing film on an absorbing substrate is used in case of normal light incidence. The normal incidence is chosen for its experimental simplifications. The upper and lower envelopes of the interference fringes are used to get the reflectance factors at the interfaces and approximate values of the film refractive index. This index is used to deduce the interference orders and the film thickness. Finally accurate values of film indices could be calculated. Only the reflectance spectrum at normal incidence is sufficient for calculations.

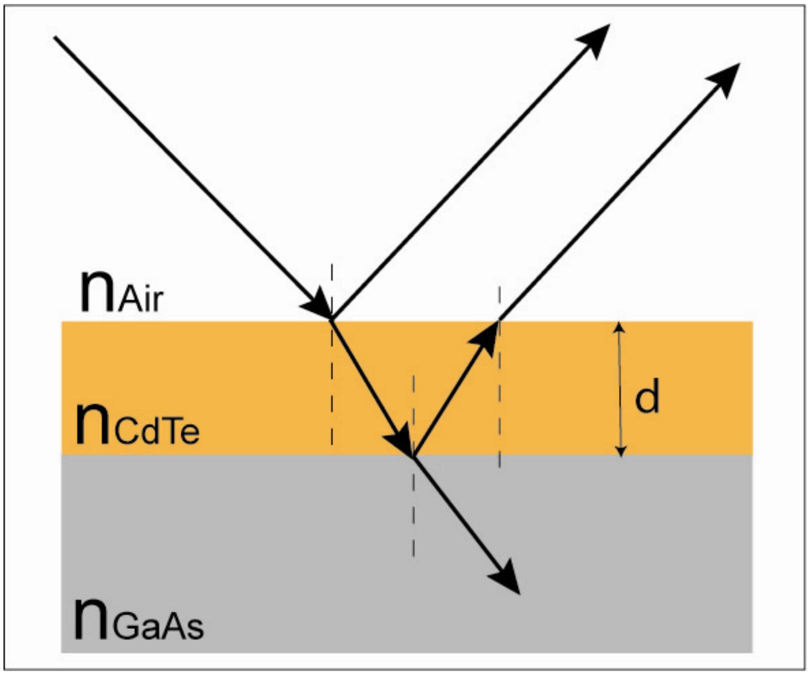

Fig. 2.15 Schematic of reflection and transmission for a CdTe/GaAs sample.

Consider a parallel beam of light, with wavelength λ, incident on the film–substrate system, for example, CdTe/GaAs heterostructure as shown in Fig. 2.15. Since the optical path difference inside the film is less than the coherence length of the incident beam then there are multiple reflections inside the film that produces coherent interference fringes. The reflection from the back surface of the substrate is neglected. This is due to that the substrate is absorbing enough to cancel the backward reflections or it can be roughed or blackened.

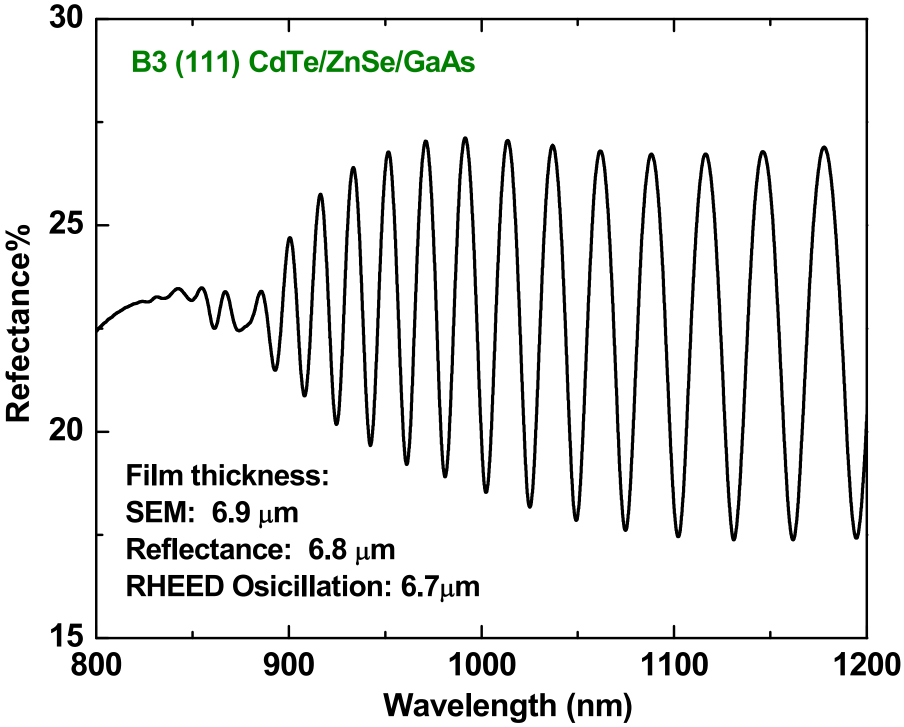

Fig. 2.16 Reflection spectra of a CdTe film.

For bulk CdTe epilayer, Marple originally measured the refractive index at 300K from a prism of melt-grown material with polished surfaces in 1962 from which the following modified Sellmeier equation was derived [28]:

$$n = \sqrt{A + \frac{B\lambda^2}{\lambda^2 \quad C^2}} \quad ,$$

where A=5.68, B=1.53 and C^2=0.366.

Barnes also developed a temperature-dependant Sellmeier dispersion equation, based on the data across a range of reduced temperatures (80-300K) by Harvey and Wolfe [29]. Calculate approximate values for the film thickness d for the wavelength of maxima and minima of reflection using the relation:

$$d = \frac{\lambda_1 \lambda_2}{4(n_2\lambda_1 - n_1\lambda_2)}.$$

Fig. 2.16 shows the reflection spectrum of a CdTe sample. The measured band gap is about 1.51 eV, which is consistent with PL measurement at RT. The thicknesses are 6.7, 6,8 and 6.9 µm measured by RHEED oscillation, reflection spectroscopy and SEM, respectively.

2.3.6 Time resolved Kerr rotation (TRKR)

There are two magneto-optical (MO) effects we could use to study the spin dynamics beyond the gigahertz frequency domain: MO Faraday effect in the transmission geometry and the MO Kerr effect in the reflection geometry. The MO Kerr effect, which we utilize to study the spin dynamics in this proposal, arises from the difference between the optical coefficients of a material for right-handed and left-handed circularly polarized light. This difference can be induced by an applied magnetic field, a spontaneous, or an optically induced magnetization.

The schematic electronic band structure of CdTe near the Γ point and absorption transitions with circularly polarized light are shown in Fig. 2.17(a). The top valence band is split into a degenerate $P_{3/2}$ band, including a heavy-hole (HH) subband and a light-hole

(LH) subband, and a split-off $P_{1/2}$ band that lies below $P_{3/2}$ at the energy Δso=0.8 eV for CdTe at RT [30]. The allowed transitions are determined by the selection rule: $\Delta m_j = m_f - m_i = 1$ [31], shown in Fig. 2.17(b).

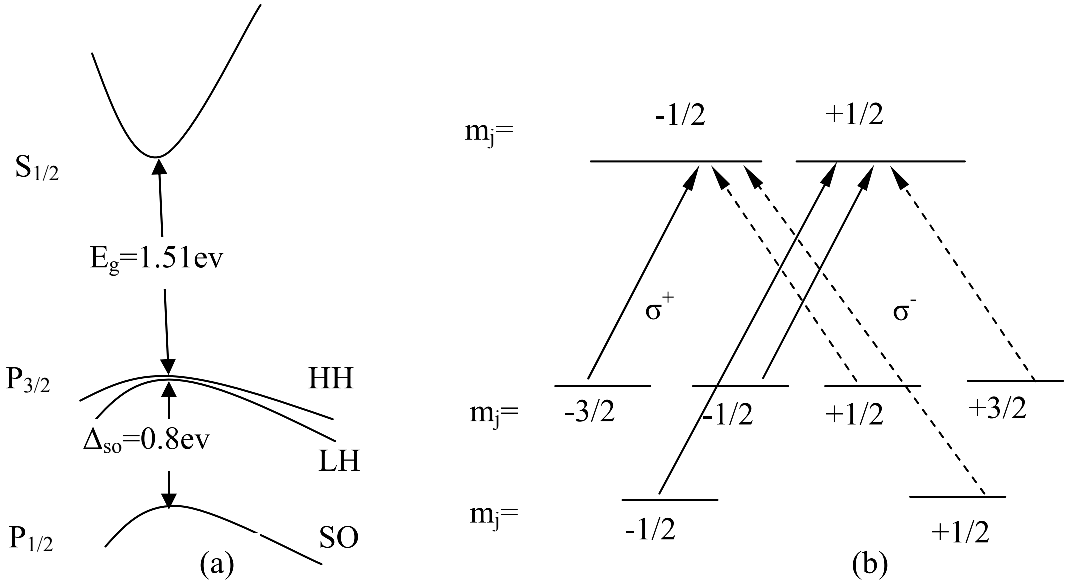

Fig. 2.17 On the left, schematic electronic band structure of CdTe near the direct band gap shows E_g=1.51ev and spin-orbit splitting Δ_{so}=0.8ev. The allowed electric dipolar transitions for right-handed (solid arrows) and left-handed (dashed arrows) circularly polarized light are shown on the right.

An ensemble of electron spins subject to a magnetic field is commonly characterized by three relaxation times: The longitudinal spin relaxation time T_1, which is related to the relaxation of the spin component parallel to the field, and the transverse relaxation times T_2 and T_2^*. The T_2 denotes the relaxation of the spin components transverse to the field, i.e., spin decoherence, of a single electron, while the T_2^* denotes the decoherence of the spin ensemble taking into account the inhomogeneous broadening the electron g factor. The coherence time T_2 is usually a few orders of magnitude longer than T_2^*. Although T_2

is the quantity of most interest for quantum computing, the longitudinal spin relaxation time T_1 is typically easier to measure [10].

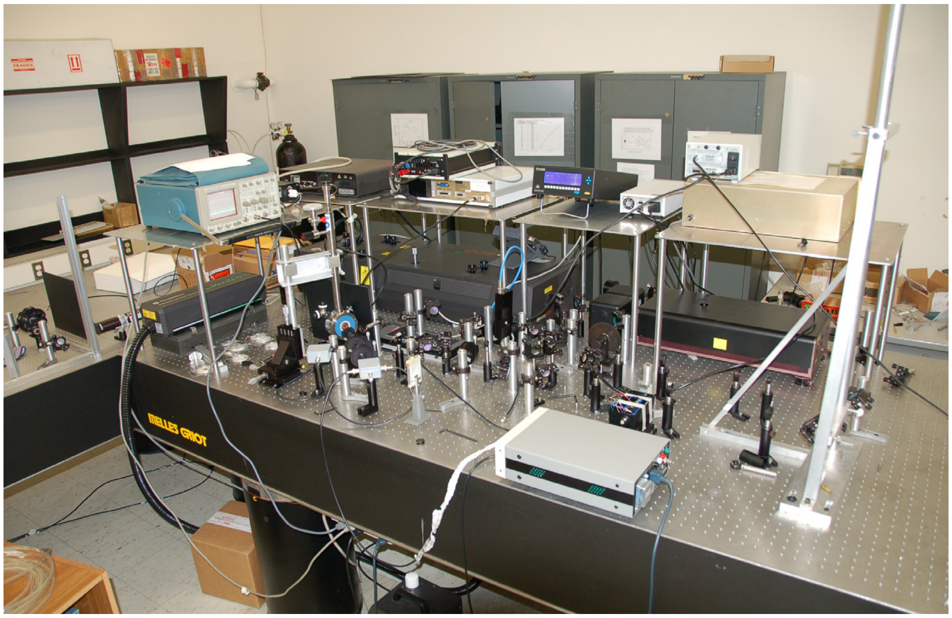

Fig. 2.18 Photo of the setup of TRKR.

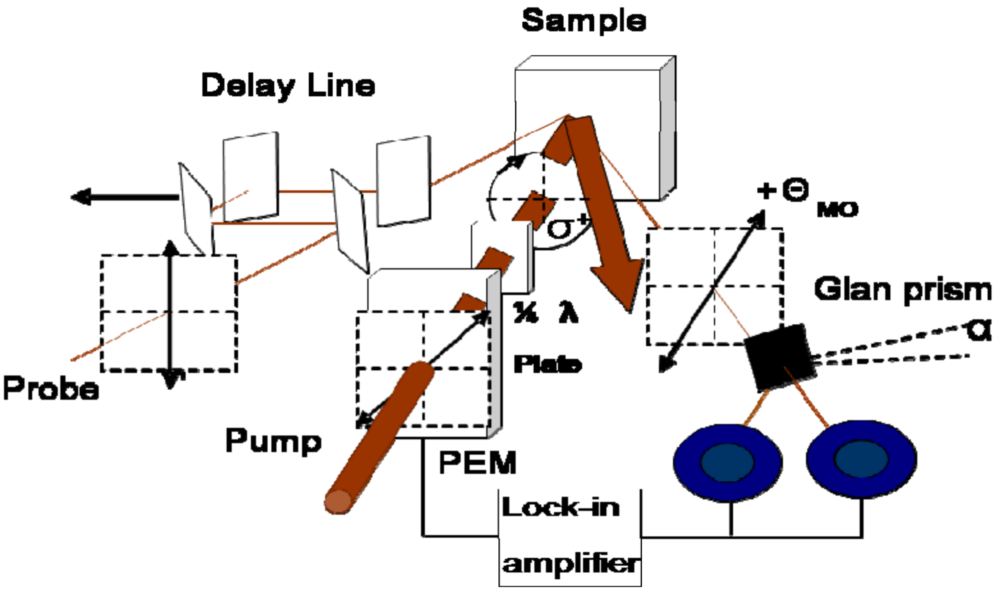

Fig. 2.19 The schematic diagram of TRKR.

TRKR measures the electron spin relaxation time in a semiconductor by recording the temporal change of a time-delayed, linearly-polarized “probe” pulse following a stronger (circularly-polarized) “pump” pulse. Fig.2.18 shows a photograph of our present setup. The schematic graph is shown in Fig. 2.19.

Electron spin dynamics is investigated by TRKR, using an experimental setup shown above. Both pump and probe pulses are generated by a tunable mode-locked Ti:sapphire laser with a pulse width of 130 fs and a repetition rate of 76 MHz. The angles of incidence of the pump and probe beams with respect to the sample normal are set to $\sim 20^{o}$ and $\sim 40^{o}$, respectively. These relatively large angles are chosen in order to minimize coherent contributions such as those observed in four-wave mixing experiments [7, 32]. A Glan-Laser Polarizer is used to split the reflected probe beam into two spatially separated components with orthogonal polarization directions. Two photodiode detectors in a bridge configuration are well adjusted to selectively detect the orthogonal probe signals. A photoelastic modulator (PEM) is used to modulate the pump amplitude at 100K Hz, while a chopper is used to modulate the probe at 5K Hz. Lock-in detection at the frequency difference allows us to remove background contributions to the signal coming from scattered pump light. The Kerr rotation experienced by the reflected delayed probe pulses is measured as a function of the delay time between pump and probe pulses.

To test the performance of this system, samples of semi-insulating GaAs were attached on glass substrates and placed at the convergence of pump and probe beams. Fig. 2.20 displays the absorption spectrum of one of our samples along with a TRKR curve at a wavelength close to the semiconductor energy gap. TRKR is a suitable in a number of situations the sample to be analyzed is grown on an opaque substrate that cannot be removed without compromising the integrity of the system, whereas a better signal-to-noise ratio could be obtained by time-resolved Faraday rotation (TRFR).

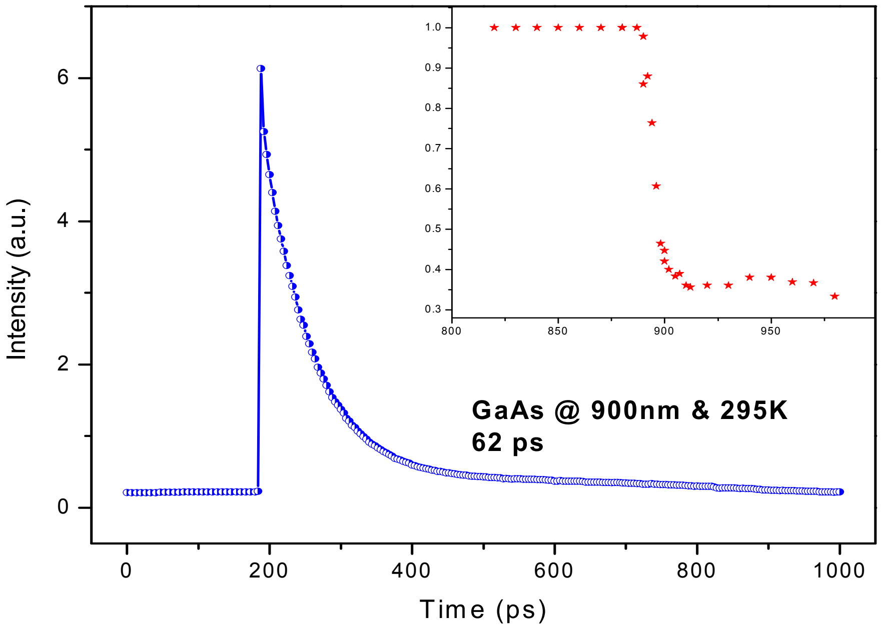

Fig. 2.20 TRKR measurement of the electron spin lifetime on a 50mm thick GaAs film at room temperature. The inset shows the absorption spectrum of the sample.

2.3.7 Optically pumped nuclear magnetic resonance (OPNMR)

Nuclear magnetic resonance (NMR) is a phenomenon that the nuclei of certain atoms, which are placed in a static magnetic field and exposed to an electromagnetic (EM) pulse, or a second oscillating magnetic field, absorb energy from the EM pulse and radiate this energy out back. It is a powerful probe of chemical structures, molecular conformations, molecular dynamics, electron and magnetic properties and phase transitions [11]. The principle limitation of NMR is its relative low sensitivity, especially in semiconductors of solid state. A second limitation of solid state NMR is the lack of spatial selectivity, i.e. the NMR signals from an inhomogeneous sample are bulk-average and it thus is difficult to assign particular spectral to particular regions within the sample. This limitation is pronounced when we study the interfacial, surface and cluster phenomena.

The interplay between the electron and nuclear spins provides a stage to enhance nuclear polarization and achieve NMR signals in selective domain by transferring photon angular momentum to nuclear spins, called optically pumped NMR (OPNMR) [33]. NMR signal are proportional to the nuclear spin polarizations, and optical pumping refers to the generation of large, nonequilibrium nuclear spin polarizations by optical excitation of electronic transitions. So it is possible in principle to enhance the NMR signal through optical pumping. It is also possible to area-selectively achieve enhanced NMR signal through spatial manipulations of the optical absorption.

As discussed in Chapter 2.3.6, it is possible to excite electron to conduction band with a spin polarization that is not is thermal equilibrium with the applied magnetic field (if any) at the temperature under investigation. One pathway by which the electron spin polarization can return to equilibrium involves mutual spin flip-flop transitions with the nuclei, e.g., processes in which an electron flips it spin orientation from m_j= -1/2 (valence band) to m_j= +1/2 (conduction band) and a nucleus simultaneously decreases it spin quantum number by one unit. These spin flip-flop transitions are driven by electron-nucleus hyperfine coupling. In this way, electron spin polarization is transferred into nuclear spin polarization and the nuclear spin polarization is driven out of thermal equilibrium. In the simplest case, the nuclear spin polarization can be pumped in either a positive or negative direction, leading to either enhanced absorptive or emissive signals in the NMR spectra.

Practically the mutual spin flip-flop transition may occur relatively infrequently, typically less than once for every 100 absorbed photons. However, there is no other strong mechanism for producing changes in the nuclear spin polarization in semiconductors, especially at low temperature. In other words, the nuclear spin-lattice relaxation time is very long (of order of ~10 minutes at RT and exceeding several hours below 80K, for CdTe). Therefore, the nuclear spin polarization can build up over many optical excitation cycles. The electron spin-lattice relaxation time is much short (of order of 10^{-10} second). However, as long as the electron spin relaxation time is comparable to or greater than the lifetime of the optically excited electronic state, the net electron spin polarization will have a nonequilibrium value, and optical pump of the nuclei occurs [11].

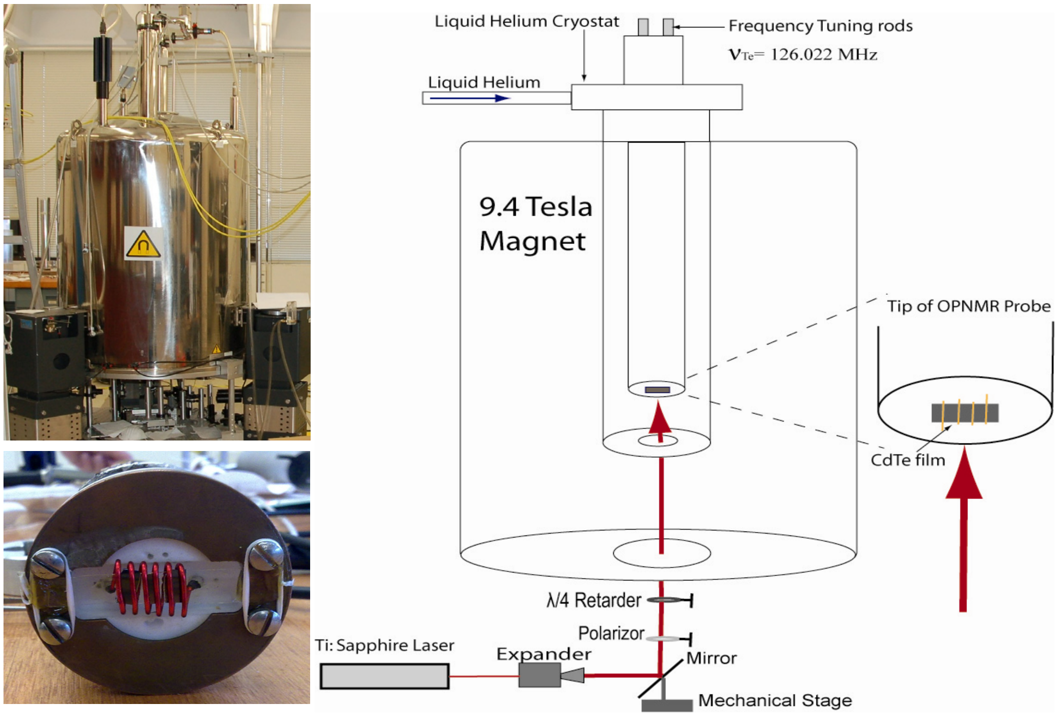

Fig. 2.21 Photos (left) and diagrams (right) of OPNMR and the probe.

Fig. 2.21 shows the photos and diagram of the equipment used for OPNMR. Most of the experimental works are carried out by my colleagues [34]. Optically enhanced NMR signal is collected in a 9.4 Tesla magnetic field. The sample is attached to a sapphire wafer to facilitate heat dissipation and a Cernox sensor is placed in its proximity to provide more extra temperature reading reference. A 5 W tunable Ti:sapphire laser is used for optical excitation, same to the one used for TRKR. Laser illumination is parallel to the direction of the magnetic field and perpendicular to the sample surface. A series of mirrors are used to steer the beam through a polarizer and 1/4 wave plate and two clear quartz windows, and onto the sample surface. The optical expander is used to vary the beam diameter from 0.5 to 3 mm. A homebuilt two-channel probe is used for all measurements, shown on the bottom left and the right in Fig. 2.21. Cryogenic capacitors allow us to tune and match the rf circuit down to 4 K and over a broad range of frequencies. The detailed experimental results and discussion will be presented in Chapter 6.

Chapter 3

Growth and characterization of (100) and (111) CdTe epilayers and related nanostructures

In this chapter, first we present the motivation of CdTe epitaxial growth. Then we present the (100) and (111) CdTe growth procedure in details. We believe that the different interfaces produced by the different shutter sequences, play an important role in the determination of the epitaxial layer's crystal orientation. We also discuss the possible growth parameters controlling the high quality CdTe epitaxial growth. Finally, we present the growth of CdTe related low dimensional structure CdTe/CdMgTe QWs and some characterization results are presented and discussed.

3.1 The motivation of CdTe growth

CdTe has been particularly attractive because of many promising applications in solar cells, gamma-ray detectors, electro-optic modulators and infrared detectors, due to its favorable optical properties and near-infrared direct band gap. Apart from this, CdTe is interesting for spintronics because it has the same crystal structure but different material parameters (e.g., effective masses or spin-orbit coupling) than the most often investigated III-V semiconductor GaAs. CdTe is also a promising material for the study of the generation of nonequilibrium nuclear spin polarization in solids by optical pumping. CdTe contains four spin -1/2 nuclear species in reasonable abundance: ^{123}Te(0.91%), ^{125}Te(7.14%), ^{111}Cd(12.8%), ^{113}Cd(12.22) and there is an increasing interest in the study of nonequilibrium nuclear spin polarization of CdTe by OPNMR [12, 35].

High quality CdTe growth is a key issue to investigate such phenomena and the crystal orientation might play an important role in such research. CdTe layers have been grown on (111) and (100) CdTe, (100) InSb, and (100) GaAs substrates by MBE [36]. Compared with the variability and generally low structural quality of CdTe wafers and costly InSb wafers, the GaAs substrate is an attractive substrate, because it is readily available, with high quality, at a low cost. However, reports to date are not consistent about the precise methods for growing reproducibly high quality single crystal (111) or (100) CdTe on (100) GaAs substrates.

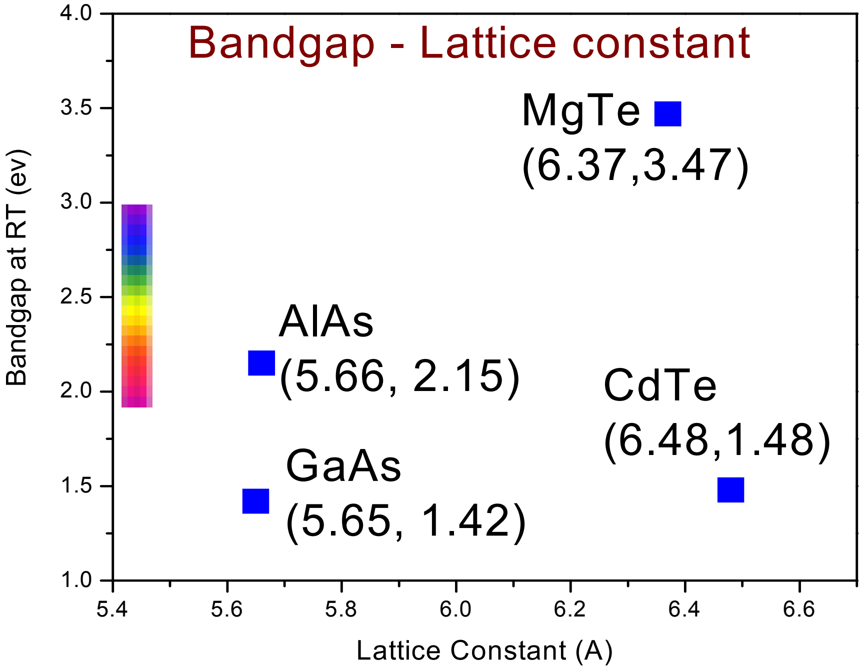

Fig. 3.1 Bandgap Vs. lattice constant for selected semiconductors.

It is known that for CdTe epilayers grown on (100) GaAs substrates both (100) and (111) orientations are probable, due to the large lattice mismatch (shown in Fig. 3.1), which makes it difficult to obtain single-domain CdTe films [37, 38]. It has been reported that substrate preparation, preheating and growth temperature have critical effects on the growth direction and interface structure during MBE of CdTe on (100) GaAs substrates [39-43]. It is also known that post growth thermal treatments have an influence on the final film quality and that low temperatures at the early stages of the heteroepitaxy may decrease intermixing [40, 41]. A distinct improvement in quality is found by raising the substrate temperature and by having excess Te in the incident flux [44].

Here, we take a different approach to address these concerns. We have modified the GaAs substrate on which we deposit CdTe by first depositing a ZnSe buffer layer on the GaAs crystals. This allows us to control the II-VI/III-V heterovalent epitaxy in a nearly lattice matched system, prior to growth of the highly mismatched CdTe deposition.

It is found that the deposition of CdTe on (100) ZnSe/GaAs quickly turns two-dimensional from the initial growth stages. We show that by changing the sequence of shutter operation used to initiate the CdTe growth, it is possible to stabilize either the growth of (100) or (111) CdTe epitaxial layers on the (100) ZnSe/GaAs substrate. Our results show that a continuous (uninterrupted) interface with various combinations of shutter sequences results in layers with (100) orientation, while an abrupt interface, achieved with a brief growth interruption between the CdTe and ZnSe layers, results in (111) CdTe. The substrate temperature then is increased 50 ^{o}C higher than the initial nucleation temperature and the growth is under Te-rich condition. Furthermore, our growth technique achieves high quality (100) or (111) CdTe epitaxial layers with ZnSe (100) buffer layer on (100) GaAs substrate without the use of post growth thermal treatments. The samples are monitored *in situ* by RHEED, and characterized post growth by SEM, PL and XRD measurements.

3.2 Experimental details of CdTe growth

CdTe layers were grown by MBE in UHV system featuring two Riber 2300 growth chambers, one devoted to III-V materials growth and the other to the growth of II-VI based heterostructures. As the general substrate preparation procedure, referred in Chapter 2.1, an epi-ready (100) GaAs semi-insulating substrate was mounted by Indium on a 2" moly-block and introduced in the III-V MBE chamber, where it was deoxidized under an As flux. The oxide desorption of the substrate was monitored by RHEED. Subsequently a 100nm GaAs epilayer was grown under As-rich conditions exhibiting a streaky (2×4) surface reconstruction, which is essential to obtain a good II-VI/III-V interface [14].

After the III-V buffer layer growth, the GaAs samples were transferred into the II-VI chamber via UHV transfer modules. Prior to growth of the II-VI layers, exposure to a Zn flux for a period of 20 s at 200°C was performed. This is expected to reduce the stacking fault density of the II-VI epilayer, which is related to the formation of undesired compounds between Se atoms and In or Ga atoms, such as Ga_2Se_3 [14]. This Zn exposure was followed by ~50Å of ZnSe at low temperature (200°C) to promote two-dimensional nucleation. Then the substrate temperature was increased to 300 °C for the remainder of the ZnSe layer growth. The ZnSe layer was grown using elemental sources of Zn and Se, under Se-rich growth conditions. The RHEED pattern exhibited a streaky Se-terminated (2×1) surface reconstruction during growth. This sequence of steps for the deposition of ZnSe on GaAs has produced high quality ZnSe layers with very low defect densities, as needed for device applications. The CdTe layer was grown from elemental sources of Cd and Te, typically under Te-rich growth conditions.

Initial trials showed that when CdTe growth was performed after a short (~2 sec.) interruption of the growth (by closing the main shutter) followed by the simultaneous opening of the Cd and Te shutters, we could obtain either (111) or (100) CdTe somewhat randomly (although a preference for (111) was observed). These initial layers exhibited full widths at half maximum (FWHM) of the x-ray rocking curves on the order of 1000 arcsec, indicating a relatively poor crystalline quality. Subsequently, we intentionally manipulated the shutter sequences in going from the ZnSe to the CdTe growth in an attempt to control the crystalline structure and quality of the CdTe layer.

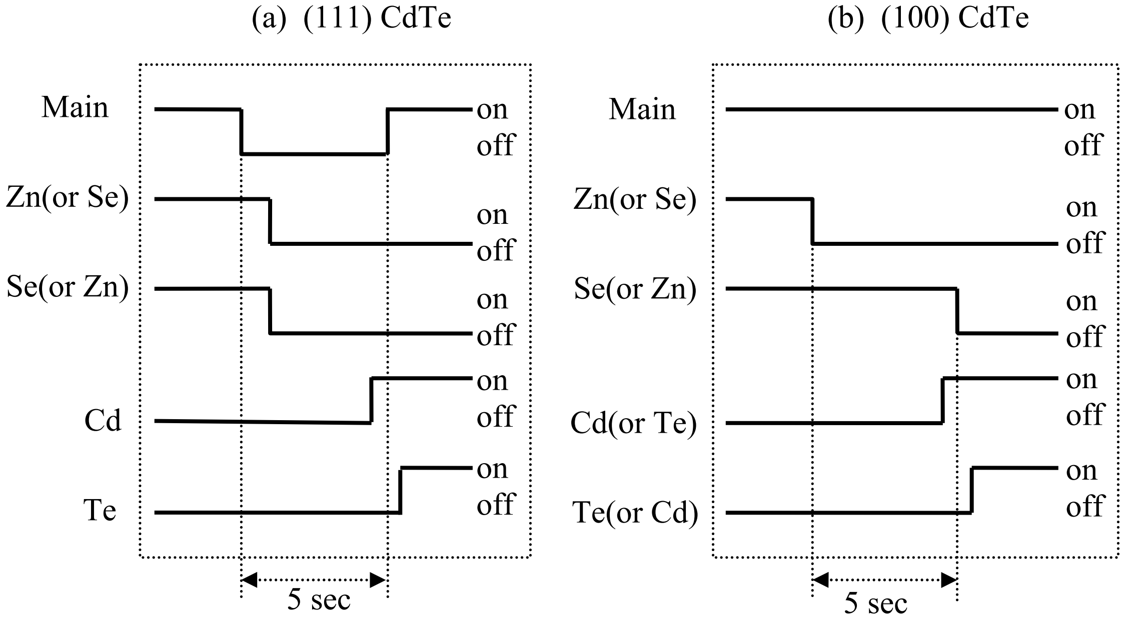

Fig. 3.2 Shutter operation sequences for selective growth of (111) and (100) CdTe on (100) ZnSe.

We first modified the interrupted growth process as illustrated in Fig. 3.2(a). We closed the main shutter for 5 seconds after completing the ZnSe buffer layer. Then we opened the Cd shutter, the main shutter and the Te shutter, sequentially. Such a shutter sequence always resulted in (111) CdTe. Once the Te shutter was open and CdTe growth was initiated, the substrate temperature was increased at a rate of 5°C/min to 350 °C. The

Cd and Te shutters were kept open for a period long enough to deposit a CdTe layer with a reasonable thickness for characterization (~2μm). To terminate the growth, the main shutter was closed and the substrate temperature was rapidly reduced to room temperature (RT). It should be noted that all the temperatures quoted were uncalibrated thermocouple readings.

In order to stabilize the (100) formation, a continuous interface, i.e., without a growth interruption, was necessary. For the uninterrupted growth, four shutter sequences were used to transition between ZnSe and CdTe, as illustrated in Fig. 3.2(b). The sequences were: 1 and 2) first closed the Se shutter after completing the ZnSe growth. This was followed by opening either the Cd or the Te shutter, which was followed by closing the Zn and lastly opening the Te or the Cd shutter; or 3 and 4) first closed the Zn shutter, which was followed by opening either the Cd or the Te shutter, then closed the Se shutter and lastly opened the Te or the Cd shutter (four combinations in total). In all cases, once the full shutter sequence was completed, the substrate temperature was gradually increased at a rate of 5°C/min to 350 °C, as in the interrupted growth sequence described above.

3.3 Characterization of CdTe samples

Our growth and characterization results are summarized in Table 3.1, including 4 samples grown by continuous shutter sequences and 3 samples grown by interrupted shutter sequences. The crystal orientation is obtained from SCXRD scans, while the X-ray FWHM relates to the DCXRD measurements. Thicknesses are measured directly from the SEM measurements and hereby the growth rate is calculated. The measurements will be discussed in details below.

Table 3.1 Summary of selected sample properties.

Sample #	Crystal Orientation	Shutter Sequence				Growth Rate (µm/h)	Thickness (µm)	DCXRD FWHM (arcsec)
		Close	Open	Close	Open			
A1	**100**	**Se**	**Cd**	**Zn**	**Te**	**1.4**	**2.2**	**740**
A2	**100**	**Se**	**Te**	**Zn**	**Cd**	**1.1**	**2.2**	**435**
A3	**100**	**Zn**	**Cd**	**Se**	**Te**	**1.0**	**2.0**	**310**
A4	**100**	**Zn**	**Te**	**Se**	**Cd**	**0.55**	**1.1**	**520**
B1	**111**	**Close Main, Close Zn & Se,**				**1.6**	**6.9**	**950**
B2	**111**	**Open Cd,**				**1.0**	**2.0**	**240**
B3	**111**	**Open Main, Open Te**				**0.25**	**1.5**	**220**

An inspection of Table 3.1 shows that the continuous growth shutter sequences result in (100) CdTe epilayers with reasonable FWHM of the DCXRD.On the other hand, the interrupted shutter sequences result in (111) CdTe epilayers, In both cases, growth rates greater than 1 µm/hr results in broad DCXRD peaks.

The RHEED patterns remained streaky during the transition between (100) ZnSe and (100) CdTe for the continuous shutter sequences, as shown in Fig. 3.3 (comparison of (a) with (c) along $[011]$ ZnSe azimuth and (b) with (d) along $[0\bar{1}1]$ ZnSe azimuth), but the separation between the rods was reduced by 86.8%, corresponding to a 13.2% lattice mismatch, which is slightly less than the expected 14.3% mismatch between bulk CdTe and ZnSe at RT. This may indicate the presence of in-plane compressive strain due to the pseudomorphic epitaxial growth, discussed in Chapter 2.3.1. The RHEED patterns remained sharp and streaky during the entire growth of the CdTe layer, indicating that the growth mode was preferred two dimensional for the entire growth procedure.

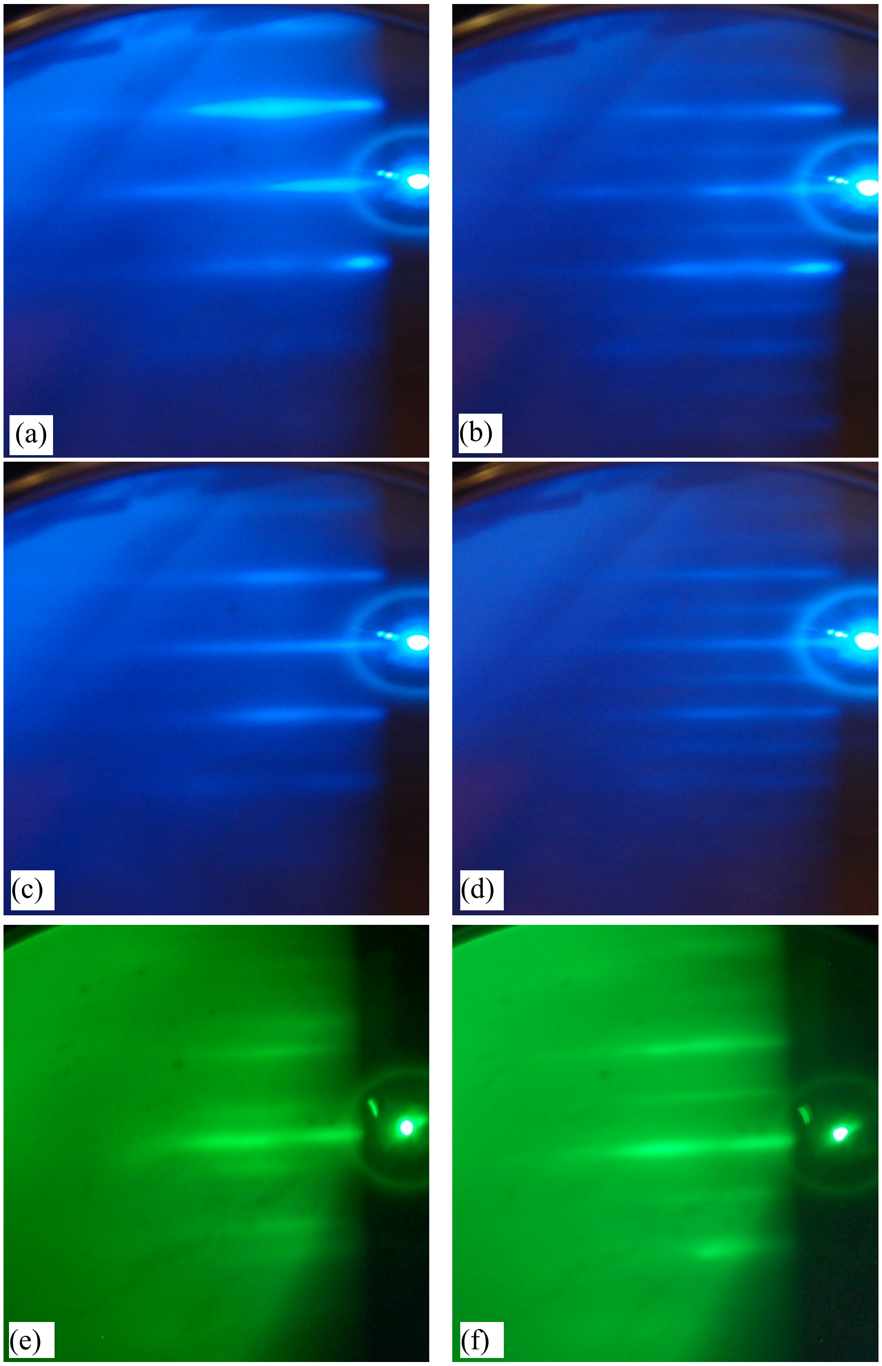

Fig. 3.3 The transitions of RHEED patterns for the (100) and (111) CdTe on (100) ZnSe. The RHEED patterns (a), (c) and (e) are taken along the $[011]$ ZnSe azimuth and (b), (d) and (f) are taken along the $[0\bar{1}1]$ ZnSe azimuth for ZnSe buffer, CdTe epilayers with continuous shutter sequence and interrupted shutter sequence, respectively.

For the interrupted growth sequence, the RHEED pattern shown in Fig. 3.3 (e) and (f) were taken along $[011]_{\text{ZnSe}}$ azimuth and $[0\bar{1}1]_{\text{ZnSe}}$ azimuth, respectively. We always observed that the RHEED patterns exhibited a 6-fold symmetry, meaning that the patterns repeated every 60°, which was typical for a (111) surface reconstruction. The observation was consistent with the $2\sqrt{3} \times 2\sqrt{3}$ R30° symmetry reported for the (111)B surface [19].

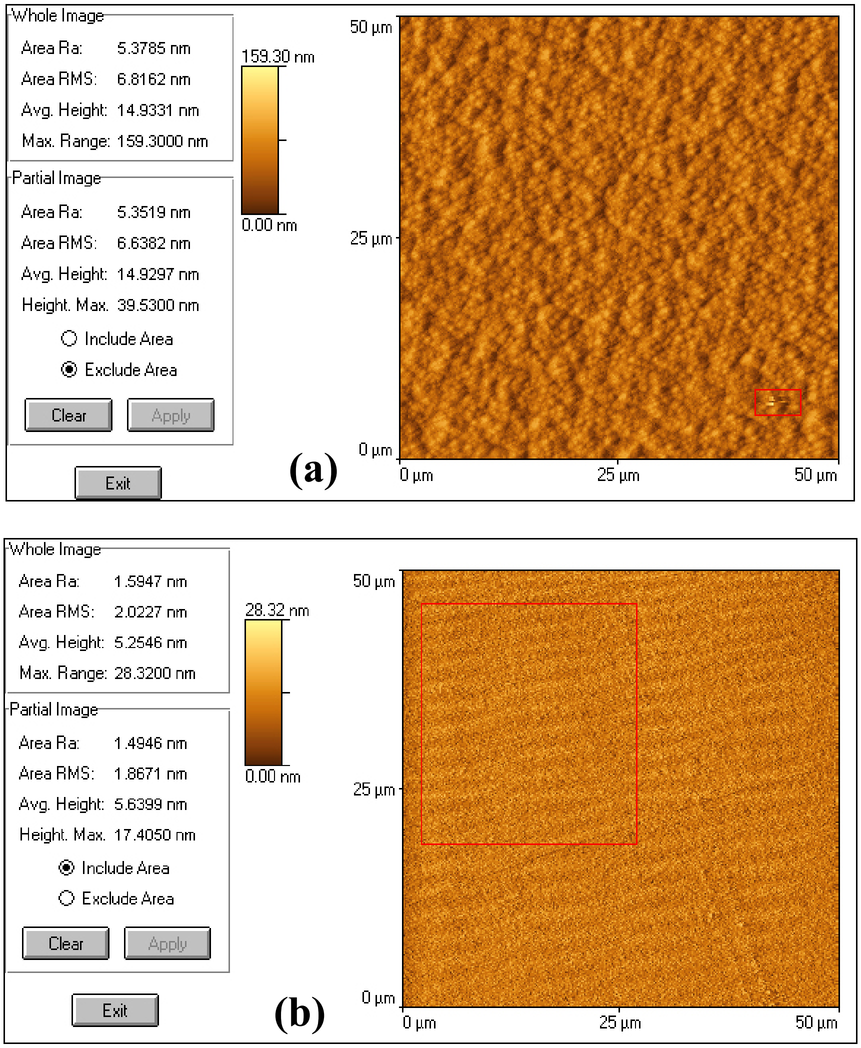

Whole Image
Area Ra: 5.3785 nm
Area RMS: 6.8162 nm
Avg. Height: 14.9331 nm
Max. Range: 159.3000 nm

Partial Image
Area Ra: 5.3519 nm
Area RMS: 6.6382 nm
Avg. Height: 14.9297 nm
Height. Max. 39.5300 nm
○ Include Area
● Exclude Area

Whole Image
Area Ra: 1.5947 nm
Area RMS: 2.0227 nm
Avg. Height: 5.2546 nm
Max. Range: 28.3200 nm

Partial Image
Area Ra: 1.4946 nm
Area RMS: 1.8671 nm
Avg. Height: 5.6399 nm
Height. Max. 17.4050 nm
● Include Area
○ Exclude Area

Fig. 3.4 AFM images for (a) A2 and (b) B2. The “Area RMS” of the whole and partial image are listed on the left information columns.

All layers exhibited mirror-like surfaces by eye. Average roughness (rms) of 8.0 nm for (100) CdTe and 2.5 nm for (111) CdTe were measured using AFM. The AFM images of A2 and B2 are shown in Fig. 3.4.

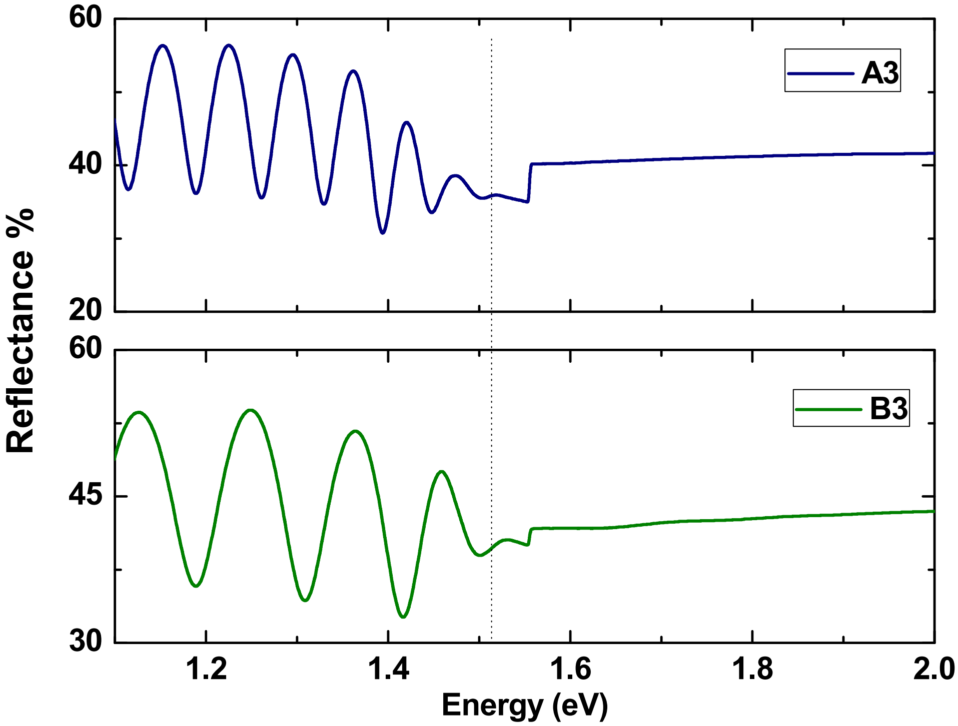

Fig. 3.5 Reflection spectra of sample A3 and B3. The dotted line indicates the energy 1.50 eV, corresponding to the band gap of CdTe at RT.

The samples were investigated using reflectance spectroscopy. The reflection spectra of A3 and B3, shown in Fig. 3.5, allow us to obtain preliminary information about the layer thickness and band gap. It works as a complementary measurement of SEM and PL. The calculated thicknesses of A3 and B3 are 2.24 and 1.53 μm, consistent with the measurement obtained by SEM. The dotted line indicates 1.51 eV, the band gap of CdTe at RT, consistent with the measurement of PL. The discontinuity in the spectrum at 1.55 eV (800 nm) is due to changing of the near infrared and visible optics.

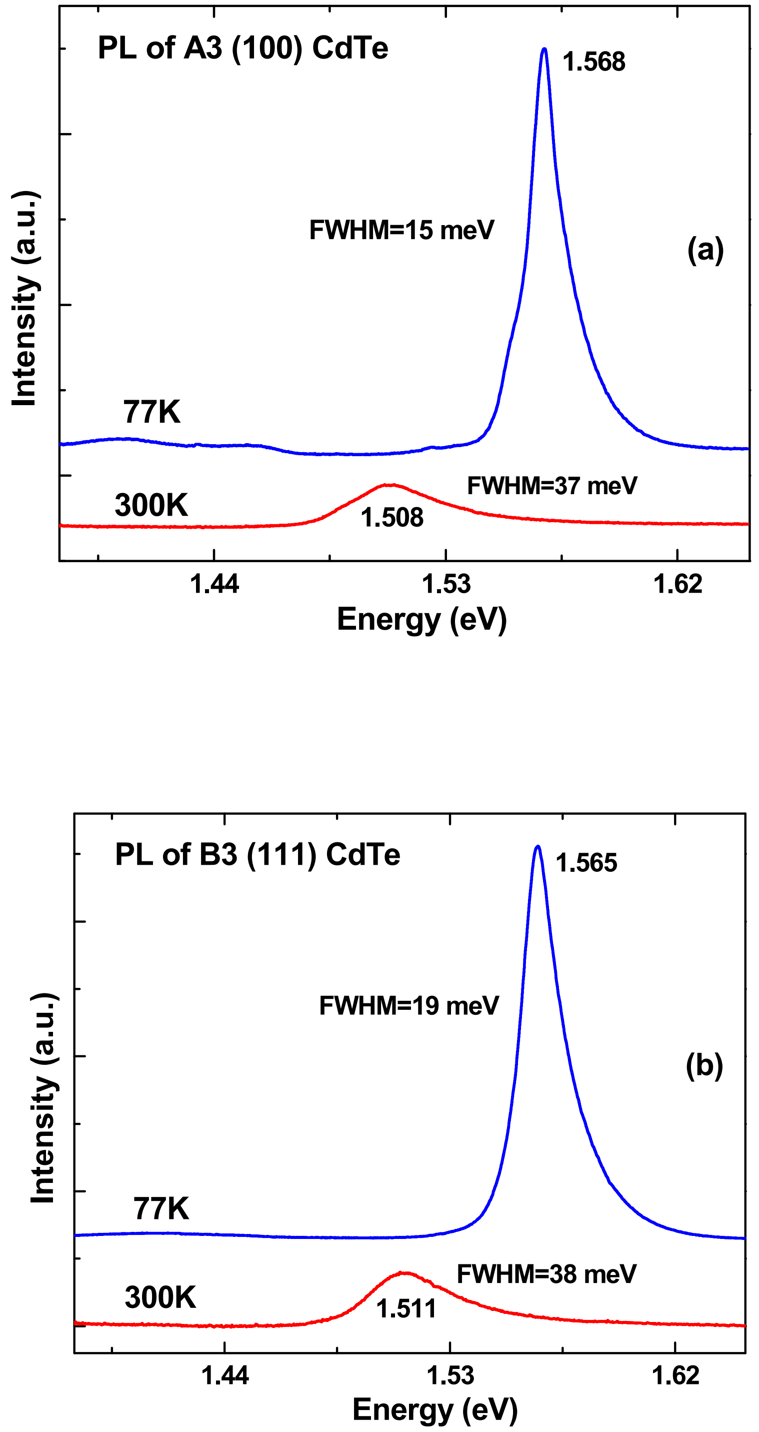

Fig. 3.6 PL spectra from A3 (100) and B3 (111) CdTe films at 300K and 77K.

Fig. 3.6 shows the PL spectra of a (100) CdTe layer and a (111) CdTe layers measured at RT and 77K, using the 633-nm line from a He-Ne laser as an excitation source. Strong and sharp PL emission was observed. The FWHM are 16 and 18 meV for the spectra of (100) and (111) CdTe films at 77K, respectively. The intrinsic FWHM expected for CdTe at 77K has been reported to be on the order of 10 meV [45]. The slightly broader peaks observed here suggest that the 77K PL peak around 1.57 eV may include contributions from impurity bound exciton peaks as well as the free exciton peak. A weak broad peak, possibly due to defects, was also observed for the (100) CdTe sample at 1.44 eV.

XRD measurements are used to characterize the structural quality of the samples. Fig. 3.7 shows the XRD ω-2θ scans of the (100) and (111) oriented CdTe films on (100)ZnSe/(100)GaAs heterostructures. In both cases, the copper $K\alpha_1$ and $K\alpha_2$ doublet for the (400) GaAs reflection is clearly resolved. While the (400) CdTe peak intensity is comparable to that of GaAs, the intensity of the (111) CdTe reflection is significantly stronger than the (400) GaAs peak. This is true even though the (111) CdTe and (100) CdTe layers have the same thickness of about 2μm

Shown in the insets are the double-crystal X-ray rocking curves for the CdTe layers with different orientation. For the same thickness layer and grown successively on the same day, the FWHM of a (111) CdTe sample is 220 arcsec, which is slightly narrower than that of (100) CdTe (310 arcsec). From comparing the rocking curves, (111) CdTe usually has a better quality than (100) CdTe. In both cases, the linewidths are among the best reported for CdTe layers grown on GaAs substrates. It should be noted that no post growth annealing or thermal treatments were used in these experiments.

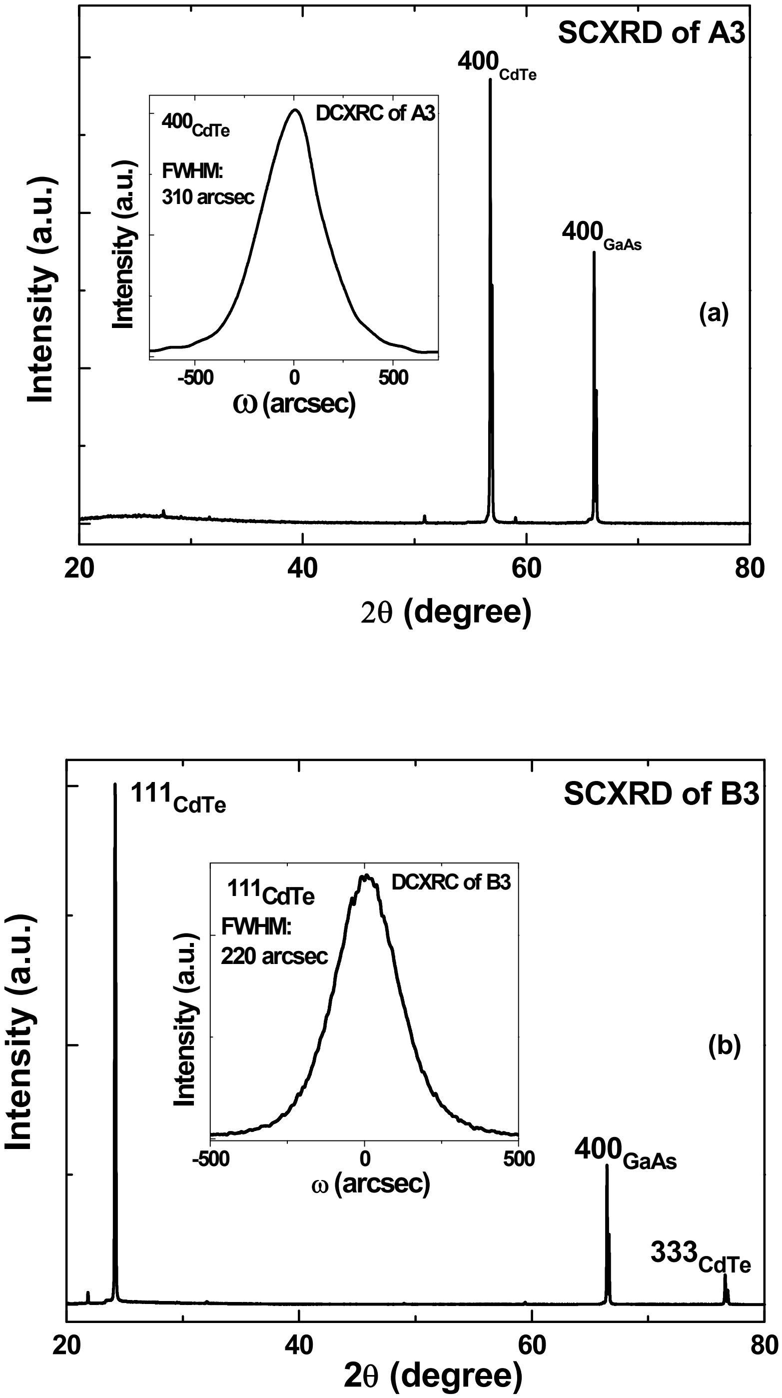

Fig. 3.7 XRD ω-2θ scans for (100) CdTe and (111) CdTe grown on (100) ZnSe/GaAs substrates. Insets are the double crystal rocking curves for (100) and (111) CdTe, respectively.

3.4 Discussion of the growth results

We believe that the achievement of high quality CdTe growth is due to the improvement of the II-VI/III-V interface quality obtained by inserting a ZnSe buffer layer. ZnSe/GaAs is an attractive substrate material for several reasons: (1) GaAs is readily available with high quality at a low cost, (2) ZnSe has a relatively small lattice constant mismatch with GaAs (0.25%) and has the potential to provide a close-to-ideal heterointerface, and (3) the surface preparation techniques for MBE growth of ZnSe on GaAs are well understood [46]. The early stages of growth of ZnSe were studied by monitoring the RHEED intensity oscillations, characteristic of layer-by-layer growth, which were observed for both ZnSe and CdTe nucleation.

The material quality is also improved by the gradual increase of growth temperature after the initial nucleation and the Te rich surface condition [44], while it is helpful to initiate the growth at a low initial temperature to reduce the intermixing [40, 41]. Note that there is no post growth annealing applied to the CdTe epilayers, although it is known that post growth thermal treatments have an influence on the final film quality.

Changes in the growth rate can also have a significant impact on the incorporation of background impurities and lattice defects, compositional homogeneity of alloy semiconductors, interface roughness of heterojunctions, and surface morphology. Usually lowering the growth rate leads to decreased FWHM of DCXRD curves, due to the enhanced surface migration at the lower growth rates. For the (111) CdTe layers, the FWHM of the DCXRD curves decreased from 950 to 220 arcsec when the growth rate decreased from 1.6 to 0.25 μm/h, although there was no significant change of width when the growth rate varied between 1.1 and 0.25 μm/h. The narrowest linewidths for the (100) CdTe layers was also achieved for growth rates of ~1.0 μm/h.

Fig. 3.8 compares the interlayer lattice geometries of the top CdTe (circles) and the underlying ZnSe (dots) for the two types of heteroepitaxies. The continuous-growth interfaces produce mixed-alloy layers at the interface, as shown in Fig. 3.8(a), which may provide an alternative way to alleviate the strain at the interface allowing the layer to maintain the (100) orientation of the underlying layer and substrate.

On the other hand, the abrupt transition between the two materials, obtained with the growth interruption, leads to the formation of the less mismatched (111) CdTe orientation on the (100) ZnSe, shown in Fig. 3.8(b). For the growth of (111) CdTe on (100) ZnSe/GaAs, the $[\bar{2}11]$ CdTe direction is aligned with the nearly matched $[011]$ GaAs direction. The remaining lattice mismatch is 0.7% in this direction. In the perpendicular direction $[0\bar{1}1]$ CdTe $\parallel$ $[0\bar{1}1]$ GaAs one is left with the total 14.6% misfit [15]. By this special alignment between the (111) CdTe and the (100) substrate there is a reduced lattice mismatch between the layer and the substrate.

From Fig. 3.8 it is also evident that, in the case of (100) CdTe on (100) ZnSe, the in-plane mismatch is isotropic, leading to an isotropic in-plane strain, which could be related to the temperature dependence of electron spin relaxation. On the other hand, the in plane mismatch is anisotropic for the case of (111) CdTe on (100) ZnSe. This characteristic may be related to the temperature independence of electron spin relaxation in these samples, as will be discussed in the next chapter.

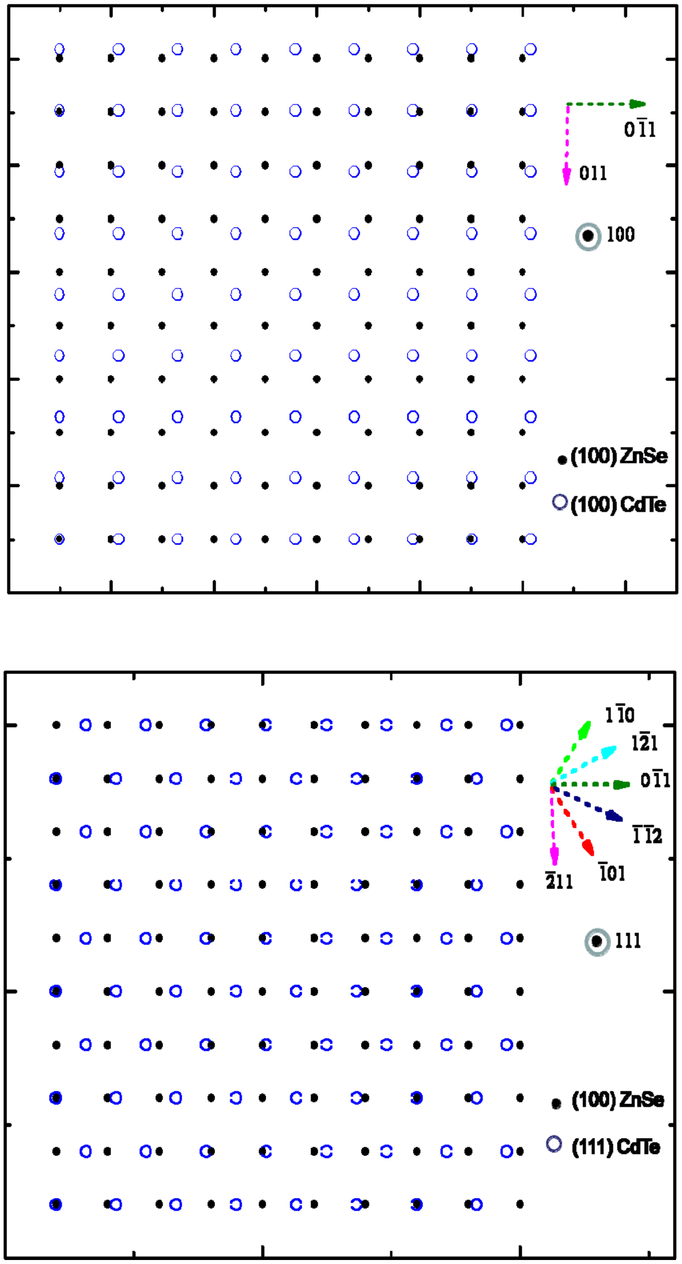

Fig. 3.8 The interlayer lattice geometries of the top CdTe (circles) and the underlying ZnSe (dots). In the case of (a) (100) CdTe, the in-plane mismatch is isotropic, while it's anisotropic for (b) (111) CdTe. The directions are based on the top CdTe lattice sites.

Although more detailed investigation of the interface phenomena and strain and defect analysis of the layers are needed to fully understand the reasons for the structural selectivity of the CdTe layer using our different shutter transition sequences, we believe that the abrupt transition between the two materials, obtained with the growth interruption, leads to the preferred formation of the less strained (111) CdTe orientation on the (100) ZnSe, while the intermixed interface of the continuous growth allows the (100) CdTe growth on the (100) ZnSe surface.

3.5 Growth of CdMgTe epilayers and CdTe/CdMgTe QWs

High quality CdMgTe epilayers as barrier materials are essential for subsequent CdTe/CdMgTe QWs studies. Fortunately, the similar lattice constants of CdTe and MgTe allow us to adjust the Mg composition continuously, avoiding the issue of lattice mismatch between the ternary and the binary epilayers. Following a similar procedure to the growth of CdTe, we have grown (100) and (111) CdMgTe epilayers on (100) GaAs substrates with CdTe/ZnSe buffer layers and a CdTe cap layer. Within each crystal orientation, the RHEED pattern of CdMgTe ternary epilayer remains the same as that of the CdTe binary epilayer.

Fig. 3.9 shows SCXRD of a 0.9 μm thick (100) CdMgTe and a 0.5 μm thick (111) CdMgTe epilayers. As shown in the insets, the FWHM of DCXRD rocking curves are 900 and 1000 arcsecs for (100) and (111) CdMgTe epilayers, respectively. The lattice constant from SCXRD is $C_{(CdMgTe)}$= 6.463 Å. The ternary layer composition $Cd_{(0.85)}Mg_{(0.15)}Te$ could be deduced by the lattice constants of binary layers of CdTe and MgTe.

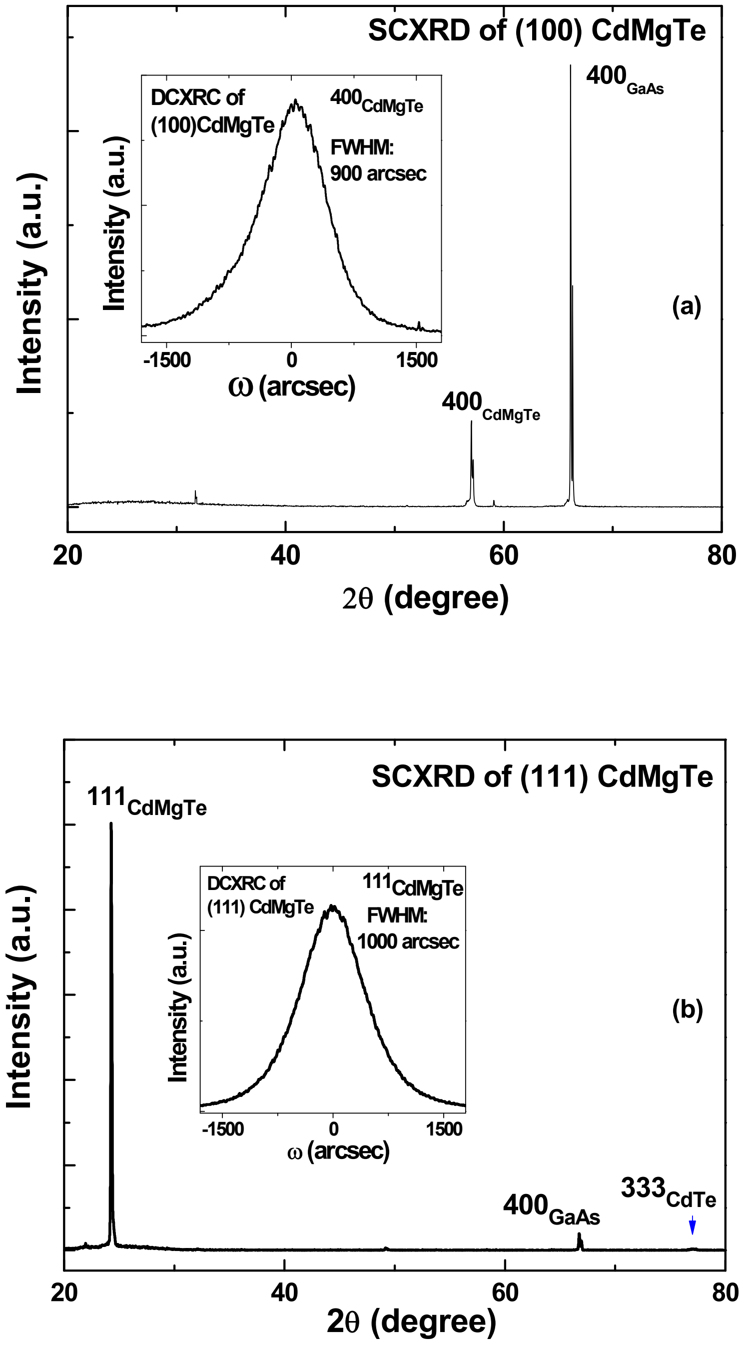

Fig. 3.9 XRD ω-2θ scans for (100) CdMgTe and (111) CdMgTe grown on (100) ZnSe/GaAs substrates. Insets are the double crystal rocking curves for (100) and (111) CdMgTe, respectively.

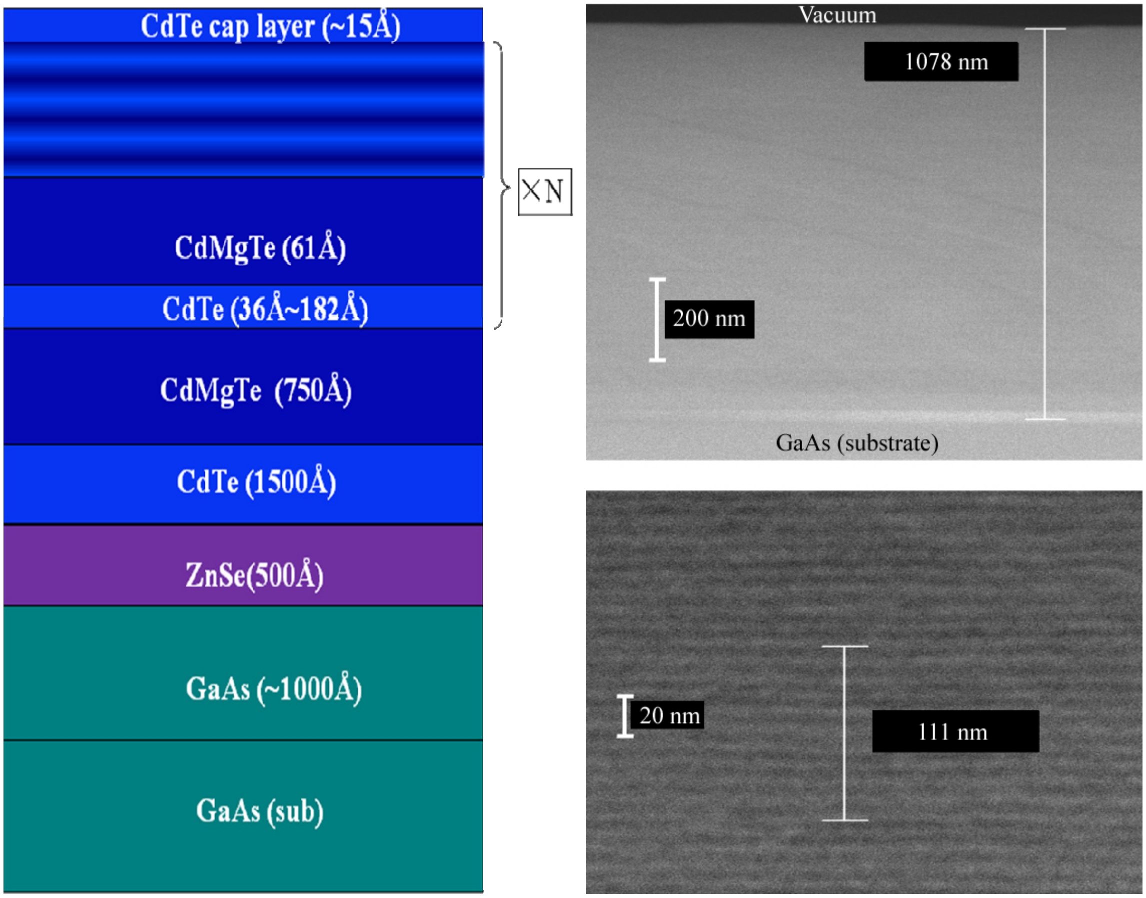

(a) (b)

Fig. 3.10 (a) Schematic of structure of CdTe/CdMgTe QWs, and (b) the SEM of CdTe (45 Å)/CdMgTe QWs in different magnifications.

Since both well material CdTe and barrier material CdMgTe have been grown and calibrated, we successfully grew a set of (100) CdTe/CdMgTe QWs structures on (100) ZnSe/GaAs substrates by MBE, with barrier thickness of 61 Å and different well thicknesses of 36, 45, 64, 91 and 182 Å. Fig. 3.10(a) shows the schematic structure. Based on the barrier material composition $Cd_{0.85}Mg_{0.15}Te$ (band gap 1.78 eV, 698nm), the well thickness is designed for the emission in the range of our TRKR setup (within 700 ~ 1000 nm). The number of repeats, N, are 125 for 36 Å well, 100 for 45 Å, 71 for 64 Å well, 50 for 91 Å well, and 25 for 182 Å well. They are chosen to keep the same overall amount of CdTe well material.

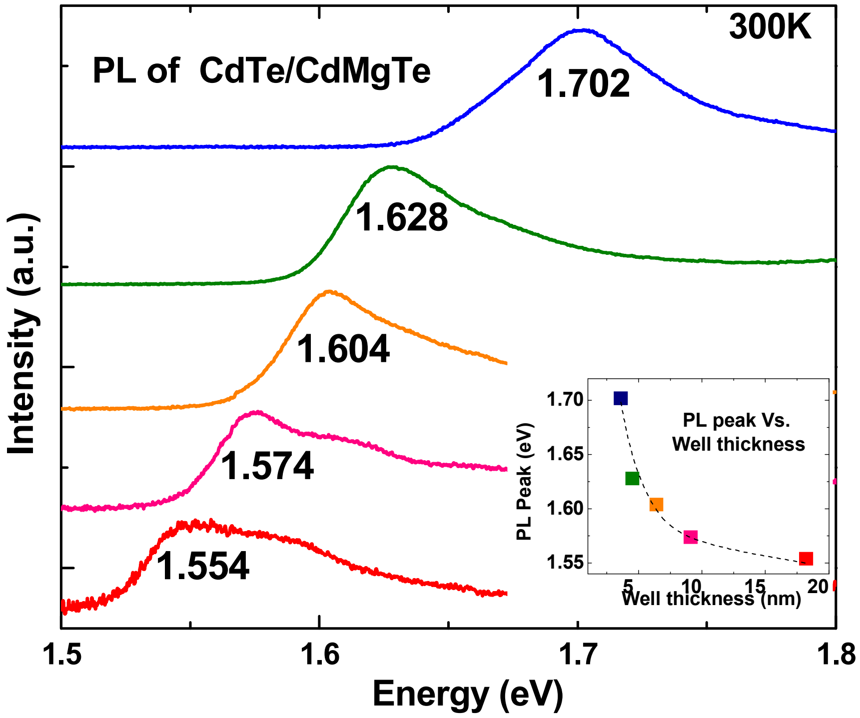

Fig. 3.11 PL of CdTe/CdMgTe QWs with well thickness of 36, 45, 64, 91 and 182 Å, from top to bottom, respectively. The peaks are plotted in the inset as a function of well thickness. The dashed line is the fitting result according to the inverse square law.

In Fig. 3.10(b) are shown the SEM images for a CdTe/CdMgTe QWs with well thickness of 45 Å. The layered structure can be seen clearly at the higher magnification (212K), showing high structural quality of CdTe/CdMgTe QWs. The measured period is 111 Å, which indicates the thickness of barrier is 65 Å, consistent with the design.

We also perform the PL measurements of the CdTe/CdMgTe QWs at RT, shown in Fig 3.11. The PL peak is plotted as a function of the well thickness, shown in the inset of

Fig 3.11. It decreases with the increasing well thickness, following the well thickness inverse square law.

In a conclusion of this chapter, we have grown (100) and (111) CdTe epilayers on (100) GaAs substrates with (100) ZnSe buffer layers by MBE. By subsequently adjusting the interface between ZnSe and CdTe, it is possible to selectively obtain the growth of either (100) or (111) CdTe epitaxial layers on the (100) ZnSe/GaAs substrate. RHEED indicates that the nucleation of the CdTe epitaxial layers quickly turns two-dimensional from the onset of growth. XRD and PL measurements indicate that both the (111) and the (100) CdTe films are of high structural quality despite the large lattice constant mismatch of 14.3% between CdTe and ZnSe. By improved CdTe growth techniques, we also grew and characterized low dimensional nanostructures of these materials, such as CdTe/CdMgTe QWs.

Chapter 4

Electron spin relaxation dynamics in CdTe epilayers

In this chapter we investigate the electron spin relaxation dynamics of (111) and (100) CdTe epilayers by TRKR, compared with bulk CdTe. For the (111) CdTe, spin relaxation rate τ_s^{-1} is significantly enhanced relative to that of bulk CdTe and shows no temperature dependence through 130K to 300K, while it is nearly unchanged for the (100) CdTe. The temperature dependence of $\tau_s^{-1} \propto T^{1.3}$ is found for (100) CdTe, compared with $\tau_s^{-1} \propto T^{2.3}$ for bulk CdTe. We ascribe these differences to the presence of residual anisotropic strain in (111) CdTe, making this the first experimental observation of the effect of strain on τ_s^{-1} in a II-VI semiconductor material. It is also found that τ_s^{-1} is dependent on material quality for both (111) and (100) CdTe. Residual strain and dislocations can enhance the spin relaxation rates through the Elliott-Yafet mechanism. We discuss the effect of strain on spin relaxation time of CdTe based on the theoretical models.

4.1 Background of electron spin lifetimes in CdTe epilayers

There is a great interest in the study of spin dynamics of electrons in semiconductors, due to the potential applications for spintronic devices and quantum computation [4]. Spin relaxation dynamics is one of the key features in spin-related phenomena, and has been found to vary over a wide range from a few picoseconds up to tens of microseconds [7, 47, 48]. Until recently, extensive investigations have been carried out in III-V semiconductors, especially in GaAs-based structures, while far less was done in II-VI semiconductors [6].

CdTe is a II-VI semiconductor that has been used in X-ray and gamma-ray detectors and optoelectronic devices, due to its favorable optical properties and near-infrared direct band gap. CdTe is also a potential material for spintronics because it has the same crystal structure and different material parameters (e.g., lattice constant, effective masses, spin-orbit coupling) than III-V semiconductors. There are some reports of the spin dynamics by TRKR measurements at RT on bulk CdTe [6, 7], but the reports are not consistent. For example, the relaxation time (2.5ps) reported in Ref. [7] is more than 20 times less than that (52ps) in Ref. [6]. To get a better understanding of spin relaxation dynamics of CdTe, we characterize bulk and epitaxial CdTe semiconductors by TRKR.

4.2 Experimental observation of electron spin relaxation of CdTe semiconductors

Table 4.1 Summary of selected samples for TRKR.

Sample number	**Crystal Orientation**	**FWHM of DCXRD (arcsec)**	**PL @ 300K (eV)**	τ_s^{-1} **@ 300K (ns^{-1})**	τ_s^{-1} **@ 130K (ns^{-1})**
A1	**100**	**745**	**1.509**	**59**	**13**
A2		**435**	**1.509**	**31**	**9**
A3		**310**	**1.508**	**23**	**6**
B1	**111**	**950**	**1.514**	**77**	**83**
B2		**240**	**1.514**	**67**	**55**
B3		**220**	**1.511**	**30**	**26**
Bulk	**111**	**N/A**	**1.489**	**18**	**2**

CdTe layers used in the experiments are grown on (100) GaAs substrate by MBE in our laboratory. ZnSe buffer layers are used to control the CdTe crystal orientation and improve the quality. (100) and (111) CdTe epilayers with different structural qualities are obtained by varying the growth parameters. The samples are characterized in our group showing high crystalline quality. Some measurements of selected samples we employ in this chapter are listed in Table 4.1, as a complementary part of Table 3.1, referred in the prior chapter.

The schematic electronic band structure of CdTe near the Γ point and absorption transitions with circularly polarized light are shown in Fig. 2.17. The experimental details and the physics were discussed in Chapter 2.3.6. Electron spin dynamics was investigated by TRKR, using the experimental setup shown in Fig. 2.19.

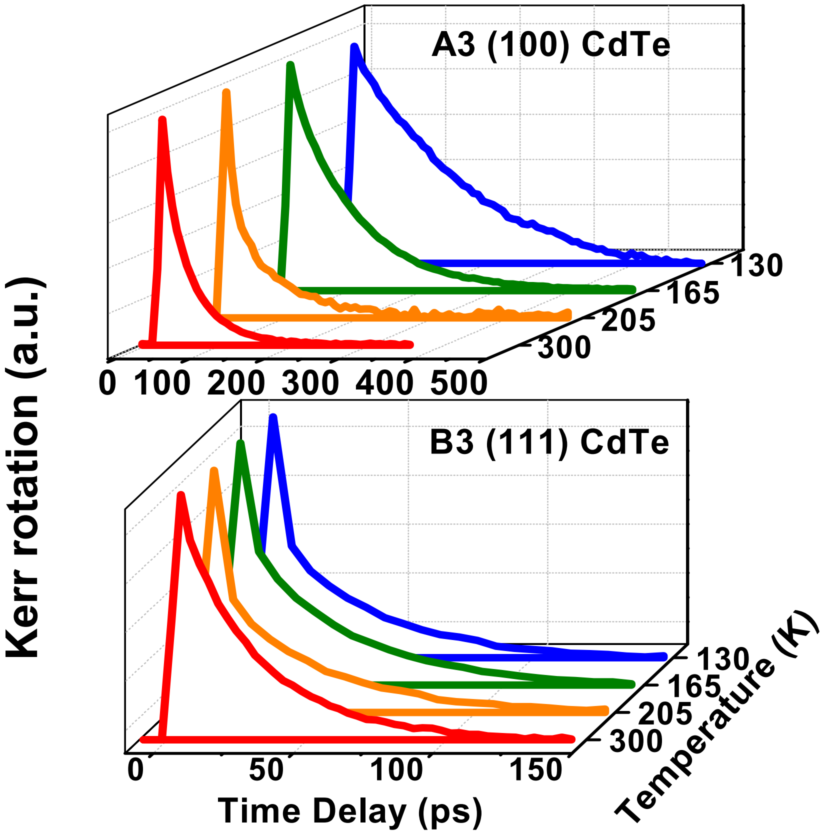

Fig. 4.1 Kerr rotation measurements for (100) CdTe and (111) CdTe at different temperatures by TRKR.

The normalized Kerr rotation θ_K curves of CdTe samples for optical excitation band-gap energy at different temperatures are shown in Fig. 4.1. The change of the polarization state of the probe pulse upon reflection from the optically excited sample is described by $\varepsilon_K + i\theta_K \propto \int dt E^*(t)[P^{++}(t) - P^{--}]$, where ε_K is the Kerr ellipicity and θ_K is the Kerr rotation. The nonlinear polarization $P^{++} = P_x + iP_y$ and $P^{--} = P_x - iP_y$ are linear functions of the probe optical electric field and a quadratic function of the optical electric field of the right-handed and left-handed polarized pump pulse [49, 50]. In the temperature range between 130K and 300K, a strong temperature dependence is observed only for (100) CdTe and not for (111) CdTe layers. Note that the much larger scale range of time delay for A3 (100) CdTe.

Two independent exponential decays are necessary to fit the observed Kerr rotation curves. The faster relaxation component, in the range of a few picoseconds, dominates the signal just after the zero delay time (when pump and probe pulses coincide in time at the sample surface). This component can be related to the process of thermalization in the electron-hole plasma that follows the excitation pulse, i.e., the quick emission of longitudinal optical phonons to release the excess energy [51]. The slower component τ_s^{-1} is plotted in Fig. 4.2 as a function of temperature for the (111) and (100) films and for a (111) CdTe crystal used as a reference.

We observe that the spin relaxation rate is systematically faster in the epilayers than in bulk material. While τ_s^{-1} in the (100) films exhibits a noticeable temperature dependence ($\tau_s^{-1} \sim T^{1.3}$) resemblant of that observed in bulk ($\tau_s^{-1} \propto T^{2.3}$), the relaxation rate remains unchanged in the (111) epilayers ($\tau_s^{-1} \propto T^0$) over the temperature range investigated.

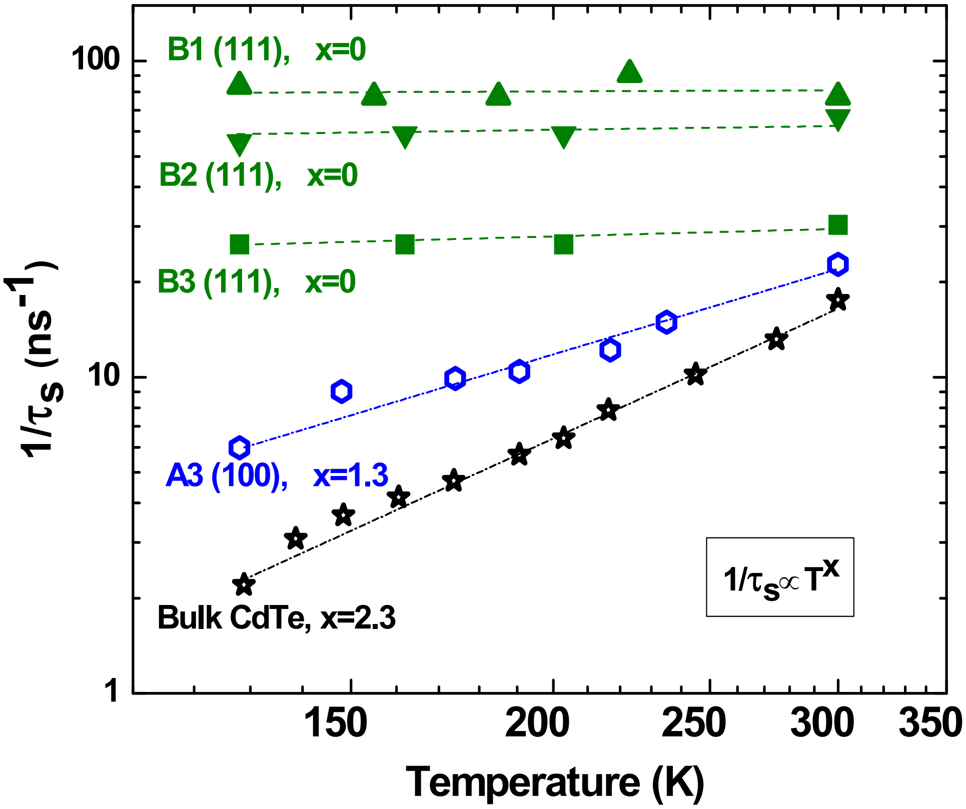

Fig. 4.2 The plot of spin relaxation rate τ_s^{-1} as a function of temperature T of CdTe measured by TRKR.

As shown in Fig. 4.3, where the spin relaxation rate τ_s^{-1} for the CdTe films with different FWHM of DCXRD are compared, τ_s^{-1} increases with the increasing FWHM of DCXRD for both (111) and (100) CdTe. Although the difference in FWHM is very small (20 arcsec) the change in τ_s^{-1} for (111) CdTe is about a factor of 2 between the two samples (B2 and B3).

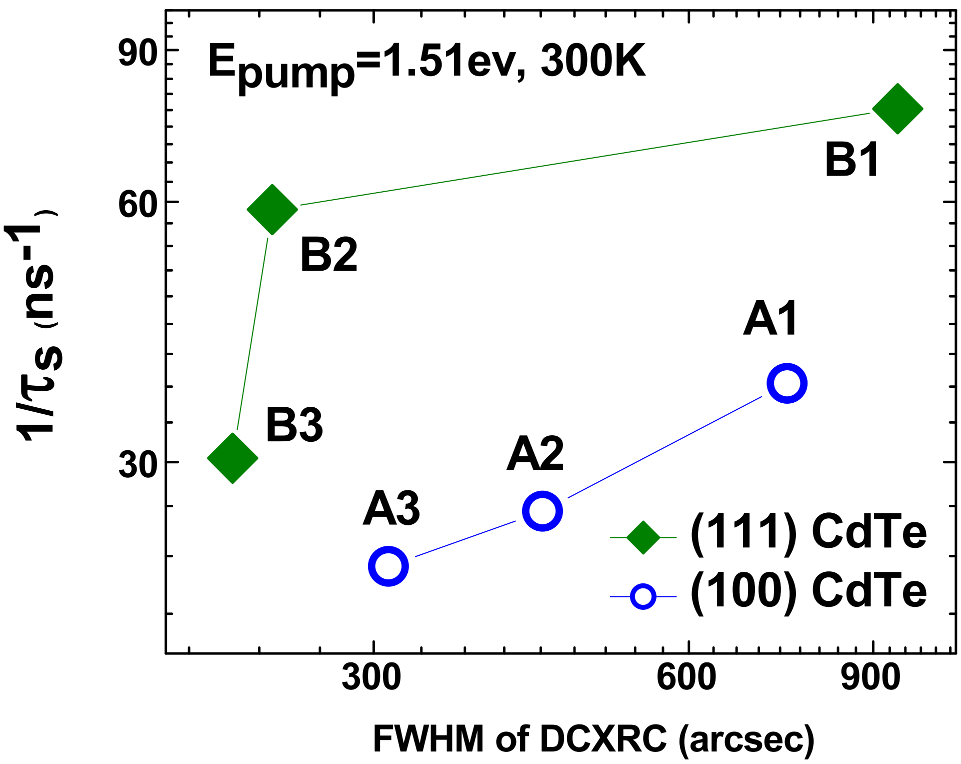

Fig. 4.3 The plot of τ_s^{-1} as a function of FWHM of DCXRD, showing that τ_s^{-1} increases with increasing FWHM of DCXRD for CdTe films of both orientations.

4.3 Analysis of the dependences of spin relaxation on temperature and material quality

It has been reported that compressive strains exist near the interfaces in CdTe layers thinner than 2 μm [52, 53]. For the (111) CdTe epitaxial layer nucleation the crystal lattice rotates to a minimum mismatched position relative to the underlying surface: $[\bar{2}11]$ CdTe ∥ [011] ZnSe/GaAs substrate, in which direction the lattice sites overlap nearly exactly on alternate along the $[\bar{2}11]$ direction producing a an effective lattice mismatch +0.7%, and $[0\bar{1}1]$ CdTe ∥ $[0\bar{1}1]$ ZnSe/GaAs substrate, in which direction the total -14.6% remains, with one missing (111) lattice site for every seven sites in the underlying (100) lattice.

This case is illustrated in Fig. 3.8(b), resulting in anisotropic in-plain strain configuration in (111) CdTe epilayer. The blue shifts of the PL emission peaks summarized in Table 4.1 are consistent with the strain effects [54]. The RHEED patterns remained streaky during the transition from (100) ZnSe to (100) CdTe, as shown in Fig. 3.3 (a)→(c) and (b)→(d), but the separation between the rods was reduced by 86.8%, corresponding to a 13.2% lattice mismatch, which is slightly less than the expected 14.3% mismatch between bulk CdTe and ZnSe at RT, as well indicating the strained surface geometry. We propose that the effect of these residual strains is causing the observed electron spin dynamics.

Strain-engineered heterostructures provide a powerful means of systematically designing internal magnetic fields, thus yielding means to manipulate spins through spin-orbit coupling induced by strain in crystals [55]. To get a better understanding of the effect of strain on relaxation time, by the methods employed in Ref. [56], we obtain $\tau_s^{-1} = \tau_{s0}^{-1} + \tau_{st}^{-1}$, where τ_{s0}^{-1} is the isotropic spin relaxation rate in the absence of strain, and τ_{st}^{-1} is the strain induced spin relaxation rate. Furthermore, we can express

$$\tau_{s0}^{-1} = q\alpha^2 (\kappa T)^3 \tau_p / \hbar E_g \qquad (1)$$

where q is a numerical factor which depends on the scattering mechanism, κ is the Boltzmann constant, T is the temperature, τ_p is the average relaxation time derived from the electron mobility, $\hbar$ is the reduced Planck constant, E_g is the width of the forbidden gap and $\alpha = \frac{4m_e}{3m_{cv}} \frac{\Delta}{(E_g + \Delta)} (1 - \frac{\Delta}{3(E_g + \Delta)})^{-1/2}$, where m_e is the electron effective mass,

m_{cv} is a parameter of the conduction band and valence band and Δ is the spin-orbit splitting energy, and

$$\tau_{st}^{-1} = A\frac{E_k \kappa T \tau_p}{2\hbar^2 C_{44}^2} P^2 \qquad (2)$$

where E_k is the electron kinetic energy, P is the strain tensor for the stress, C_{44} is the elasticity modulus and $A = n_x^2 n_y^2 + n_x^2 n_z^2 + n_y^2 n_z^2$ and n is a unit vector along the strain axis.

In the case of (100) CdTe, $n \parallel \langle 100 \rangle$, $A = 0$, and the strain has no effect on the spin relaxation. On the other hand, in the case of (111) CdTe, $n \parallel \langle 0\bar{1}1 \rangle$, $A = 1/4$, and with increasing stress, the strain-induced contribution τ_{st}^{-1} increases fast. With a certain value of the stress P, τ_{st}^{-1} can be comparable or even larger than τ_{s0}^{-1}, Therefore, the sum of them τ_s^{-1} of (111) CdTe behaves differently from strain-free bulk materials.

The influence of dislocation defects to electron spin dynamics in bulk CdTe at room temperature was investigated, and a weak but clear decrease of the electron spin lifetime (from 52 to 36 ps) with the increased concentration of defects was observed [6]. Their results are comparable to ours at room temperature. Although there are some reports that the temperature dependence of spin relaxation time faded due to the defect-related structural and electronic environment of localized carriers [57-59], we believe that the dominant contribution to the temperature dependent spin relaxation is from the strain, because the higher structural quality sample B3 (of less dislocation) shows temperature robust behavior while lower structural quality sample A3 (of more dislocation) exhibits a temperature dependence.

It is known that the D'yakonov-Perel (DP) mechanism dominates the spin relaxation at RT in undoped semiconductors without the inversion symmetry in the high temperature range between 130 and 300 K. However, with greater spin-orbit splitting to bandgap ratio, referred in Fig. 2.17(a), the Elliot-Yafet (EY) mechanism can become dominant. The ratio of CdTe (E_g=1.61eV, Δ_{so}=0.92eV at 4K) is more double than that of GaAs (E_g=1.52eV, Δ_{so}=0.34eV at 4K) [60]. The EY mechanism indicates that the spin relaxation rate increases with increasing dislocation, which is consistent with the plot in Fig. 4.3. Consequently, the EY mechanism can be dominant when the dislocation density is comparable large, as observed recently in wurtzite GaN [61]. The EY mechanism can also play an important role of this temperature dependence, whose efficiency process is inversely proportional to the temperature, far less affected by the temperature than that of DP mechanism [62, 63].

Another contribution to the change of spin dephasing times might be from Bir-Aronov-Pikus dephasing mechanism, which usually plays a more important role in heavily p-doped semiconductors [46]. Although the CdTe layers show high resistance through Hall effect measurement and are not intentionally doped, the intrinsic CdTe is p-type under Te-rich condition, with the Cd vacancy as the dominant acceptor and the Te antisite as the compensating donor [64]. Another possible explanation for this $\tau_s^{-1} \propto T^{1.3}$ temperature dependence of (100) CdTe epilayers can be related to the carrier lifetime, because temperature dependence of them behaves same trend [65, 66].

In conclusion, we have investigated electron spin relaxation dynamics at different temperatures by TRKR measurements on the bulk CdTe and CdTe epilayers with different crystal orientation. For the (111) CdTe films, the spin relaxation rate τ_s^{-1} is significantly enhanced relative to that of bulk CdTe and shows no temperature dependence through 130K to 300K. On the other hand, the (100) CdTe films show temperature dependence $\tau_s^{-1} \propto T^{1.3}$ resemblant to $\tau_s^{-1} \propto T^{2.3}$ observed in bulk CdTe. It is also found that τ_s^{-1} is dependent on material quality for both (111) and (100) CdTe films. We ascribe these differences to the presence of dislocations and residual strain, enhancing the spin relaxation rate mainly through the EY mechanism.

Chapter 5

Growth and characterization of ZnTe/ZnSe type II QDs

Type II quantum dot structures are of particular interest, due to the spatial separation of electrons and holes within the nanostructures. This in turn, can produce new physical phenomena that may have potential practical applications. In this chapter the growth, characterization and modification of ZnTe/ZnSe type II QDs are presented.

5.1 Background and motivation of ZnTe/ZnSe type II QDs

The idea to use the spin of electrons and nuclei rather than the electron charge for information processing has renewed the interest in spin-related phenomena in solids. Spin-based concepts for semiconductor devices require the preparation of a long-lived spin states [67]. Diluted magnetic semiconductors (DMS) exhibit a giant Zeeman splitting, enabling efficient spin selection and injection. An advantage of the II-VI semiconductors is that the magnetic impurities, such as Mn or Cr, are incorporated isoeletronically. This enables the fabrication of high-quality DMS structures, whose magnetic and electronic properties can be varied independently. II-VI semiconductors such as ZnSe, ZnTe and CdTe, are well suited for spin-coherence studies.

The interest of ZnTe/ZnSe type II QDs for electro spin relaxation applications originates from the type II band structure alignment that induces separation of charge upon photoexcitation and localizes carriers to different regions of the structure [68]. It's good to recall the classification of quantum structures according to the confinement energy schemes of their electrons and holes. Given two semiconductors A and B (with $E_{gB}>E_{gA}$) forming the structure B/A/B, shown schematically in Fig. 5.1(a), the band alignment of the two materials is called type I, in which the electrons and holes are both confined within the same layers A. Compared with type I, Fig. 5.1(b) shows “staggered” confinement scheme, referred as type II. In the case of ZnTe/ZnSe type II QDs, A’ and B’ are ZnTe and ZnSe, respectively. A type II alignment can also be called “spatially indirect bandgap” structure, because the electrons are confined in one layer and the holes are confined in a different layer, which gives rise to a longer lifetime of recombination[69]. The conduction band (CB) offset and valence band (VB) offset are plotted in Fig. 5.1(c) [70]. Moreover, the lifetime can be controlled by optimizing the intensity of the excitation, external electric and magnetic fields. Furthermore, type II heterostructures suppress Auger recombination that shortens the lifetime of the electron-hole separation and becomes a significant obstacle for successful implementation of nanocrystal-based electronic devices [71].

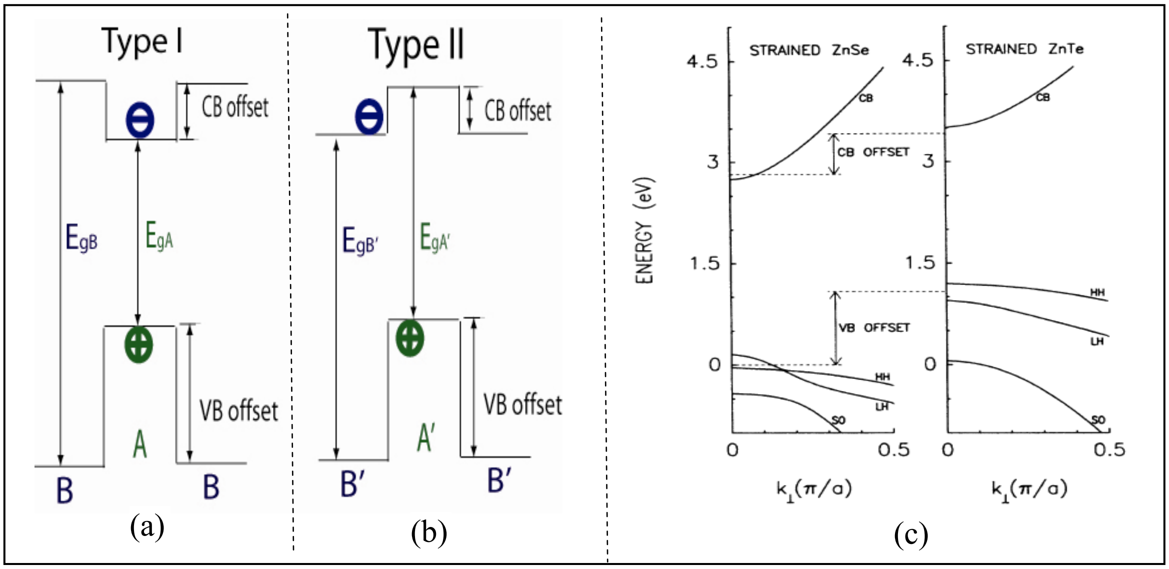

(a) (b) (c)

Fig. 5.1 Type I and Type II band alignments are shown in (a) and (b), respectively. The conduction band (CB) offset and valence band (VB) offset between ZnTe and ZnSe are plotted in (c).

Although II-VI wide band gap semiconductors show great potential for electron spin related devices, there is still a hurdle for successful device fabrication due to the lack of relatively high bipolar conductivity of these materials, and this hurdle resides in obtaining adequate dopants incorporation due to poor solubility and/or excessive compensation [72-74]. It is well known that it is easy to incorporate n-type dopants rather than p-type in certain semiconductors, whereas in others it is inverse [75]. For the semiconductors of specific interest in this work (e.g., ZnSe and related alloys) it is relatively easy to obtain n-type ZnSe, while ZnTe can only be easily doped p-type. This has led to many studies on both bulk and epitaxial materials, and it was expected that in addition to relatively easy n-type doping, good p-type doing could be achieved in ZnSe and related alloys [76-79]. Recently, a high p-type doping level of 6 x 10^{18} cm-3 was achieved in ZnSe by using submonolayer type II ZnTe QDs, while keeping relatively low percentage of Te (2%~3%) [80]. However, this p-type conductivity is still not sufficient for practical device application such as the formation of ohmic contacts. Recent studies suggest that although a high p-type doping was achieved, the free acceptor concentration in these type II nanostructures was low, giving rise to relatively low conductivity material [81].

In our research, in order to reduce the localization of the holes with the purpose of achieving a higher conductivity of the samples, samples have been grown incorporating Mg in the ZnTe QDs. The Mg is expected to modify the bandgap of ZnTe in such a way as to lift the energy level of holes and reduce their confinement making them less localized. The effect of Mg is illustrated in Fig. 5.2. The CB offset between MgTe and ZnSe is 0.45 eV, as small as half of that between ZnTe and ZnSe, shown in Fig. 5.2(c). The incorporation of Mg will decrease the band gap of dot material, while remaining type

II alignment. All samples were characterized by x-ray diffraction (XRD), Hall effect, spectral and time-resolved photoluminescence (PL).

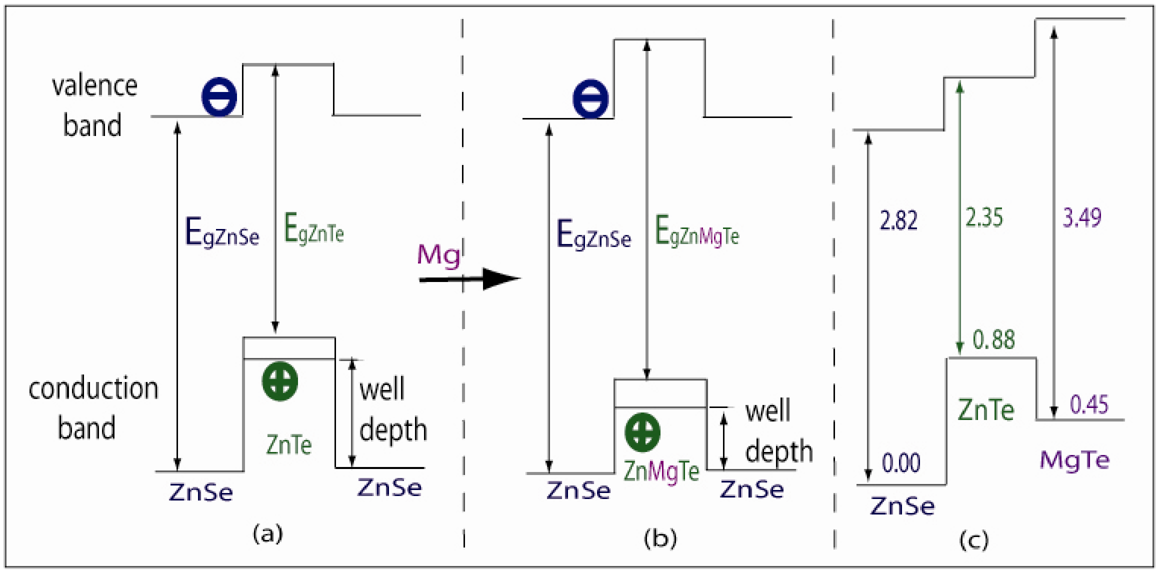

Fig 5.2 The illustration to show how Mg works in order to free holes trapped within the ZnTe/ZnSe type II QDs by modifying band structure. The band gap structures of ZnSe, ZnTe and MgTe are compared in (c).

5.2 Growth of ZnTe/ZnSe type-II QDs

The growth procedure used to grow these type II QDs is a type of migration enhanced epitaxy (MEE). For historical reasons, we often refer to this technique as “(N+Te) δ-doping”. A ZnSe epilayer was first grown for 35 seconds (~5.7 nm). Then we started to grow ZnTe QDs three cycles by MEE, as shown in Fig. 5.3. In cycle 1, the Se shutter was closed and Zn shutter was left open for 5 s to interrupt the growth and produce a Zn-terminated surface. After this, all shutters were closed for 5 s to desorb the excess Zn from the surface, and then the Te(N) shutter was opened to deposit Te(N) on the Zn-terminated surface for 5 s, followed by another growth interruption for 5 s. In cycle 2, the (Mg+Zn) shutters or the Mg shutter itself was first opened for 5 s to incorporate Mg in ZnTe QDs. After this, all shutters were closed for 5 s, and then the Te(N) shutter was opened for 5 s, and another growth interruption was applied for 5 s. The shutter operation in Cycle 3 is same to that in cycle 1, and then the Zn shutter was opened for 5 second, followed by another ZnSe spacer. The main shutter was closed at the end of the growth and the temperature of the substrate was lowered to RT quickly.

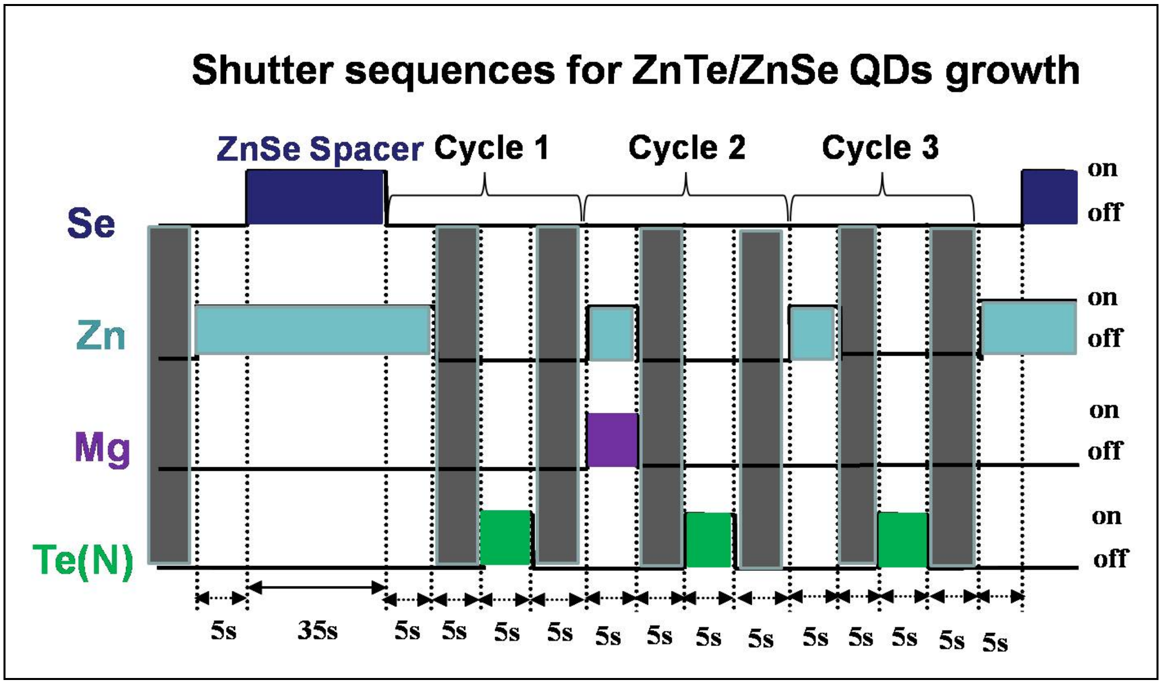

Fig. 5.3 Shutter sequence for growth of type II ZnTe QDs by MEE with incorporation of Mg.

Two sets of samples were grown, as shown in Table 5.1. In set 1, both A2601 and A2602 were grown with Zn and Mg co-deposition during the MEE cycle. However, the temperature of Mg was 20°C higher in A2602 than in A2601. On the other hand, samples in set 2 only were grown with only Mg in the middle of the MEE cycle. The last sample A2656 in set 2 was grown intentionally thicker followed the same recipe to fulfill the Hall effect measurment.

Table 5.1 Two sets of type II ZnTe/ZnSe QDs samples.

Sample		T_{Mg}(°C)	No. of Repeats	ZnSe spacer	Cycle 1		Cycle 2		Cycle 3		
Set 1	A2601	200	100	5.7nm	Zn	(Te+N)	(Zn+Mg)	(Te+N)	Zn	(Te+N)	Zn
	A2602	220	100	5.7nm	Zn	(Te+N)	(Zn+Mg)	(Te+N)	Zn	(Te+N)	Zn
Set 2	A2604	200	100	5.7nm	Zn	(Te+N)	Mg	(Te+N)	Zn	(Te+N)	Zn
	A2605	220	100	5.7nm	Zn	(Te+N)	Mg	(Te+N)	Zn	(Te+N)	Zn
	A2656	210	200	5.7nm	Zn	(Te+N)	Mg	(Te+N)	Zn	(Te+N)	Zn

Double lines represent 5 second interruptions between depositions.

5.3 Characterization of ZnTe/ZnSe type-II QDs

Single crystal X-ray scans, shown in Fig. 5.4, indicate that the lattice constants of the samples with higher Mg source temperature are larger than the ones grown with less Mg, which is consistent with the larger lattice constant of MgTe (6.37Å) compared to that of ZnTe (6.10Å). (Lattice constant of ZnSe=5.6676 Å). As shown in Fig. 5.4, there is a greater effect on the change of the lattice constants when there is only Mg in the middle of the deposition cycle, instead of Mg and Zn, suggesting a higher percentage of Mg in the Zn(Mg)Te/ZnSe type-II quantum dots (QDs) formed that way.

The X-ray spectrum of the thicker sample A2656, shown in Fig. 5.4(c) has the same shape but is somewhat broader, possibly indicating that the layer is not pseudomorphic, and partial relaxation has occurred.

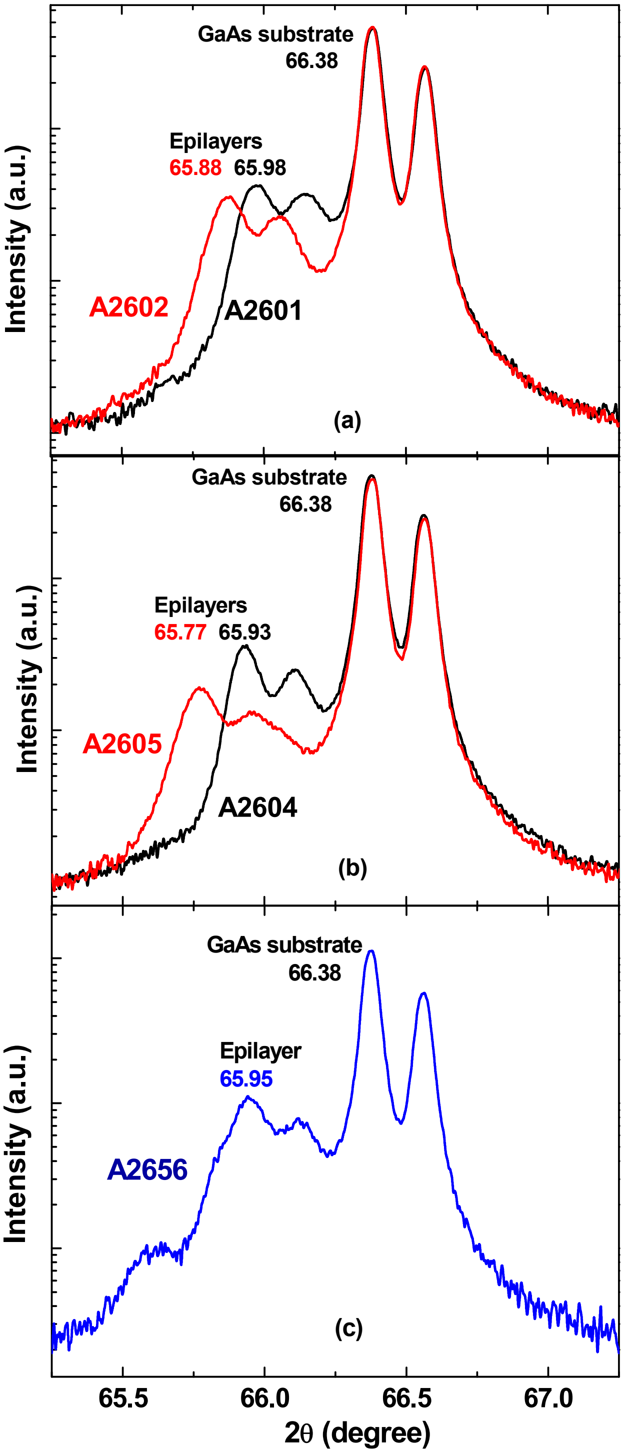

Fig. 5.4 SCXRD of samples A2601 and A2602 in (a), A2604 and A2605 in (b) and A2656 in (c).

Previous studies have shown that the submonolayer type II QD structures have a characteristic behavior when investigated by PL. In particular, two bands appear, known as the “blue band” and the “green band”, which have different behavior as a function of excitation intensity. The PL peak of the blue band exhibits little shift, while the green band shifts significantly (as much as 45 meV over four orders of magnitude of change of excitation intensity in Ref. [69]). Our samples were characterized by temperature and intensity dependent photoluminescence (PL) measurements. The data are summarized in Fig.5.5.

There is a significant blue shift, as large as 200 meV in some samples, when the excitation power increases. This phenomenon, which is usually interpreted as the results of band-banding effect, is characteristic for type II quantum structures. With higher excitation density, stronger band-bending effect in the heterointerfaces is induced by higher population of spatially confined electron-hole pairs. All PL peaks of these samples have the similar excitation dependence. The PL peak is plotted as a function of excitation power in Fig. 5.5(f), which is theoretically predicted to be consistent with a cube root dependence (the pink dashed line in Fig 5.5(f)) [82]. An investigation of the FWHM of the PL peaks shows no obvious broadening, which means the possibility of blue shift due to the band-filling mechanism can be excluded in our case. This further confirms the type-II nature of emission from ZnTe/ZnSe QDs [83].

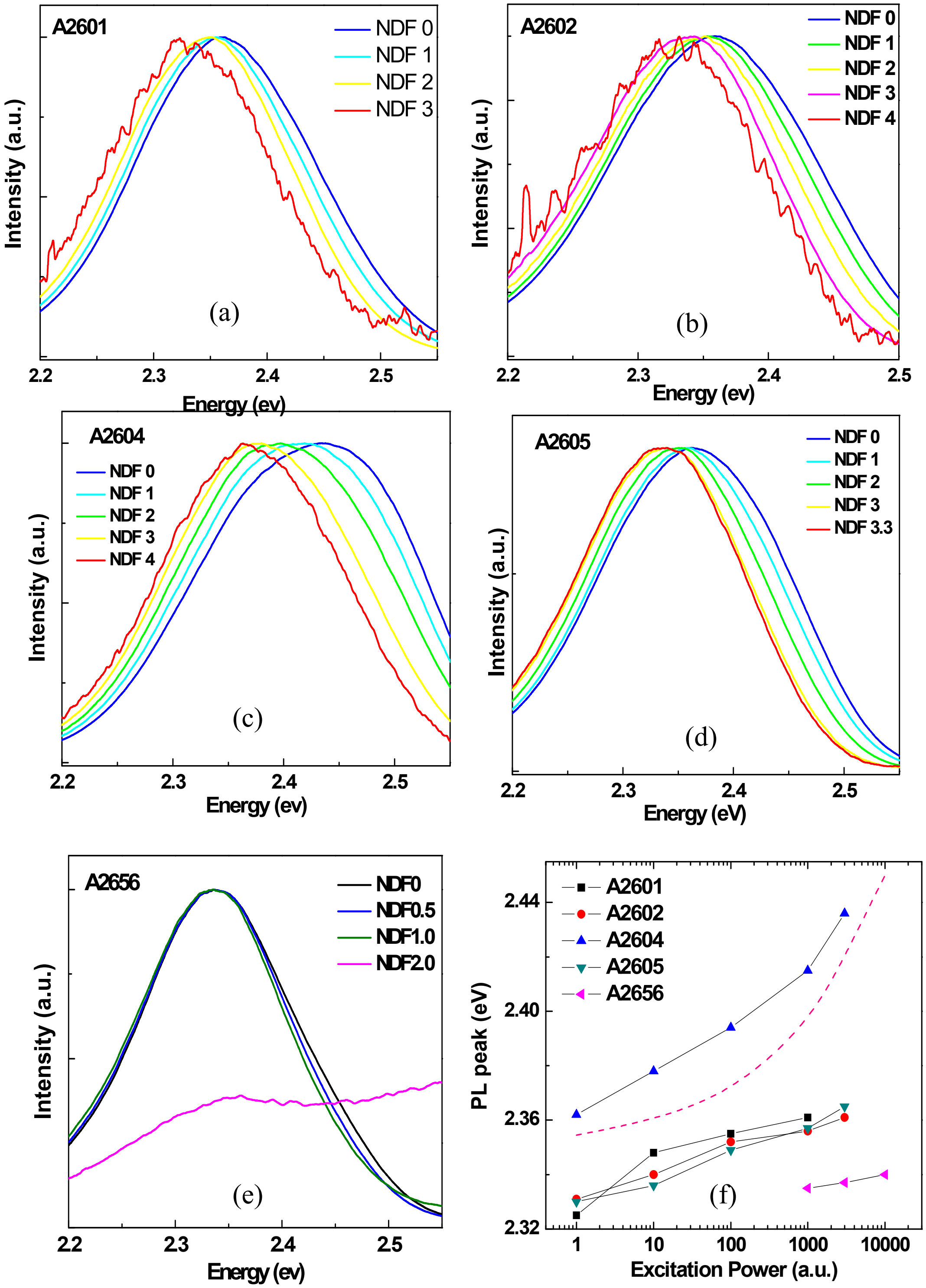

Fig. 5.5 (a-e) PL of samples listed in Table 5.1 measured at 10K. The PL peak is plot as a function of excitation power in (f). The pink dashed line is the result of fitting with $I_{ex}^{1/3}$.

The incorporation of Mg by the MEE technique for the modification of the band structure relies on the fact that the Mg is incorporating only in the Te-based QD regions, and not in the ZnSe-based barrier regions. In order to assess this aspect we performed reflectance measurements. The reflectance spectrum of sample A2656 is shown in Fig. 5.6. Analysis of the data indicated an absorption edge transition at around 2.7ev, which corresponds closely to the band gap of the barrier ZnSe at RT, thus demonstrating that the Mg is not incorporating in the barrier regions.

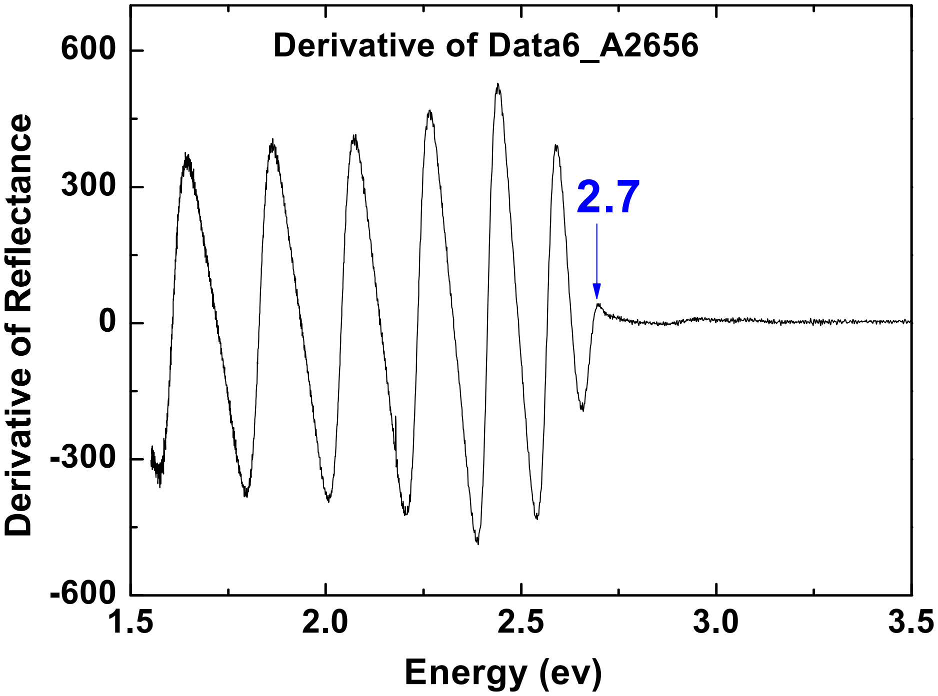

Fig. 5.6 Reflectance spectra of A2656.

Finally, we measured the electrical properties of sample A2656. Au coated contacts were applied to perform Hall effects measurement. The Au contacts are nearly ohmic as indicated by the I-V characteristics, as shown in Fig. 5.7(a). I-V curve measured when only In is used seems to be ‘rectified’, compared with that when Au coated contacts were deposited to boost contacts between In and the II-VI epilayer, which is usually hard to put contacts.

The results of the Hall Effect measurements are summarized in Fig. 5.7(b). The data are taken from the sample having Au-contacts and with a smaller Hall sample size (i.e., smaller distance between the four contacts in the corners of the Hall sample). It seemed that the data were dependent on the current we applied to the sample. The current in the range between 3 and 8 μA showed more stable data. The carrier concentration appears to be p-type, in the range of mid 10^{15} carriers/cc. The mobilities are in the range of 5-25 cm^2/Vs which is consistent with typical hole mobilities in II-VI semiconductors.

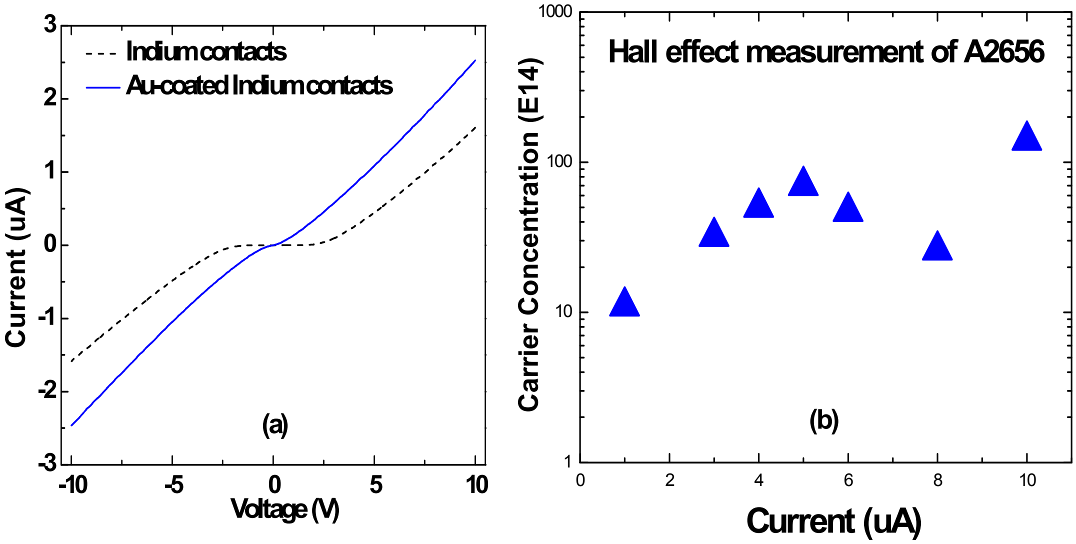

Fig. 5.7 (a) I-V curve of A2656 with (dotted) and without (straight) Au.
(b) The Hall effect data from the sample having Au-contacts.

In conclusions, we have gown Zn(Mg)Te/ZnSe type II QDs, and characterized with XRD, PL, Reflectance and Hall effect. The PL shows blue shifts with higher intensities of exciting laser, an indication of type-II QDs. The Mg containing type II QDs showed improved electrical properties compared to those without Mg, demonstrating our ability to engineer the band structure of these materials. P-type carrier concentration in the range of mid 10^{15} carriers/cc was observed by Hall effect measurement, indicating less confinement of holes. The Zn(Mg)Te/ZnSe type II QDs structures are expected to have potential applications in both electronic devices and spintronics.

Chapter 6

Other related studies: Optically pumped NMR investigation (OPNMR) of CdTe and growth of low dimensional GaAs-based nanostructures for spin relaxation dynamics

In this chapter we show our preliminary results in two areas: first, we explore nuclear spin polarization in CdTe samples through the technique of OPNMR. Strong enhanced signals are observed both in bulk and film CdTe semiconductors, independent of pumping laser helicity, possibly resulting from surface spin dependent recombination. Secondly we explore the growth GaAs/AlAs coupled double QWs and a GaAs/AlGaAs n^+-i-p^+ heterojunction. The characterization results are presented and discussed. Finally, the procedure of GaAs substrate removal is introduced which is essential for future experiments.

6.1 Optically pumped nuclear magnetic resonance (OPNMR)

6.1.1 Experimental observations

Based on the OPNMR equipment described in Chapter 2.3.7, we studied three samples: the first one is a semi-insulating CdTe single crystal from University Wafers (resistivity $>10^9 \Omega$cm, surface orientation [111]). The second one is a 2 μm thick, MBE-grown CdTe epilayer (surface orientation [100]) on a GaAs substrate, with a think ZnSe buffer layer (1nm) between the CdTe film and and the GaAs substrate to improve the film quality [60]. The third on is a semi-insulating GaAs single crystal as a control (350 μm thick, surface orientation [100], resistivity greater than 10^7 Ωcm, American Crystal

Technologies). Samples are used “as received”, although in subsequent experiments we cean the surface of samples using methanol with no apparent change).

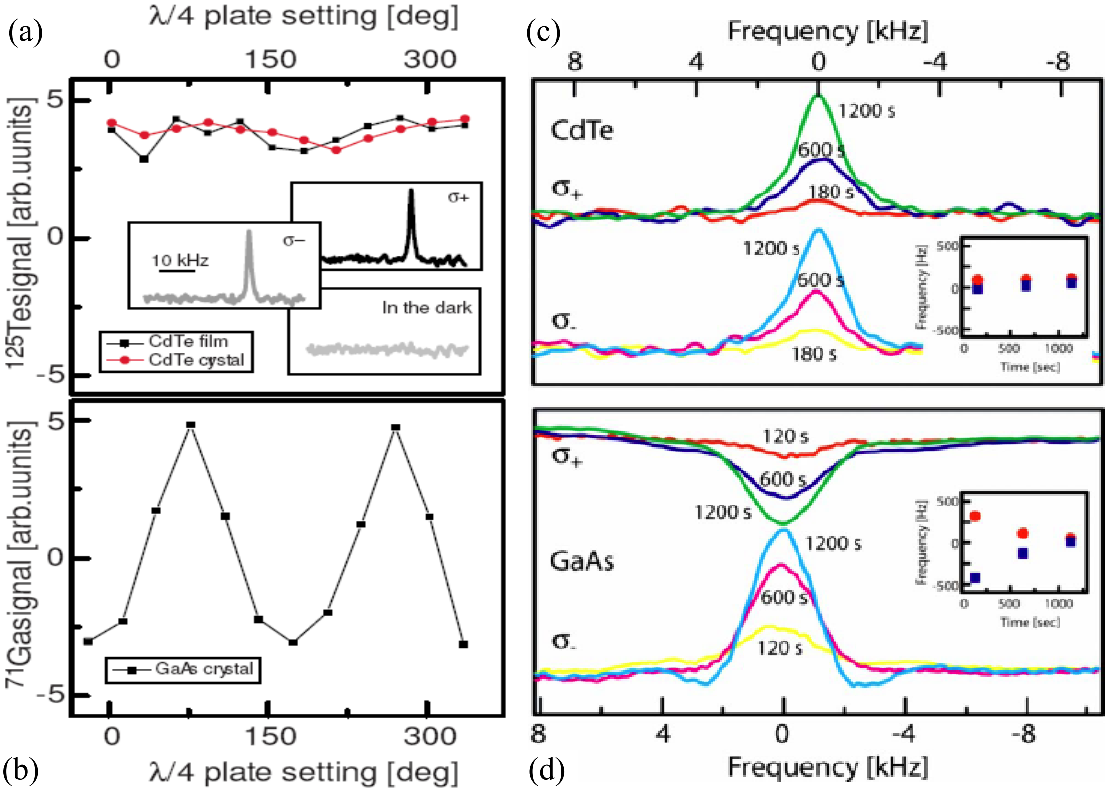

Fig. 6.1 (a) ^{125}Te signal as a function of laser helicity, tuned by λ/4 plate setting. The insets show the actual NMR spectra. (b) The NMR signal of ^{71}Ga. Different helicity-dependence is observed between (a) and (b). (c) and (d) show the NMR spectra for CdTe crystal and GaAs sample, respectively. Helicity-dependent frequency shifts in GaAs at short τ_L are absent in CdTe. Spectra have been shifted for clearity.

Direct detection of nuclear polarization is preceded by the known protocol SAT - τ_L - τ_D -π/2, where SAT is a pre-saturation sequence consisting a series of resonant π/2 pulses. τ_L=300s and τ_D=10s indicate illumination and dark intervals, respectively, and π/2 represents the excitation rf pulse. The frequencies are tuned to 126.022 MHz for ^{125}Te and 121.965 MHz for ^{71}Ga, respectively, according to the 9.4 Tesla magnet. The laser beam diameter is ~1 mm and the power is 300 mW at 1.55 eV.

The NMR signals are plotted as functions of helicity in Fig. 6.1 (a, b). First, we observe no signal in the dark, which is consistent with the long relaxation times found in CdTe. When the laser is on, however, there are strong enhanced signals in both samples, which is independent on the beam polarization. Second, the signals from both bulk and film CdTe samples almost have the equal amplitude, indicating the optical pumping occur within less than 2 μm from the surface. Third, the magnitude and orientation of ^{125}Te nuclear spin alignment is independent of the laser helicity. It is different from the known helicity dependence for ^{71}Ga, which shows signal inversion when tuning circularly polarized illumination from right to left. Furthermore, it is different from the reports for ^{125}Te subject to similar conditions, either, which show a significant change between signals induced by light of different helicity. Fig. 6.1 (c, d) show the NMR signal dependence on the illumination time, additional to laser helicity, for CdTe crystal and GaAs sample, respectively. The resonant peak frequency of ^{125}Te NMR spectra does not vary with either illumination time or laser helicity, on the contrary to the case for ^{71}GaAs, which shows apparent dependence on both illumination time and laser helicity.

Fig. 6.2 shows the dependence of ^{125}Te signal on photon energy, illumination time at different temperatures, power density and temperature. The NMR signal of ^{125}Te reaches a maximum at excitation energy less than the bandgap of CdTe, shown as a dashed line in Fig. 6.2(a). Then it remains virtually unchanged with excitation energy as high as 1.77 eV, different from the sharp decay for ^{71}Ga at higher energy, shown in the inset in Fig. 6.2(a). On the other hand, we observe the ^{125}Te signal dependence behaves similar to that of ^{71}Ga: it increase linearly with illumination time, exponentially with excitation density and decay quickly with temperature, shown in Fig. 6.2 (b-d).

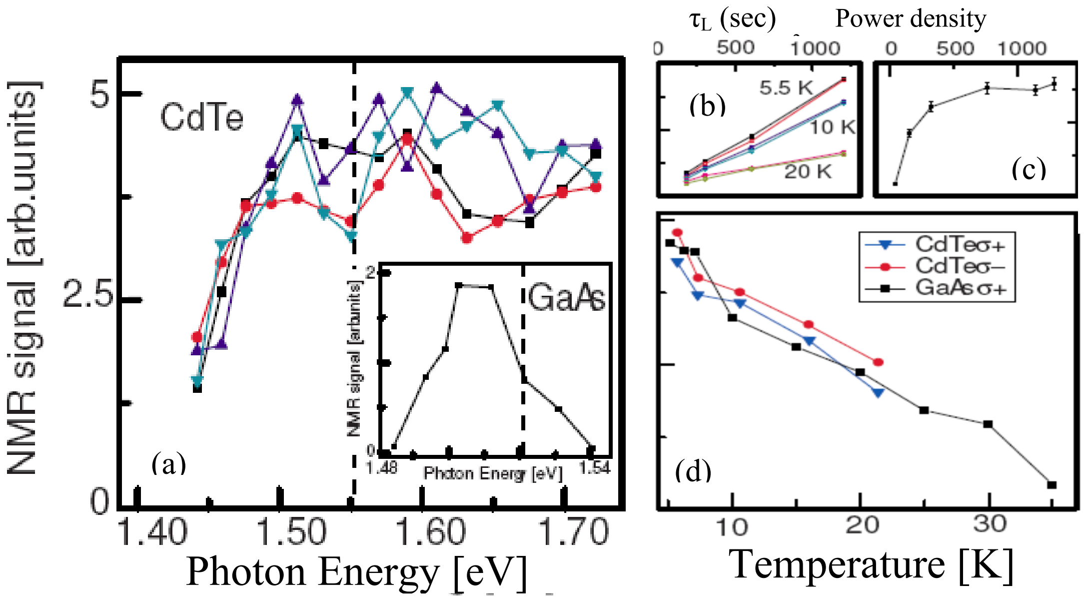

Fig. 6.2 (a) ^{125}Te signal as a function of excitation energy. The inset shows the energy depence of ^{71}Ga. (b), (c) and (d) show ^{125}Te signal as a function of illumination time at different temperatures, power density and temperature. The signal of ^{71}Ga is rescaled for comparison.

6.1.2 Discussion

Although it is hard to theoretically model the helicity-indepence of ^{125}Te, we speculate that the observed behavior originates from strong spin-dependent recombination (SDR), which describes a recombination of excess electrons and holes via paramagnetic impurities and a selective polarization of a conduction electron trapped in a paramagnetic center [84]. When the nuclear spin polarization derives from selective recombination at shallow donors, helicity-independent signals can be expected when free carriers spin-relax before they recombine. In a SDR-dominant OPNMR experiment, when free carriers spin-relax before they recombine, helicity-independent signals can be expeted. Shallow impurities and lattice defects are typically assumed to play a dominant role in the process of optically pumped nuclear spin polarization. Hyperfine couplings, referred in Chapter 2.7, could be locally enhanced through carrier localization by lattice imperfections and thus effectively lead to the alignment of adjacent nuclei. The local polarization subsequently spreads throughout the crystal via a spin "flip-flops" mechanism [85].

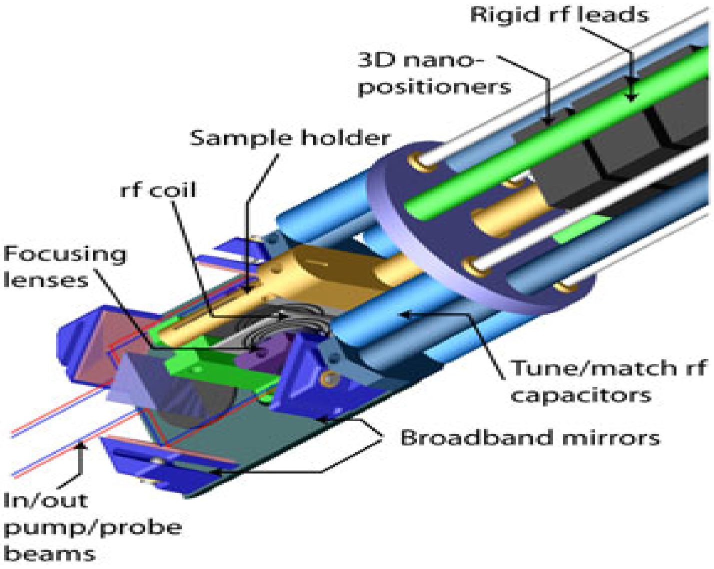

Fig. 6.3 CAD rendition of the proposed probe. The device fits within the cryostat 5-cm-wide bore.

Our next goal is to integrate TRKR with our NMR system. Along with the sensitivity gain afforded by optical detection, the versatility provided by our spectrometer will make it possible to use state-of-the-art NMR sequences for nuclear spin manipulation. Fig. 6.3 shows a CAD-generated image of our already completed design: after following parallel but separate paths, pump and probe pulses are directed onto the bore of the magnet and within the cryostat via an optical window located at its end. A set of adjustable, broadband mirrors mounted on a titanium stage conduct both beams in and out of a system of aspheric, high-numeric-aperture lenses capable of focusing the beam on a diffraction-limited spot. This design is compatible with the ultrafast pulses required by TRFR because no significant distortions are introduced neither in the shape and duration of the light pulse nor in its polarization (as is the case, for example, when long optical fibers are used to channel light onto the sample from external sources). In addition, the configuration of the optical mounts will be fairly flexible, which, in turn, will allow us to alter the geometry of the sample illumination.

6.2 MBE growth and processing of III-V semiconductor nanostructures

6.2.1 GaAs/AlAs QWs

The long spin-coherence times, which are essential to these applications, have been observed in low dimensional semiconductors. Inspired by a paper by Dawson [86], who observed complex long-lived photoluminescence transients involving recombination from electrons and holes in the wide quantum well of a variety of mixed type-I/type-II coupled double QWs, we grew a GaAs/AlAs mutiple QWs structure, shown in Fig. 6.4.

It consists of 20 periods of 25 and 68 Å GaAs double QWs separated by 80 Å AlAs barriers, and is nominally undoped. Electron/hole pairs that are optically excited in the narrow GaAs well become spatially separated, as the electrons can scatter to the wide GaAs well on a picosecond timescale via the AlAs X valley states, whereas the holes at low temperatures can only tunnel through the barrier on a microsecond timescale [87, 88]. The electron density in the wide QW can therefore be varied continuously over a wide range by optical excitation with photon energy greater that the effective gap of the narrow well.

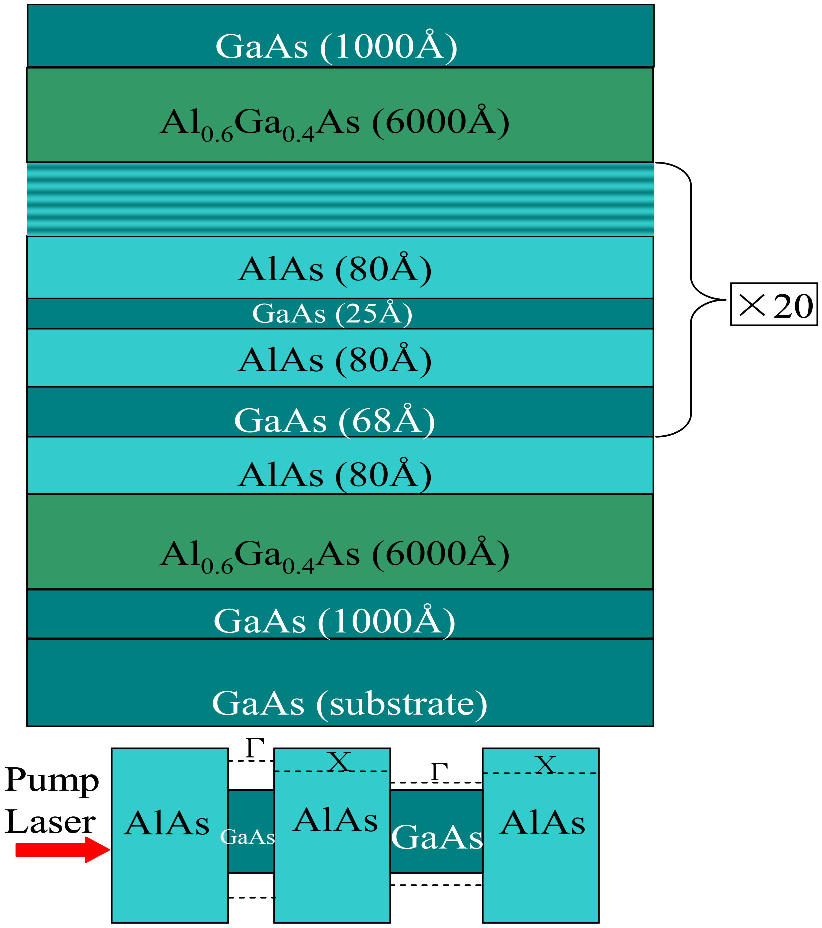

Fig. 6.4 Schematic of GaAs/AlAs QWs structures and its bandgap profile.

In order to establish the growth conditions, in situ RHEED was employed during growth. The RHEED patterns of a calibration samples were streaky throughout. The intensity oscillations of the RHEED specular spot are shown in Fig. 6.5. From these we can confirm the layer by layer growth mechanism and calculate the growth rates. The growth was two dimensional and the growth rates calculated directly from the oscillation peaks were 0.32 ML/s, 0.85 ML/s for GaAs, AlAs, respectively, and 1.15 ML/s for AlGaAs, which is consistent with the sum of the growth rates (1.17ML/s) of GaAs and AlAs measured separately.

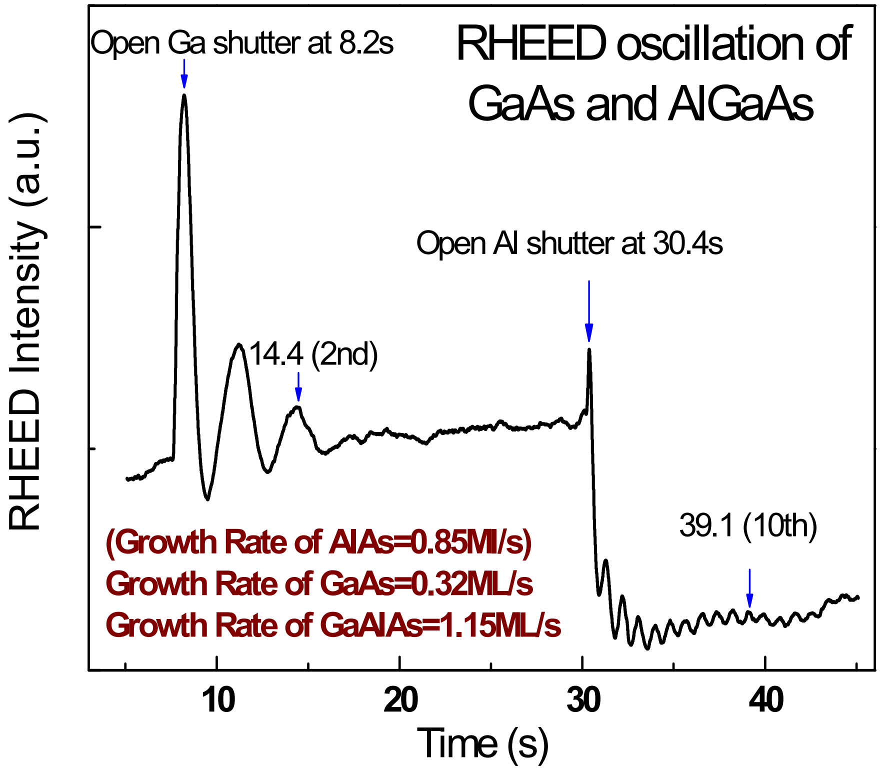

Fig. 6.5 The intensity oscillation of RHEED specular spot.

The AlAs (lattice constant~5.6602 Å) epilayer is almost lattice-matched to the GaAs (lattice constant~5.6533 Å) substrate, and the 0 order of satellite peak is very close to the GaAs substrate peak, shown in Fig. 6.6. The satellite peaks due to the periodicity of the MQW structures could be clearly seen in DCXRD of the 200 direction, shown in Fig. 6.6(b). It shows good quality of the material and is consistent with the designed structures.

The PL was measured at RT and LT and shown in Fig. 6.7. The emission from the narrow well could not be seen at LT, due to the coincidence of the emission and the laser wavelength.

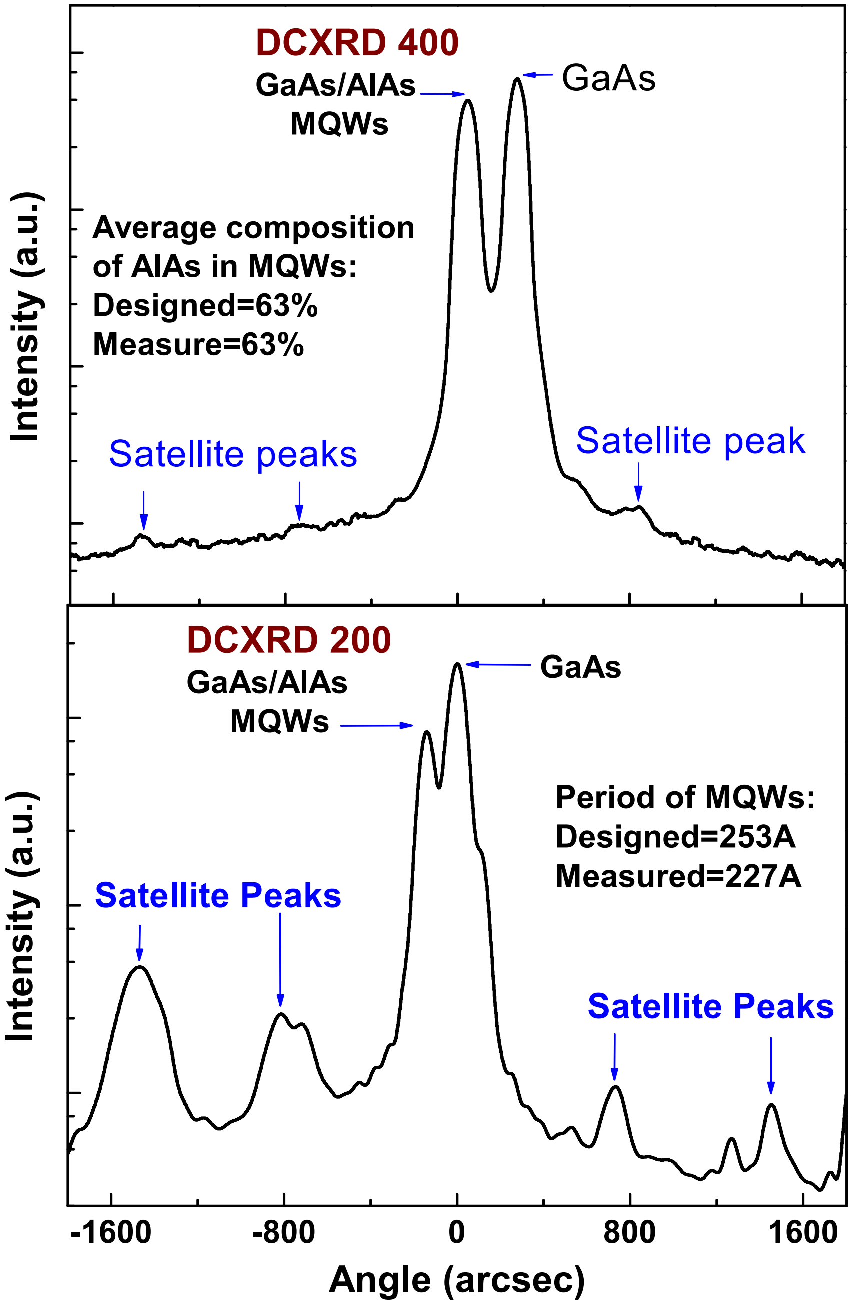

Fig. 6.6 The rocking curve in reflection of (a) 400 and (b) 200 from pseudomorphic GaAs/AlAs layers grown on GaAs.

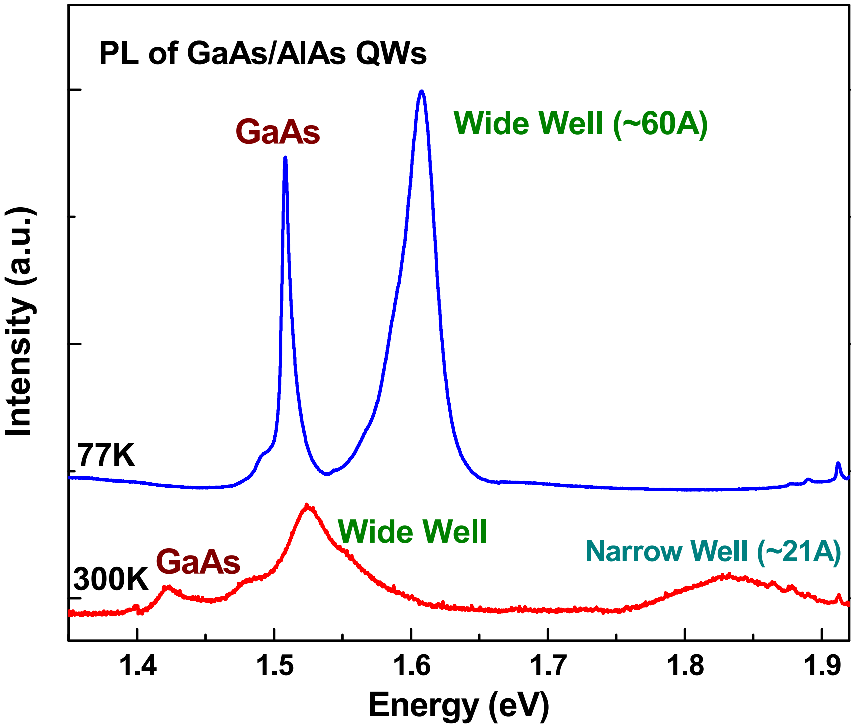

Fig. 6.7 PL of GaAs/AlAs coupled double QWs at 300K (red) and 77K (blue).

6.2.2 GaAs/AlGaAs n^+-i-p^+ heterojunction

Another experiment is inspired by G. Aichmayr [89], who applied longitudinal electric field to separate spatially the electrons and holes, so that spin-dependent exciton-exciton interaction could be tuned in coupled double QWs. We have grown the material structure needed for this other experiment, which is an n^+-i-p^+ GaAs/AlGaAs heterojunction. The schematic diagram of GaAs/AlGaAs QWs is shown in Fig. 6.8. The active region consisted of ten QW periods separated from each other by a 200Å $Al_{0.3}Ga_{0.7}As$ layer, and each formed by two 50Å GaAs wells with a 20 Å $Al_{0.3}Ga_{0.7}As$ barrier in between. An undoped $Al_{0.3}Ga_{0.7}As$ layer on each side of the QW stack (100 and 80nm thick, respectively) completed the intrinsic (i) region of the structure, whose p^+ and

n^+ electrodes are a 500 nm p^+-doped GaAs:Be layer and a 1 μm thick n^+-doped GaAs:Si layer on a (100) GaAs substrate, respectively.

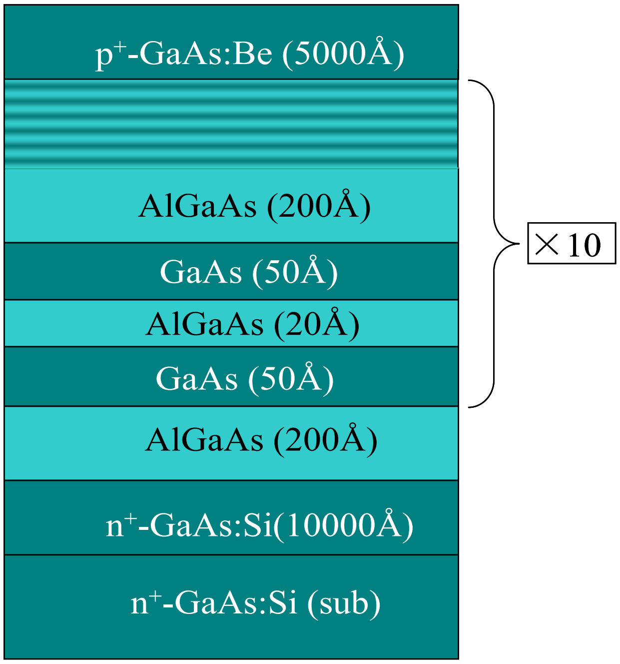

Fig. 6.8 Schematic of GaAs/AlGaAs QWs.

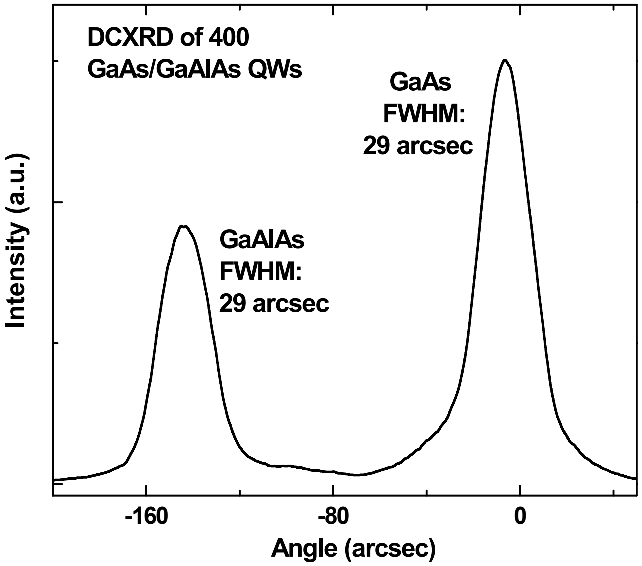

Fig. 6.9 DCXRD rocking curve of the pseudomorphic GaAs/GaAlAs layers.

The DCXRD rocking curve of GaAs/GaAlAs QWs is shown in Fig. 6.9, indicating good material quality of the epilayers and consistent with the designed structure. To get a proper growth temperature of the dopants, calibration growth is performed.

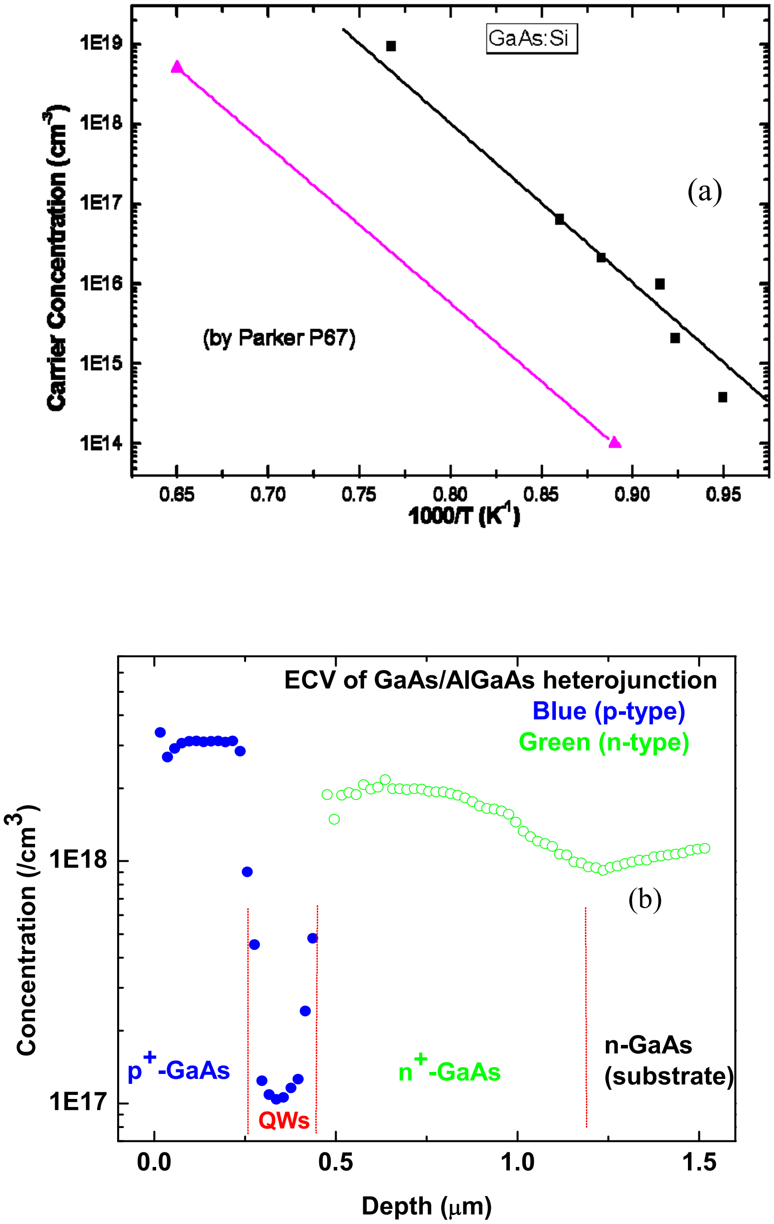

Fig. 6.10 (a) The fitting curve of doping calibration and (b) the curves measured by ECV measurement.

To grow an n^+-i-p^+ structure it was necessary to calibrate the doping. In Fig. 6.10(a), the calibration data obtained from separate calibrations samples doped with Si at different cell temperatures and measured by Hall effect were summarized. The points are fitted to a linear fit shown by the solid line, whose slope is the same as that of previously reported data, shown by the pink line taken from reference [90]. Shown in Fig. 6.10(b) are the curves of the doping profile of the GaAs/AlGaAs heterostructre measured by Electrochemical capacitance voltage (ECV). ECV, combining C-V and depth (etch) profiling, is based on making a liquid electrolyte-semiconductor Schottky contact and measuring the capacitance at a constant dc voltage. It has the capability to characterize the capacitance as a function of depth into the sample structure in steps as small as 0.005 μm, that is, useful for the study of multiple layer structures, such as GaAs/AlGaAs heterostructre. The carrier concentration is ~3 x 10^{18} in p^+ region, as what we expected, but the value in n^+ region is ~2 x 10^{18}, a little lower than what we expected. We also deposited transparent contacts (5.5nm Au) to the structure and performed I-V measurements, which indicates the formation of good ohmic contacts. This structure will allow us to investigate electric-field dependence of spin relaxation times by applying an electrical potential difference on both sides of the sample.

For reliable measurements of the spin polarization studies of thin layers and nanostructures, it is often necessary to remove the relatively thick substrate which may mask the effects being studied. Therefore, there is a need to develop a reliable method of selective etching the GaAs substrate, and prepare windows in GaAs crystals by use of a GaAlAs stop etch layer. Such windows are used for spectroscopic analysis of nanostructures grown on GaAs substrate by MBE, for example, the prior AlAs/GaAs QWs grown on (100) GaAs substrate. Here we demonstrate a technique developed by us.

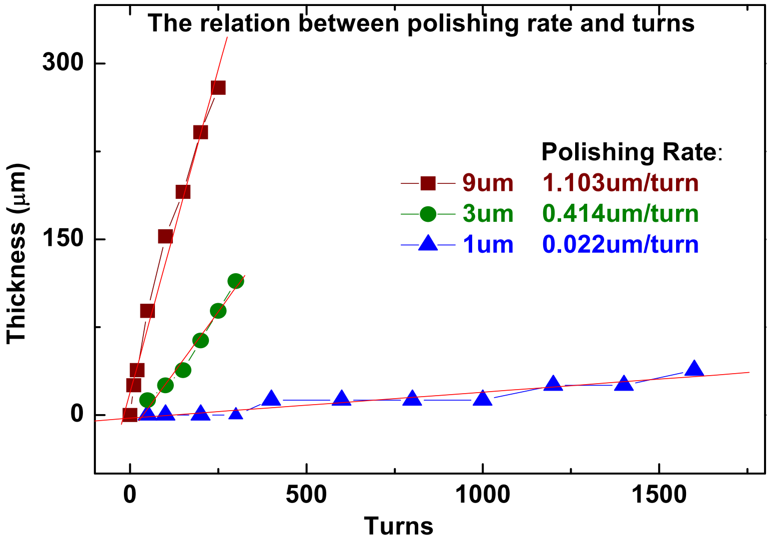

Fig. 6.11 The relation between polishing rate and turns.

The preparation of the sample involved, first, thinning the very thick (~0.6 μm) substrate mechanically to the desired reduced thickness. The polishing rates vary depending on the different diamond size of the lapping film, as is shown is Fig. 6.11. The sample was bonded to a glass plate by crystalbound, a transparent solid at RT and liquid glue at high temperature (>125^{o}C), with the epitaxial layers facing down to the glass plate, which was bonded to the polishing metal block. The sample can be thinned to a thickness of 12.5um, which was monitored by micrometer and measured using a surface profilometer.

The etching rate decreases quickly with the increasing composition of Al in GaAlAs when volume ratio $\gamma=V_{H2O2}/V_{NH4OH}$, a parameter for varying the etch rate, is bigger than certain number (~30). The etching solution used by us is a mixture of hydrogen peroxide (H_2O_2) 50% concentrated and ammonium hydroxide (NH_4OH) 30% concentrated. The composition of the solution given by the volume ratio γ determines the selectivity of GaAs to GaAlAs, which is larger than 100 during the etching process [91, 92].

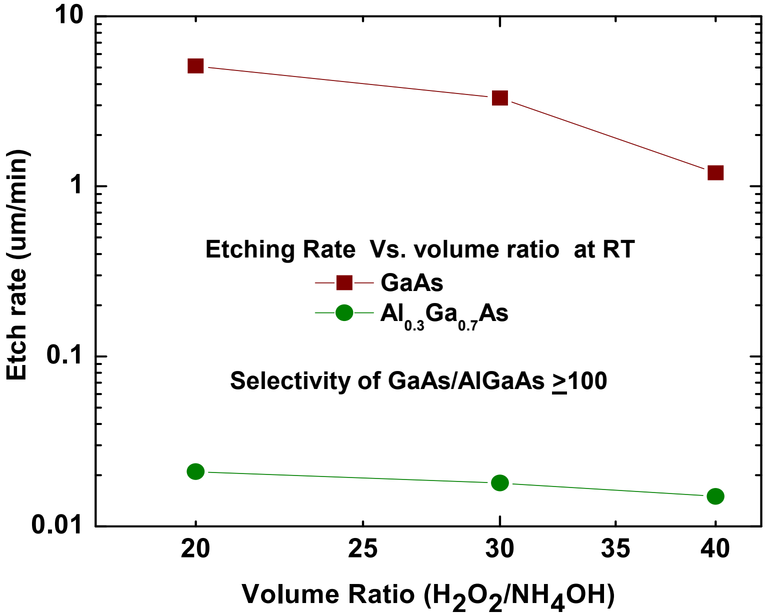

Fig. 6.12 The etching rate as a function of volume ratio (H_2O_2/NH_4OH) measured in our laboratory.

The etching rate vs. volume ratio curve, shown in Fig. 6.12, measured in our laboratory, is consistent with the former reports. A magnetic stirrer was used in the beaker to agitate the solution, while the sample was stirred in the solution with plastic tweezers.

The color of the sample changed to a copper-like color if the whole GaAs substrate was removed. The sample was monitored by eye during the etching process and taken out of the etching solution once the color changed. The cystalbound was removed by acetone and the sample was rinsed by methanol and dried by nitrogen gas.

In conclusion of this chapter, we first studied the enhancement of nuclear spin polarization through optical pumping. We find strong enhancement both in bulk CdTe as well as in CdTe epilayers, independent of the helicity of the laser, which is contrary to the prior reports by others. Compared with GaAs crystal, we ascribe this independence to the surface spin-dependent recombination. Then we grew and characterized GaAs/AlAs and GaAs/GaAlAs multiple coupled double QWs. The measurements show good quality of the material and are consistent with the designed structures. These structures are of interest TRKR and other measurements.

Chapter 7

Summary and proposed future work

In this thesis we have performed studies of MBE growth and characterization of materials and nanostructures whose properties may be of interest for spin enhancement. The following results were achieved:

We grew CdTe epilayers with different crystal orientation by MBE, and investigated the MBE growth of CdTe films on (100) GaAs substrates with (100) ZnSe buffer layers. The high quality ZnSe (100) epitaxy on GaAs allows us to control the II-VI/III-V heterovalent interface prior to the CdTe deposition. By subsequently adjusting the interface between ZnSe and CdTe, it is possible to selectively obtain the growth of either (100) or (111) CdTe epitaxial layers on the (100) ZnSe/GaAs substrate. Reflection high-energy electron diffraction indicates that the nucleation of the CdTe epitaxial layers quickly turns two-dimensional from the onset of growth. X-ray diffraction and photoluminescence measurements indicate that both the (111) and the (100) CdTe films are of high structural quality despite the large lattice constant mismatch of 14.3% between CdTe and ZnSe. By improved CdTe growth techniques, we also grew and characterized low dimensional nanostructures of these materials, such as CdTe/CdMgTe QWs.

Electron spin relaxation time of the (100) and (111) CdTe layers was investigated by TRKR. It is observed that the relaxation time behaves different dependence on temperature between (111) can (100) CdTe epilayers. Based on the data we measured, there is a significant change of spin relaxation time for the (100) CdTe samples, same to the temperature dependent spin relaxation properties of GaAs bulk layers. On the other hand, there are no significant differences of spin relaxation times at different temperatures for the (111) CdTe samples. It also increases with the decreasing FWHM of XRDRC for both (100) CdTe and (111) CdTe. We attribute these phenomena to strain and defect effects.

We also grew ZnTe/ZnSe type II QDs, which are expected to have potential applications in both electronic devices and spintronics. The PL shows blue shifts with higher intensities of exciting laser, an indication of type-II QDs. The Mg containing type II QDs showed improved electrical properties compared to those without Mg, demonstrating our ability to engineer the bandstructure of these materials.

We also studied the enhancement of nuclear spin polarization through optical pumping. We find strong enhancement both in bulk CdTe as well as in CdTe epilayers, independent of the helicity of the laser, which is contrary to the prior reports by others. Compared with GaAs crystal, we ascribe this independence to the surface spin-dependent recombination.

GaAs/AlAs and GaAs/GaAlAs multiple coupled double QWs have also been grown and characterized. The measurements show good quality of the material and are consistent with the designed structures. These structures are of interest TRKR and other measurements.

Several experiments are proposed for future study. They include;

1. Additional growth of (100) and (111) CdTe/CdMgTe QWs and QDs to characterize the quantum confinement effect on the electron spin relaxation dynamics.

2. Additional growth of doped (100) and (111) CdTe films to characterize the effect of carrier concentration on the electron spin relaxation dynamics.

3. Demonstration on the hypothesis that the independence of pumping laser helicity possibly results from surface spin dependent recombination by performing OPNMR on the surface capped CdTe samples.

4. Investigation of type II nanostructures by TRKR to study the electron spin relaxation dynamics.

We also plan further experiments to fully characterize the spin relaxation and related properties of the samples we have grown, and study the effects of temperature, magnetic field, laser photon energy, and polarization on the spin relaxation time.

Publications

1. Qiang Zhang, Yunpu Li, Daniela Pagliero, Aidong Shen, Carlos A. Meriles, and Maria C. Tamargo, "Controlled growth of (100) or (111) CdTe epitaxial layers on (100) GaAs by molecular beam epitaxy and study of their electron spin relaxation times", *J. Vac. Sci. Tech*, 2010, (accepted)
2. Qiang Zhang, Yunpu Li, Xuejun Liu, Daniela Pagliero, Aidong Shen, Carlos A. Meriles, and Maria C. Tamargo, "Dependence of electron spin relaxation times on the crystal orientation of CdTe grown on (100)ZnSe/GaAs substrates", *Physica status solidi*, 2010, (accepted)
3. Qiang Zhang, William Charles, Bingsheng Li, Aidong Shen, Carlos A. Meriles, Maria C. Tamargo, "Control of crystal orientation of CdTe epitaxial layers grown on (001) GaAs with ZnSe buffer layer by molecular beam epitaxy", *J. Crystal Growth* **311** (2009) 2603–2607
4. Wei Dong, Bo Li, Qiang Zhang, Maria C. Tamargo, and Carlos A. Meriles, "Helicity-independent optical pumping of nuclear magnetization in bulk CdTe", *Phys. Rev. B.* **80**, (2009) 045211
5. W. O. Charles, K. J. Franz, A. Shen, Q. Zhang, Y. Gong, B. Li, C. Gmachl, M. C. Tamargo, "Molecular beam epitaxy growth of $Zn_xCd_{(1\_x)}Se/Zn_{x'}Cd_{y'}Mg_{(1-x'-y')}Se$-InP quantum cascade structures", *J. Crystal Growth* **310** (2008) 5380–5384
6. J. D. Wu, J. W. Lin, Y. S. Huang, W. O. Charles, A. Shen, Q. Zhang, M. C. Tamargo, "Characterization of a $Zn_xCd_{1-x}Se/Zn_{x'}Cd_{y'}Mg_{1-x'-y'}Se$ multiple quantum well structure for mid-infrared device applications by contactless electroreflectance and Fourier transform infrared spectroscopy", *J. Phys. D: Appl. Phys.* **42** (2009) 165102

7. W. O. Charles, A. Shen, K. J. Franz, C. Gmachl, Q. Zhang, Y. Gong, C. Gmachl, M. C. Tamargo, “Growth and characterization of $Zn_xCd_{(1\_x)}Se/Zn_{x'}Cd_{y'}Mg_{(1-x'-y')}Se$-InP asymmetric coupled quantum well structures for quantum cascade”, *J. Vac. Sci. Technol. B* **26**, (2008) 1171
8. B. S. Li, A. Shen, W. O. Charles, Q. Zhang, and M. C. Tamargo. “Midinfrared intersubband absorption in wide band gap II-VI $Zn_xCd_{1-x}Se$ multiple quantum wells with metastable zincblende MgSe barriers”, *Appl. Phys. Lett.* **92**, (2008) 261104
9. A. Shen, W. O. Charles, B. S. Li, K. J. Franz, C. Gmachl, Q. Zhang, M. C. Tamargo. “Wide band gap II–VI selenides for short wavelength intersubband devices”, *J. Crystal Growth* **311** (2009) 2109–2112
10. B. S. Li , A. Shen, W. O. Charles, Q. Zhang, M. C. Tamargo, “Growth and properties of wide bandgap MgSe/ $Zn_xCd_{1-x}Se$ multiple quantum wells for intersubband devices operating at short wavelengths”, *J. Crystal Growth* **311** (2009) 2113–2115
11. Qiang Zhang, Xuejun Liu, Yunpu Li, Daniela Pagliero, Aidong Shen, Carlos A. Meriles, and Maria C. Tamargo, “Electron spin relaxation time in CdTe epitaxial layers with (111) and (100) crystal orientation grown on (100) ZnSe on GaAs”, (in preparation)

Presentations in Conferences

1. Qiang Zhang, Yunpu Li, Xuejun Liu, Daniela Pagliero, Le Peng, Aidong Shen, Carlos A. Meriles, and Maria C. Tamargo, "MBE-grown (100) and (111) CdTe epitaxial layers and study of CdTe-related electron spin relaxation times", 2010 CUNY Photonics Retreat, January 14, 2010, New York, NY, USA
2. Qiang Zhang, William Charles, Aidong Shen, Carlos A. Meriles, and Maria C. Tamargo, " (100) and (111)CdTe epitaxial layers grown by molecular beam epitaxy for investigation of electron spin relaxation lifetimes", The 14th International Conference on II-VI compounds, August 23-28, 2009, Saint-Petersburg, Russia.
3. Qiang Zhang, William Charles, Aidong Shen, Carlos A. Meriles, and Maria C. Tamargo, "Control of Orientation of CdTe Epitaxial Layers Grown on GaAs by Molecular Beam Epitaxy and Study of CdTe Electron Spin Relaxation Times", 26th North American Molecular Beam Epitaxy Conference, August 9-12, 2009, Princeton, NJ, USA
4. Qiang Zhang, William Charles, Bingsheng Li, Aidong Shen, Carlos A. Meriles, and Maria C. Tamargo, "Crystal orientation control of CdTe epitaxial layers grown on (100) GaAs with ZnSe buffer layer by molecular beam epitaxy", American Physical Society March Meeting, March 16-20, 2009, Pittsburgh, PA, USA
5. Qiang Zhang, William Charles, Bingsheng Li, Bo Li,Carlos Meriles, Aidong Shen, and Maria C. Tamargo, "MBE-grown semiconductors for the investigation of spin lifetime", CUNY Graduate Center Science Celebration, 2008, New York, NY, USA

Reference List

[1] H. Lu, *Dissertation* (2007).

[2] M. C. Tamargo, A. Cavus, L. Zeng, N. Dai, N. Bambha, A. Gray, F. Semendy, W. Krystek and F. H. Pollak, *J. Elect. Mater*. **25**, 259 (1996).

[3] M. N. Perez-Paz, *Dissertation* (2006).

[4] I. Zutic, J. Fabian, S. Das Sarma, *Rev. Mod. Phys.* **76** (2004) 323.

[5] S. Datta, B. Das, *Appl. Phys. Lett.*, **56**, 665 (1990).

[6] P. Nahalkova, P. Nemec, D. Sprinzl, E. Belas, P. Horodysky, J. Franc, P. Hlidek, P. Maly, *Mater. Sci. Eng. B* **126** 143-147 (2006).

[7] A. V. Kimel, V. V. Pavlov, R. V. Pisarev, V. N. Gridnev, F. Bentivegna, T. Rashing, *Phys. Rev. B* **62** (2000) R10610.

[8] E. Vanelle, M. Paillard, X. Marie, T. Amand, P. Gilliot, D. Brinkmann, R. Levy, J. Cibert, S. Tatarenko, *Phys. Rev. B* **62** (2000) 2696.

[9] P. Peng, D. Milliron, S. Hughes, J. Hohnson, A. Alivisatos, R. Saykally, *Nano. Lett.* **5**, 1809 (2005).

[10] X. R. Wang, Y. S. Zheng, and Sun Yin, *Phys. Rev. B* **72**, 121303(R) (2005).

[11] R. Tycko, J. A. Reimer, *J. Phys. Chem.* **100**, 13240-13250 (1996).

[12] W. Dong, B. Li, Q, Zhang, M. C. Tamargo, C. A. Meriles, *Phys. Rev. B.* **80**, 045211 (2009).

[13] S. Itoh, S. Taniguchi, T. Hino, R. Imoto, K. Nakano, N. Nakayama, M. Ikeda, A. Ishibashi, *Mater Sci Eng* **B43** 55-59 (1997).

[14] D. Li and M. D. Pashley, *J. Vac. Sci. Technol. B* **12**, 2547 (1994).

[15] H. H. Farrel, M. C. Tamargo, J. L. de Miguel, F. S. Turco, D. M. Hwang, R. E. Nahory, *J. Appl. Phys.* **69**, 7021 (1991).

[16] L. Zeng, S. P. Guo, Y. Y. Luo, W. Lin, M. C. Tamargo, H. Xing, G.S. Cargill III, *J. Vac. Sci. Technol. B* **17**(3) (1999) 1255.

[17] A. Y. Cho, *J. Appl. Phys.* **41** 2780 (1970).

[18] E. A. Wood, *J. Appl. Phys.* **35**, 1306 (1964).

[19] C. Hsu, S. Sivananthan, X. Chu, J. P. Faurie, *Appl. Phys. Lett*. **48**, 908 (1986) .

[20] M. C. Tamargo, R. Hull, L. H. Greene, J. R. Hayes, and A. Y. Cho, *Appl. Phys. Lett*. **46**, 569 (1985).

[21] B. S. Li, A. Shen, W. O. Charles, Q. Zhang, and M. C. Tamargo, *Appl. Phys. Lett.* ***92**, 261104(2008).*

[22] L. Zeng, B. X. Yang, and M. C. Tamargo, *Appl. Phys. Lett.* **72** (11), 1317 (1998).

[23] Maria C. Tamargo, Shiping Guo, Oleg Maksimov, Ying-Chih Chen, Frank C. Peiris, Jacek K. Furdyna, *J. Crystal Growth*. **227**, 710 (2001).

[24] S. P. Guo, Y. Luo, W. Lin, O. Maksimov, M. C. Tamargo, I. Kuskovsky, C. Tian, G. F. Neumark, *J. Crystal Growth*. **208**, 205 (2000).

[25] W. Lin, B. X. Yang, S. P. Guo, A. Elmoumni, F. Fernandez, and M. C. Tamargo, *Appl. Phys. Lett*. **75**, 2608 (1999).

[26] H. Lu, A. Shen, W. Charles, I. Yokomizo, M. C. Tamargo, K. J. Franz, C. Gmachl, and M. Munoz, *Appl. Phys. Lett.* **89** 241921 (2006).

[27] Y. Luo, S. P. Guo, O. Maksimov, and M. C. Tamargo, V. Asnin and F. H. Pollak, Y. C. Chen, *Appl. Phys. Lett.* **77**, 4259 (2000).

[28] D. T. F. Marple, *J. Appl. Phys.*, **35**, 539 (1964).

[29] N. P. Barnes, M.S. Piltch, *J. Opt. Soc. Am.* **69** 178 (1979).

[30] O. Madelung (Ed.), *Semiconductors-Basic Data*, 2nd Ed., Springer, 1996.

[31] Daniel T. Pierce, Felix Meier, *Phys. Rev. B* **13** (1976) 5484.

[32] A. Leitenstorfer, A. Lohner, K. Rick, P. Leisching, T. Elsaesser, T. Kuhn, F. Rossi, W. Stolz, K. Ploog, *Phys. Rev. B* **49**, 16372 (1994).

[33] A. K. Paravastu, S. E. Hayes, B. E. Schwickert, L. N. Dinh, M. Balooch, J. A. Reimer, *Phys. Rev. B* **69**, 075203 (2004).

[34] Wei Dong, Dissertation (2009).

[35] I. J. H. Leung, C. A. michal, *Phys. Rev. B* **70**, 035213 (2004).

[36] R. F. C. Farrow, G. R. Jones, G. M. Williams, I. M. Young, *Appl. Phys. Lett.* **39**, 954 (1981).

[37] J. M. Ballingall, M. L. Wroge, and D. J. Leopold, *Appl. Phys. Lett.* **48** (19) 1986.

[38] G. Bratina, L. Sorba, A. Antonini, G. Ceccone, R. Nicolini, G. Biasiol, And A. Franciosi, *Phys. Rev. B* **48** 8899 (1993).

[39] Myoung Seok Kwon, Jeong Yong Lee, Moon Duck Kim, Tae Won Kang, *J. Crystal Growth* **186** 465 (1999).

[40] Kazuto Koike, Takashi Tanaka, Shuwei Li, Mitsuaki Yano, *J. Crystal Growth* **227/228** 671 (2001).

[41] M. D. Kim, M. S. Han, T. W. Kang, T. W. Kim, *Thin Solid Films* **310** 132-137 (1997) .

[42] S. Rubini, B. Bonanni, E. Pelucchi, A. Franciosi, Y. Zhuang, G. Bauer, J. Crystal Growth **201/202** 465 (1999).

[43] M. B. Veron, V. H. Etgens, M. Sauvage-Simkin, S.Tatarenko, B. Daudin, D. Brun-Le Cunff, *J. Crystal Growth* **159** 694 (1996).

[44] E. H. C. Parker, *The Technology and Physics of Molecular Beam Epitaxy*, Plenum Press, New York (1985), P335.

[45] J. M. Ballingall, W. J. Takei, Bernard J. Feldman, *Appl. Phys. Lett.* **47**, 6 (1985).

[46] L. A. Kolodziejski, R. L. Gunshor, A. V. Nurmikko, N. Otsuka in *Molecular Beam Epitaxy* (Noyes Publications, New Jersey, 1995), R. R. C. Farrow, editor, p. 387.

[47] R. I. Dzhioev, K. V. Kavokin,V. L. Korenev, M. V. Lazarev, B. Ya. Meltser, M. N. Stepanova, B. P. Zakharchenya, D. Gammon, and D. S. Katzer, *Phys. Rev. B* **66**, 245204 (2002).

[48] M. Kroutvar, y. Ducommun, D. Heiss, M. Bichler, D. Schuh, G. Abstreiter, J. Finley, *Nature* **432** 81-84 (2004).

[49] T. Ostreich, K. Schonhammer, L. Sham, *Phys. Rev, Lett.* **75**, 2554 (1995).

[50] L. J. Sham, *J. Magn. Magn. Mater.* **200**, 219 (1999).

[51] B. Li, M. Tamargo, C. Meriles, *Appl. Phys. Lett.* **91**, 222114 (2007).

[52] G. Bratina, L. Sorba, A. Antonini, G. Ceccone, R. Nicolini, G. Biasiol, A. Franciosi, J. E. Angelo, W. W. Gerberich, Phys. Rev. B 48, 8899 (1993).

[53] M.S. Han, T. W. Kang, J. H. Leem, B. K. Song, Y. B. Hou, W. H. Baek, M. H. Lee, J. H. Bahng, K. J, Kim, J. M. Kim, H. K. Kim, T. W. Kim, *J. Electron. Mater.* **26**, 507 (1997).

[54] I. Hernandez-Calderon, Optoelectronic Properties of Semiconductors and Superlattices, edited by M. C. Tamargo, Taylor & Francis Inc., 2001, Chapter 4, P113.

[55] D. Awschalom, N. Samarth, *Physics* **2,** 50 (2009).

[56] M. I. D'yakonov, V. A. Maruschak, V. I. Perel', and A. N. Titkov,*Sov.Phys.JETP* **63**,655(1986).

[57] J. Berezovsky, Min Ouyang, Florian Merier, D. Awschalom, D. battaglia, X. Peng, *Phys. Rev. B* **71**, 081309(R) (2005).

[58] J. A. Gupta, D. D. Awschlom, X. Peng, A. P. Alivisatos, *Phys. Rev. B* **59** R10 421 (1999).

[59] K. L. Litvinenko, L. Nikzad, J. Allam, B. N. Murdin, C. R. Pidgeon, J. J. Harris, L. F. Cohen, *J. Supercond Nov Magn* **20**: 4612-465 (2007) .

[60] Q. Zhang, W. Charles, B. Li, A. Shen, C. A. Meriles, M. C. Tamargo, *J. Cryst. Growth* **311** 2603-2607 (2009).

[61] T. Kuroda, T. yabushita, T. Kosuge, A. Techeuchi, K. Taniguchi, T. Chinone, N. Horio, *Appl. Phys. Lett.* **85** 3116 (2004) .

[62] C. Brimont, M. Gallart, A. Gadalla, O. Cregut, B. Honerlage, P. Gilliot, *J. Appl. Phys.* **105**, 023502 (2009) .

[63] D. Jena, Phys. Rev. B **70** 245203 (2004).

[64] M. Berding, *Appl. Phys. Lett.* **74** 552 (1999).

[65] A. Kanno, Y. Masumoto, *Phys. Rev. B* **73**, 073309 (2006).

[66] D. Sprinzl, J. Kune, T. Ostatnicky, P. Horodysky, R. Grill, J. Franc, P. Maly, P. Nemec, *Phys. Stat. Sol. (b)* **244**. No. 5, 1612-1617 (2007).

[67] Y. Ohno, D. K. Young, B. Beschoten, F. Matsukura, H. Ohno, D. D. Awschalom, *Nature* **402**, 790 (1999).

[68] P. Peng, D. Milliron, S. Hughes, J. Hohnson, A. Alivisatos, R. Saykally, *Nano. Lett.* **5**, 1809 (2005).

[69] Y. Gu, I. L. Kuskovsky, M. Voort, G. F. Neumark, X. Zhou, M. C, Tamargo, *Phys. Rev. B* **71**, 045340 (2005).

[70] Y. Rajakarunanayake, R. H. Miles, G. Y. Wu, T. C. McGill, *Phys. Rev. B* **37** 10212 (1988).

[71] V. I. Klimov, D. W. McBranch, C. A. Leatherdale, M. G. Bawendi, *Phys. Rev. B* **60** 13740 (1999).

[72] G. f. Neumark, R. M. Park, and J. M. Depuydt, *Phys. Today* **47** (6), 26 (1994).

[73] G. F. Neumark, *Mater. Lett.* **30**, 131 (1997).

[74] G. F. Neumark, *Mater. Sci. Eng., R.* **21**, 1 (1997).

[75] D. J. Chadi, *Phys. Rev. B* **59**, 15181 (1999).

[76] A. Kamata, H. Yoshida, S. Chichibu, and H. Nakanishi, *J. Cryst. Growth* **170**, 518.

[77] C. S. Yang, W. C. Chou, D. M. Chen, C. S. Ro, J. L. Shen, and T. R. Yang, *Phys. Rev. B* **59**, 8128 (1999).

[78] H. D. Jung, C. D. Song, S. Q. Wang, K.Arai, Y. H. Wu, Z. Zhu, T. Yao, and H. Katayama-Yoshida, *Appl. Phys. Lett.* **70**, 1143 (1997).

[79] Igor L. Kuskovsky, Y. Gu, Y. Gong, H. F. yan, J. Lau, I. C. Noyan, G. F. Neumark, O. Maksimov, X. Zhou, M. C. Tamargo, V. Volkov, Y. Zhu, and L. Wang, *Phys. Rev. B* **73**, 195306 (2006).

[80] W. Lin, S. P. Guo, M. C. Tamargo, I. Kuskovsky, C. Tian, and G. F. Neumark, *Appl. Phys. Lett.* **76**, 2205.

[81] Y. Gong, W. MacDonal, G. F. Neumark, M. C. Tamargo, I. L. Kuskovsky, *Phys. Rev. B* **77**, 155314 (2008).

[82] N. N. Ledentsov, J. Bohrer, M. Beer, F. Heinrichsdorff, M. Grundmann, D. Bimberg, S. V. Ivanov, B. Ya. Meltser, S. V. Shaposhnikov, I. N. Yassievich, N. N. Faleev, P. S. Kop'ev, Zh. I. Alferov, *Phys. Rev. B* **52** 14058 (1995).

[83] M. C. Kuo, J. S. Hsu, J. L. Shen, K. C. Chiu, W. C. Fan, Y. C. Lin, C. H. Chia, W. C. Chou, M. Yasar, R. Mallory, A. Petrou, H. Luo, *Appl. Phys. Lett.* **89**, 263111 (2006).

[84] D. J. Lepine, *Phys. Rev. B* **6**, 436 (1972).

[85] P. L. Kuhns, A. Kleinhammes, T. Schmiedel, W. G. Moulton, E. Hughes, S. Sloan, P. Chabrier, C. R. Bowers, *Phys. Rev. B* **55**, 7824 (1997).

[86] P. Dawson, M. J. Godfrey, *Phys. Rev. B.* **68**, 115326 (2003).

[87] H. Hoffmann,1 G. V. Astakhov,1,2 T. Kiessling,1 W. Ossau,1 G. Karczewski,3 T. Wojtowicz,3 J. Kossut,3 and L. W. Molenkamp, *Phys. Rev. B.* **74**, 073407 (2006).

[88] Z. Chen, S. Carter, R. Bratschitsch, P. Dawson and S. Cundiff, *Nature Phys.*, **11** Feb. (2007).

[89] G. Aichmayr, M. Jetter, L. Vina, J. Dickerson, F. Camino, and E. E. Mendez, *Phys. Rev. Lett.* **83**, 2433 (1999).

[90] E. H. C. Parker, *The Technology and Physics of Molecular Beam Epitaxy*, Plenum Press, New York (1985).

[91] Y. Uenishi, H. Tanaka, H. Kita, *IEEE Transactions on Electron Devices,* Vol **41**, No. 10, P1778, Oct 1994.

[92] J. J. Lepore, *J. Appl. Phys.* **51** (12), 1980.